DISSERTATION

submitted to the

Combined Faculty of Natural Sciences and Mathematics

of Heidelberg University, Germany

for the degree of

Doctor of Natural Sciences

Put forward by

M.Sc. Judith Thoma

Born in Würzburg, Germany

Oral examination: 08.11.2022

Electrostatics, Mechanics, and Dynamics of Biological Interfaces at and out of Equilibrium

Referees: Prof. Dr. Motomu Tanaka
Priv.-Doz. Dr. Falko Ziebert

Elektrostatik, Mechanik und Dynamik von biologischen Grenzflächen in und außerhalb von Gleichgewichtszuständen

Biologische Grenzflächen sind nicht nur Grenzen, die zwei Phasen voneinander trennen, sondern besitzen auch Strukturen und Funktionen. Das Hauptziel dieser Arbeit ist die quantitative Bestimmung der Elektrostatik, Mechanik und Dynamik biologischer Grenzflächen in Abwesenheit und Anwesenheit externer Störeinflüsse durch die Kombination verschiedener physikalischer Techniken.

In Kapitel 4 wird auf molekularer Ebene untersucht, wie die Kombination von geladenen Tensiden und Alkohol die elektrostatische Barriere an der Oberfläche von Bakterien zerstört. Strukturelle Veränderungen senkrecht zur Bakterienmembran wurden mit Röntgenreflektometrie in sub-Å-Auflösung untersucht. Zur Bestimmung der Konzentrationsprofile einzelner Ionen nahe der Oberfläche in Å-Auflösung wurde Röntgenfluoreszenz gemessen. Die ermittelten Daten zeigten, dass die Permeation von kationischen Tensiden in die Membran durch eine kondensierte Schicht von Ca-Ionen blockiert wurde, die die geladenen Saccharidgruppen vernetzten. Bemerkenswerterweise führt die Zugabe von aromatischem Alkohol zu einer signifikanten Störung der strukturellen Integrität der Membran. Die Ergebnisse dieser Kombination von Röntgenreflexion und Röntgenfluoreszenz zeigen, wie geladene Tenside und Alkohol, die Hauptbestandteile von Desinfektionsmitteln, synergistisch die äußere Oberfläche von Bakterien beeinflussen.

Der Schwerpunkt von Kapitel 5 ist die quantitative Untersuchung der mechanischen Eigenschaften und der Nichtgleichgewichtsdynamik lebender Zellen auf Substraten, die die zelluläre Mikroumgebung präzise modellieren. Die Adhäsionsfunktion und die räumlich-zeitliche Dynamik humaner hämatopoetischer Stammzellen wurden in Zusammenarbeit mit Prof. A. D. Ho und Prof. C. Müller-Tidow (Innere Medizin V, Universitätsklinikum Heidelberg) auf die Auswirkungen klinischer Wirkstoffe für Leukämietherapie untersucht. Die Adhäsionsfläche und -stärke der Zellen wurden mit Marker-freier Mikrointerferometrie und einem Assay zur Zellablösung gemessen, der auf Laser-induzierten Schockwellen basiert. Die Zelldynamik wurde anhand von Bildgebungsdaten durch eine Leistungsspektralanalyse der Membranverformung charakterisiert, die den Energieaufwand durch aktive Verformung bestimmen ließ. Schließlich wurde die räumlich-zeitliche Dynamik der Zellen theoretisch modelliert, indem periodische Verformungskräfte und Reibungskoeffizienten zum Ohta-Okuma-Modell für selbstbewegende, verformbare Partikel hinzugefügt wurden. Obwohl dieses Modell nicht in der Lage ist, chemische Reaktionen innerhalb der Zellen zu berücksichtigen, konnten die Simulationen die Verformung und Bewegung menschlicher Stammzellen in Abwesenheit und Anwesenheit von Medikamenten als Modulation von Adhäsion und aktiver Verformung beschreiben.

Electrostatics, Mechanics, and Dynamics of Biological Interfaces at and out of Equilibrium

Biological interfaces are not just boundaries separating two bulk phases, but also possess structures and functions. The primary aim of this thesis is the quantitative determination of electrostatics, mechanics, and dynamics of biological interfaces in the absence and presence of external perturbation by the combination of various physical techniques.

In chapter 4, I investigated the mechanism how the combination of charged surfactants and alcohol synergistically destroys the electrostatic barrier protecting the surface of bacteria on molecular level. To quantitatively model the surface of bacteria, a monolayer of complex glycolipids was prepared at the air-water interface. Structural changes in the direction perpendicular to the membrane were investigated with specular X-ray reflectivity in sub-Å resolution. To determine the concentration profiles of individual ions in the vicinity of the surface in Å resolution, X-ray fluorescence was measured under grazing incidence near the angle of total reflection. The obtained data indicated that the permeation of cationic surfactants into the membrane was blocked by a condensed layer of Ca^{2+} ions cross-linking the charged saccharide groups. Remarkably, the addition of aromatic alcohol causes a significant increase of roughness between hydrocarbon chains and saccharide headgroups, leading to a disturbance of structural integrity of the membrane. These results demonstrate that the combination of X-ray reflectivity and grazing incidence X-ray fluorescence unravelled, how charged surfactants and alcohol, the main ingredients of sanitisers, synergistically act on the outer surface of bacteria.

Chapter 5 focuses on the quantitative investigation of the mechanical properties and non-equilibrium dynamics of living cells on substrates precisely mimicking cellular microenvironments. As biological system, I chose human haematopoietic stem cells in collaboration with Prof. A. D. Ho and Prof. C. Müller-Tidow (Internal Medicine V, University Hospital Heidelberg), and investigated the impact of clinical agents for leukaemia therapy on adhesion function and spatio-temporal dynamics. Area of tight cell contact and adhesion strength were measured by label-free micro-interferometry and a cell-detachment assay, which is based on shockwaves induced by pico-second laser pulses. Dynamics of cells were characterised by power spectral analysis of membrane deformation from live cell imaging data, yielding the energy dissipation due to active deformation. Finally, the spatio-temporal dynamics of cells were theoretically modelled by adding periodic deformation forces and friction to the Ohta-Okuma model for self-propelled, deformable particles. Although this model is not able to include chemical reactions inside the cells, the simulations could describe the deformation and motion of human stem cells in the absence and presence of drugs as modulation of adhesion and active deformation.

You must never think of the whole street at once,
understand?
You must only concentrate on the next step,
the next breath, the next stroke of the broom,
and the next, and the next. Nothing else.

That way you enjoy your work,
which is important,
because then you make a good job of it.

MICHAEL ENDE,
Momo

Acknowledgements

I would like to thank

Prof. Dr. Motomu Tanaka for offering this project, for which I had the great opportunity to join the experiments at the ESRF in Grenoble, France, and extend my working horizon to the group of Prof. Dr. Sano at the University of Tokyo, Japan,

Priv.-Doz. Dr. Falko Ziebert for kindly acting as second referee to this work and my final examination,

Prof. Dr. Anthony D. Ho and **Prof. Dr. Carsten Müller-Tidow** from Internal Medicine V, University Hospital Heidelberg, for giving me the opportunity to contribute to this interdisciplinary project related to human haematopoietic stem cells,

Prof. Dr. Masaki Sano and **Dr. Tetsuya Hiraiwa** for hosting me at the University of Tokyo and for the introduction to the numerical simulations,

Dr. Caroline Pabst, Dr. Alicia He, and Angela Lenze from Internal Medicine V, University Hospital Heidelberg, for kindly providing technical assistance for the isolation and preparation of hHSC samples,

Dr. Alexandra Becker for the introduction to the experimental work,

Dr. Wasim Abuillan for all the guidance and encouragement throughout this work, the counselling regarding experiments and analysis in and out of equilibrium, the extended proofreading of this thesis, and most of all for all the solid support,

and **Natalie Munding, Esther Kimmle, and Julian Czajor** for further proofreading my thesis.

My special thanks go to

Wasim and Stefan for countless and most educational conversations including a mouse of most unusual colour, a bear of questionable credibility, and a sheep with most particular ideas, which allowed us to start every week with Lach- und Sachgeschichten,

Sven, Danny, Julian, Susanna, Philipp, and Natalie for all the times we found a path to save the world from villainous goblins, ogres, and ancient ones,

Bahareh, Zahra, Felix, and Esther for making the office an enjoyable environment,

Benni for entrusting me to provide the safest of all places for his most precious piece of aluminium foil,

Christina, Henrik, and Arno for keeping the balance between the forces of work and music, and for being the most hornificent friends of all times,

Henrik, Arno, Christian, Metty, Tobi, Lilo, Arne, and many others in varying cast of characters for α-projects regarding the mystic terraforming of Gaia, from the galaxy's wingspan of Tokyo through the stone ages of eclipse in Andor to the twilight of photosynthesis, even if it turned out to be only a δ- or ε-crew,

and of course my family for all the support one could wish for.

Contents

1. Introduction

During the past several decades, mounting evidence has postulated that an interface is not merely a boundary between two bulk phases, but contains structures and functions at and out of equilibrium. One of the most prominent examples in nature are biological interfaces, such as membranes.

Biological membranes are a crucial element in the evolution of life, as they define interfaces in living systems by the formation of compartments for biochemical reactions, as well as by the selective exchange of materials and signals between compartments. One of the most important building blocks of eukaryotic cell membranes are phospholipids, which self-assemble into vesicles, or planar bilayer sheets in aqueous solution.[1] To minimize the entropy of the solvent, the non-polar and therefore hydrophobic hydrocarbon chains assemble together to minimise the contact to the polar solvent (water), while the hydrophilic head groups are exposed to the polar, aqueous environment. Figure 1.1 (A) displays the schematic composition of a eukaryotic cell membrane. The extracellular leaflet of the bilayer is typically covered with oligosaccharides anchored to glycolipids or glycoproteins, while the inner leaflet is coupled to the cytoskeleton. Further membrane-associated proteins can be categorised into two classes: integral, transmembrane proteins spanning across the lipid bilayer, and peripheral membrane proteins docking to the membrane surface.[2]

1.1. Destabilisation of Biological Interfaces: Synergistic Function of Alcohol and Surfactants against Bacterial Membranes

Structural integrity of membranes is protected against external cues, such as harsh extracellular environment and external stress, by charged saccharide-based poly-

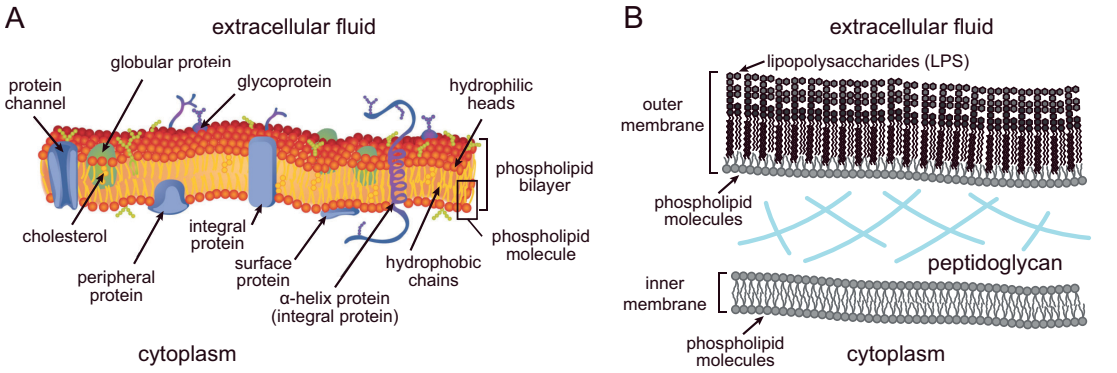

Figure 1.1.: Schematic illustration of eukaryotic cell membrane and cell envelope of Gram-negative bacteria. (A) Eukaryotic cell membrane composed of amphipathic lipids with embedded proteins and attached oligosaccharides.[3] **(B)** Bacterial outer membrane consisting of a bilayer of phospholipids and lipopolysaccharides (LPS), the peptidoglycan cell wall, and the cytoplasmic cell membrane consisting of a phospholipid bilayer. Adapted from Duong *et al.*[4]

mers attached to the membrane surface. In Gram-negative bacteria, for example, a dense layer of lipopolysaccharides (LPS) is displayed on the surface of the outer membrane, as illustrated in figure 1.1 (B),[4] which in the presence of divalent cations such as Ca^{2+} or Mg^{2+} protects the membrane from structural perturbations due to changes in the surrounding environment. It has been shown that the association of divalent Ca^{2+} ions to the negatively charged cores of the LPS headgroups prevent cationic antimicrobial peptides from disturbing the stratified membrane structures.[5–8] The formation of an electrostatic barrier of Ca^{2+} cross-linking LPS molecules and protecting the membrane structure from intrusion was further proven by coarse-grained Monte Carlo simulations.[5,9] Furthermore, LPS-Ca^{2+}-layer were investigated by interfacial shear rheology, which showed them to behave like a two-dimensional gel at the air-water interface.[10]

During the past several decades, many antibiotics have been developed to overcome this barrier function, which in turn created the new problem of multi-drug resistant bacteria. More recently, studies showed the achievement of a sufficient hygiene level by the proper use of sanitisers, without increasing the amount of antibiotic treatments.[11] Cationic surfactants, also known as quaternary ammonium compounds (QACs), are the most commonly used disinfectants,[11,12] which electrostatically bind to the negatively charged saccharide groups of LPS by their positively charged nitrogen, as suggested by several studies. Upon integration of

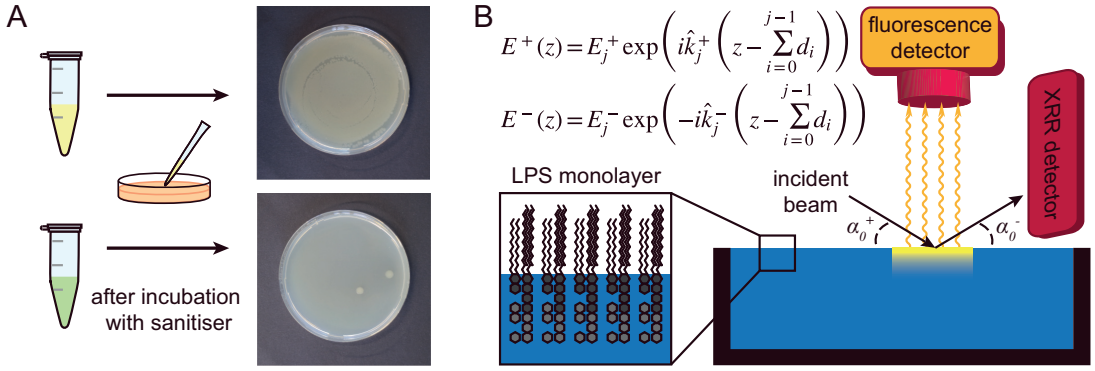

Figure 1.2.: Investigation of destabilisation of biological interfaces. (A) Bacterial killing assay confirming the bactericidal capability of sanitisers and their ingredients.[16] **(B)** Experimental setup of simultaneous specular X-ray reflectivity (XRR) and grazing incidence X-ray fluorescence (GIXF) at the air-water interface using lipopolysaccharides LPS Ra.

hydrocarbon chains into the hydrophobic core of the outer bacterial membrane the cytoplasm is subsequently lost, followed by bacterial death.[11,13,14] Although several bacterial strains have gained resistance against high doses of QACs,[13,15] Gram-negative bacteria are still vulnerable against the antimicrobial function of QACs, if it is facilitated by the combination with aromatic alcohol (cf. figure 1.2 (A)).[14–16]

The synergistic function of these two components is well known and utilised in commercial products,[14] but the physical mechanism behind the bactericidal effect, however, has yet to be unravelled. The systematic screening of various combinations of alcohol and surfactant, for example, suggested the alcohol to cause an increase in membrane fluidity, promoting the permeation by the surfactants.[17] However, the quantitative impact of how the combination of simple molecules destabilises biological interfaces remains largely unknown.

From the experimental point of view, quantitative characterisation of soft biological interfaces including charged macromolecules is non-trivial and poses challenges such as the determination of electrostatic interactions of biological interfaces. On the sub-molecular level, at length scales below 1 nm, charge density is neither uniform nor static. Due to further cross-linking of multivalent ions with charged moieties, such as charged saccharide groups in lipopolysaccharides, the classical Deraguin-Landau-Verwey-Oberbeck (DLVO) theory can not be applied. The critical roles of ion-specific interactions in ligand-receptor interaction and protein fold-

ing have been indicated by ample experimental evidence,[18,19] but the quantitative determination of density profiles of specific ions, such as K^+ and Ca^{2+}, still remains an experimental challenge. However, density profiles of specific ions in the close proximity of interfaces, typically within 20 nm, can not be determined by commonly used spectroscopic techniques, such as sum frequency generation (SFG) spectroscopy. Structural details in the direction perpendicular to the interface are commonly investigated using specular X-ray or neutron reflectivity. However, due to the lack of significant difference in scattering length densities, these techniques are not able to localise specific elements in Å resolution.

In Chapter 4, the synergistic function of cationic surfactant and aromatic alcohol, the major components of commercial sanitisers, is investigated by simultaneous specular X-ray reflectivity (XRR) and grazing incidence X-ray fluorescence (GIXF), as schematically outlined in figure 1.2 (B).

1.2. Spatio-Temporal Dynamics of Biological Interfaces: Adhesion and Migration of Human Haematopoietic Stem Cells

Cell membranes do not only serve as a protective layer, but also provide reaction sites for many biochemical reactions, such as molecular recognition, signalling, and the pathway for migration processes. Cell migration is not only relevant for simple, unicellular organisms, but also involved in essential processes in highly developed metazoans, such as collective cell movement during morphogenesis. During migration, cells generate active forces to their surrounding micro-environments by protruding and retracting cell membranes under rhythmic deformation.[20–24]

In chapter 5, adhesion and spatio-temporal dynamics of cells are experimentally investigated by the combination of various microscopic techniques. Moreover, quantitative parameters extracted from experimental data are compared with a theoretical model of self-propelled, deformable particles. Under the collaboration with Prof. A. D. Ho and Prof. C. Müller-Tidow (Internal Medicine V, University Hospital Heidelberg), I investigated the influence of external factors, such as clinical agents for leukaemia therapy, on the dynamic deformation and motion of human haematopietic stem cells (hHSCs).

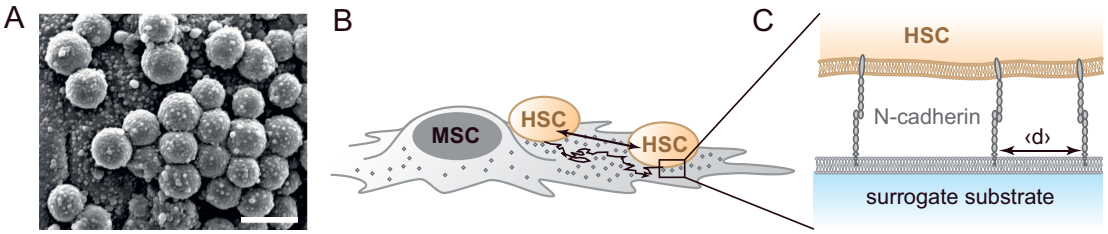

Figure 1.3.: Outline of *in vitro* experiments. **(A)** Scanning electron microscopy image from Schmal *et al.*[34] of hHSC adhering to MSC after 4 days of co-culture, scale bar 10 µm. **(B)** Schematic illustration of hHSC migrating on the surface of MSC displaying ligand molecules. **(C)** Zoom-in of quantitative model of MSC surface, functionalised with ligand molecule N-cadherin at defined surface density.

In the bone marrow, hHSCs adhere to the surface of mesenchymal stem cells (MSCs) and remain in a non-differentiated state.[25–29] The balance between self-reproduction and differentiation of hHSCs is adjusted by migration cycles between the bone marrow and the blood stream. In leukaemia, cancerous stem cells, known as leukaemic stem cells (LSCs), evade this cycle and reproduce as non-differentiated cells, called blasts, in the bone marrow. The resulting overpopulation of blasts causes the suppression of normal haematopoiesis, leading to the death of patients by cytopenia.[30] Since clinical treatments, such as chemotherapy, cannot reach the LSC pool inside the bone marrow, it is necessary to force the migration of leukaemic stem cells out of the bone marrow. Moreover, also the mobilisation of healthy hHSCs from donor's bone marrow is of great importance. Current leukaemia therapy largely relies on the transplantation of healthy hHSCs collected from donors. Therefore, mobilisation of hHSCs from the donor's bone marrow to the peripheral blood is of great importance for increasing the harvesting efficiency of hHSCs.[31,32]

To date, *in vitro* experiments of human HSC systems are limited by the co-culture of hHSCs and MSCs (cf. figure 1.3 (A)),[33,34] and are mostly depending on qualitative observation by immunofluorescence staining of fixed cells. Therefore, the demand for quantitative, label-free, live-cell imaging platforms has been increasing over the years, in order to aid the investigation of physical principles of stem cell adhesion and migration, and its stimulation by clinical agents.

In this study, a quantitative model of MSC surfaces was used, based on planar lipid membranes displaying ligand molecules at defined surface densities, as displayed in figure 1.3 (C). Those so-called supported membranes[35] were func-

tionalised with N-cadherin, a key ligand molecule for the adhesion of hHSCs, and employed to dissect the role of different ligand-receptor interactions in the presence and absence of clinical agents.

Cadherins are one of the key components of the multiprotein complex connecting neighbouring cells, called the adherens junction.[36–40] Within the adherens junction, the function of the cadherin family includes mechanical coupling and signalling between cells, and thereby regulating cytoskeleton and influencing gene expression, among other mechanisms. On the molecular level, Panorchan *et al.* measured the kinetics of bond rupture under different loading rates using atomic force microscopy, demonstrating a continuous breaking of the N-cadherin bond at 30 – 40 pN, independent from the magnitude of the loading rate of up to >1000 pN/second.[41] In general, N-cadherin is one of the key targets in cancer therapy, because of its high expression on drug resistant tumour cells.[42]

N-cadherin antagonist ADH-1, also known as Exherin, is a peptide-based drug designed to specifically block N-cadherin. Several reports have shown that ADH-1 facilitates the uptake of nanoparticles by cancer cells and the efficiency of the drug delivery to cancerous tissues.[43,44] Furthermore, the administration of ADH-1 is able to cause apoptosis by interrupting endothelial cell adhesion mediated via the homophilic N-cadherin axis.[45] However, there has been no quantitative study on the impact of ADH-1 on N-cadherin mediated adhesion and migration of hHSCs.

***In vitro* experiments** in this work were performed using label-free, non-invasive techniques based on optical microscopy. The static properties of adhesion such as adhesion area and strength of hHSCs to supported membranes functionalised with N-cadherin were quantitatively assessed by two techniques. Adhesion area was investigated using micro-interferometry, where the area of close surface contact is analysed in close proximity to the functionalised substrate without the necessity for fluorescent labels as e.g. for total internal reflection fluorescence (TIRF) microscopy. As illustrated in figure 1.4 (A), in μ-interferometry the area of close surface contact is visible as a dark footprint surrounded by the characteristic Newton's rings, due to the destructive and constructive interference of the reflected polarised light.[46]

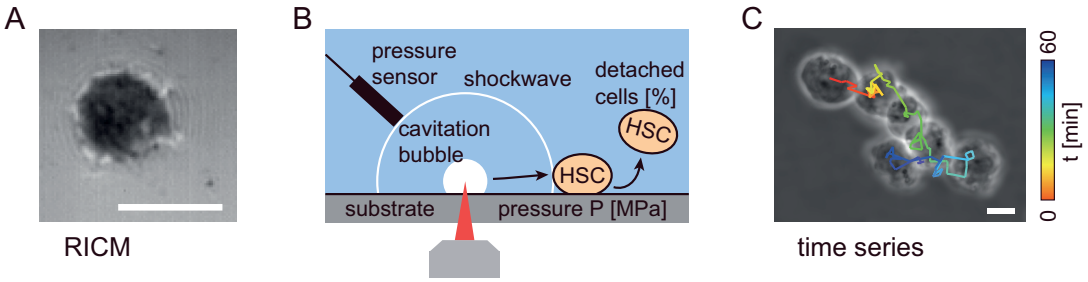

Figure 1.4.: Experimental design of *in vitro* experiments. **(A)** Micro-interferometry image of hHSC adhering to the planar lipid membrane displaying ligand molecules ad defined surface density. **(B)** Schematic principle of laser-pulse induced cell detachment, and **(C)** time-lapse imaging using phase contrast microscopy. Scale bars 5 µm.

For the determination of adhesion strength between cells and substrates, several methods have been developed over the years. Single-cell detachment by micropipette aspiration,[47–51] optical and magnetic tweezers,[52–55] or AFM scratching[56–59] give the advantage of high resolution of detachment forces, but limit the applicability with small force ranges ($10^2 - 10^3$ pN, $10^{-1} - 10^2$ pN, and $10 - 10^4$ pN, respectively), low statistics at high time effort, and mechanical damage to the cells due to the direct contact.[55] Cell detachment via shear stress using flow chambers can provide higher cell numbers with lower time effort, but the slow response time of cells to the applied shear flow also allows elastic deformations, which may alter the applied stress and therefore renders the measured adhesion strength inaccurate. One of the more recent techniques circumventing the deformation of cells at large time scales is the induction of pressure waves via high-powered pico-second laser pulses. Yoshikawa *et al.* introduces an experimental setup,[60] where multi-photon absorption at the focal point of an infrared laser pulse induces the formation of a cavitation bubble through the evaporation of aqueous medium, upon whose collapse a strong pressure wave is created, propagating at supersonic velocity. Figure 1.4 (B) displays the schematic principle of the laser-pulse induced cell detachment. The short exposure to the detachment pressure ensures the prevention of cell deformation, whereby the detachment force can be determined without corruption.

Deformation and motion of hHSCs was monitored by time-lapse imaging using phase contrast microscopy (figure 1.4 (C)). While the start-to-end point observation commonly used for migration experiments in screening studies lacks information on the behaviour of cells during migration,[61] the time-lapse experiments

performed in this work provide detailed insight into the active deformation of hHSC throughout the migration process.

1.3. Theoretical Modelling of Dynamic Deformation and Migration

As described in the previous section, the migration of cells is accompanied by the active deformation of cell membranes. In this study, the spatio-temporal dynamics observed from live-cell imaging are theoretically modelled by generalising the cells as self-propelled, deformable particles as proposed by Otha *et al.*[62–64] Based on the experimental data, periodic deformation and frictional coupling between cells and the substrate are added to the model, which allows the numerical simulation of deformation induced migration, as observed from hHSCs migrating on functionalised substrates.

Starting from static adhesion, a cell on the substrate displaying a specific adhesive protein is viewed as the state of equilibrium for the cell and the corresponding adhesion axis. Proceeding from static adhesion to dynamic deformation and migration requires the introduction of disturbance to the equilibrium, e.g. polymerisation-depolymerisation cycles for rearrangement of the actin filament network.[65] Out of equilibrium, propulsion forces are generated by polymerisation at the leading edge of the cell transferring forces from the cytoskeleton to the substrate, accompanied by depolymerisation at the rear end of the cell causing detachment from the substrate.[66–68] Direct numerical modelling of these processes, however, pose great computational challenges, such as the simulation of flexible interfaces and multi-phase reactive flow.[69–72] Many theoretical studies simulate force generation through the cytoskeleton and dynamic adhesion to ligands on the substrate, but for simplification neglect the occurrence of deformation,[73,74] although most experimental systems show deformation caused by the particle's motion or the exertion of propulsion forces by deformation. On the other hand, Kruse *et al.*[75] simulates the polymerisation-depolymerisation process in terms of an active, polar actin/myosin gel, which describes the shape and motion of lamellipodia including a friction coefficient representing the force exerted to the substrate via adhesion molecules. This model, however, considers the side view of lamellipodia as thin gel layers homogeneous in y-direction, and simulates the one-dimensional time de-

velopment of the height profile $h(x)$ at the leading edge of the lamellipodium.

Other models focus on membrane bending forces, surface tension, and cross-linked actin filament fields in two dimensions.[65,76,77] For example, Shao *et al.* uses the phase-field model of Collins and Levine[78] in the description of cell interior and exterior, separated by a diffuse layer representing the cell membrane. By applying a fourth order non-linear partial differential equation including surface tension, bending force, protrusion force from actin filaments, contraction force, and the effective friction due to adhesion to the substrate, the persistent gliding motion of epithelial keratocytes was successfully modelled. At quasisteady state for the persistent gliding, however, effective friction is compensated by active protrusion and retraction forces, setting the total force between substrate and cell equal to zero.[76] Since in experimental systems regarding the active migration of hHSC, propulsion forces are exerted to the substrate via friction instead of exhibiting persistent gliding, adhesion between cell and substrate needs to be explicitly considered. Another two-dimensional application of the phase-field model introduced by Ziebert *et al.*[65] has shown the simulation of propulsion forces through e.g. polymerisation-depolymerisation cycles. In this report, motion induced at the leading edge was simulated by coupling the cell's shape to the vector field of mean actin filament network orientation ($\equiv$ polarisation). This phase field approach furthermore considers the polarisation of actin filaments and traction forces to the substrate, inducing contractile stress at the rear end of the cell. The resulting anisotropy successfully leads to the modelling of crescent-shaped, migrating cells, as observed in experiments on dynamics of keratocyte cells and cell fragments.[65,79–82] Furthermore, actin protrusion rate, substrate stiffness, and adhesion rate have successfully been implemented to this model.[83] For considerations of distinct polymerisation cycles, however, genetic expression of reporter markers is necessary to follow the reactive processes inside the migrating cells, which is not applicable for the primary human stem cell samples used in this work.

An alternative approach to the simulation of single-cell dynamics is the modelling of collective cell behaviour as presented e.g. by Hiraiwa *et al.*,[84] where by simplification of motility and driving forces, deformation of the particles is excluded. In this model, repulsion and scattering between particles is induced by exclusion effects in 2D under conservation of preferred direction of motion, and dynamic self-organisation of cells can be implemented through inter-cellular con-

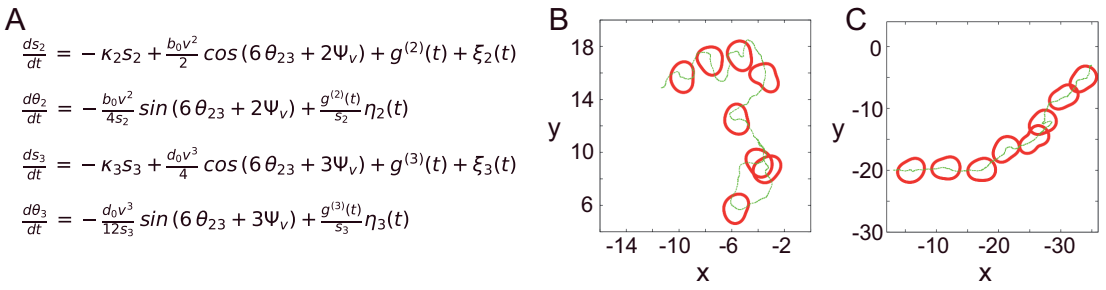

Figure 1.5.: Outline of theoretical model of deformable, self-propelled particles by Ohta *et al.*[63] **(A)** Set of differential equations connecting deformation amplitude s_n and direction θ_n to intrinsic force $g^{(n)}$. **(B)** Trajectory (green) and shape change (red) for the linear model. **(C)** Trajectory (green) and shape change (red) in the presence of non-linearity. Adapted from Ohta *et al.*[63]

tact communication.[85]

An intermediate approach between modelling of intracellular processes and simplified expression of motility and driving forces is presented by Ohta *et al.*[62] In this model, excitable or oscillatory intrinsic forces are connected to the cell's deformation by a set of differential equations, allowing the simulation of migration induced deformation, as well as deformation induced migration, where the velocity of the cell is directly coupled to the friction between cell and substrate.[62–64, 86] Figure 1.5 (A) displays the set of differential equations for deformation amplitude s_n and direction θ_n, alongside two exemplary trajectories for linear (B) and non-linear (C) modelling of deformation induced cell migration.[63]

Throughout this work, deformation and migration of hHSCs is modelled following Ohta *et al.*,[63] in absence and presence of clinical drug ADH-1. In the experiments, frictional coupling between cell and substrate is controlled by lateral density of ligand molecules N-cadherin, and investigated in terms of its influence on the dynamic behaviour in experiment and simulation. Additionally, previously reported results of similar stem cell experiments are further investigated using numerical simulations.

1.4. Aims of this Study

The overarching aim of this thesis is to study the influence of external stimulation on (A) the stability, structure, and electrostatics, and (B) the mechanical properties and dynamic behaviour of biological interfaces. To do so, two sets

of experimental setups are introduced: to determine the stability, structure, and electrostatics of monolayers, a model system representing the outer membrane of Gram-negative bacteria is fabricated at the air-water interface. Using X-ray techniques under synchrotron radiation, the disturbance of the membrane's equilibrium state by surface active molecules is studied within Å resolution. The second system for the investigation of mechanical properties and dynamic behaviour of cell-cell contacts utilises the model system of supported lipid bilayers, mimicking the micro-environment of the human bone marrow niche. By the optical-microscopy based techniques of micro-interferometry, laser-induced detachment, and live-cell imaging, mechanics and dynamics of cell-cell interfaces are analysed, aided by numerical simulations. Within this study, molecules antagonistic to the interface composition are introduced as external stimulus to the model system, allowing the analysis of direct perturbation to the system's single components.

In chapter 4 the stability, structure, and electrostatics of LPS monolayers are studied at the air-water interface, under the influence of external stimuli by BzA and BAC. Section 4.1 presents the results from compressibility analysis, followed by the investigation of structural changes by the addition of BzA (sec. 4.2), BAC (sec. 4.3), and the synergistic effect of both additives (sec. 4.4). Finally, the ion concentration profiles near the interface are presented and analysed in section 4.5.

Mechanical properties and dynamic behaviour of HSCs on surrogate substrates displaying cell adhesion molecule N-cadherin are investigated in chapter 5. The influence of clinical drug ADH-1, antagonistic to N-cadherin, is analysed in section 5.1, wherefore in section 5.1.1, adhesion area and strength measured by μ-interferometry and laser pulse detachment are presented. Deformation and migration of HSCs are presented and analysed in sections 5.1.2 and 5.1.3, connecting experimental results and numerical simulations. In section 5.2, the results from unpublished experiments regarding deformation and migration of HSCs on various surface densities of N-cadherin are reconstructed using numerical simulations. Finally, section 5.3 presents the theoretical modelling of HSC dynamics under the influence of NOX-A12, based on the experimental study from Monzel *et al.*[87]

2. Theoretical Background

To study the influence of external stimulation on the stability, structure, electrostatics, and dynamics of biological interfaces, two sets of experimental setups are introduced. Section 2.1 presents the basic introduction to the X-ray technique of X-ray reflectivity (XRR), followed by grazing incidence X-ray fluorescence (GIXF) in section 2.2 for determination of stability, structure, and electrostatics of monolayers at the air-water interface.

For experiments on interactions at the cell-cell interface, the theoretical background of micro-interferometry will be introduced in section 2.3, followed by laser-induced cell detachment (sec. 2.4), shape analysis (sec. 2.5), and migration analysis (sec. 2.6). Finally, in section 2.7 the theory of deformation induced migration of self-propelled particles[63,86] is presented.

2.1. X-Ray Reflectivity XRR

For the investigation of liquid surfaces and interfaces, most experimental techniques in real space are not applicable due to the fluidity of the sample, or the limited resolution of the technique. To overcome this obstacle, surface scattering techniques utilising synchrotron radiation are introduced in the following section, obtaining reciprocal-space information even from complex layered structures on atomic scale. Furthermore, the resolution of the chosen technique not only reached down to several Å, but also covers the thickness of whole structures, reaching the range of µm. Therefore, detailed structures close to the surface as well as characteristics of buried structures of stratified layers can be obtained with high resolution and sensitivity. In the following section, the basic interactions of X-rays with matter will be introduced, alongside with the basic properties and theoretical background of the scattering technique, starting from the single, smooth interfaces towards rough, multi-layered systems.[88]

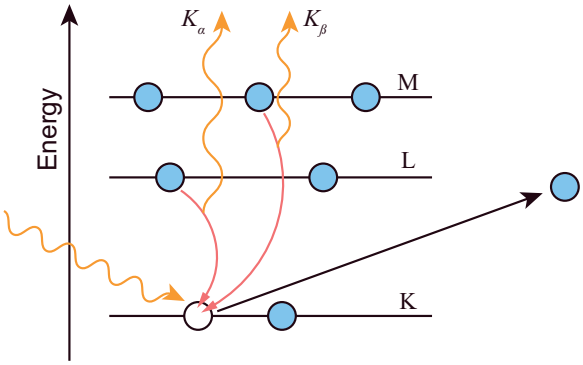

Figure 2.1.: Schematic description of photoelectric absorption of X-rays. Electron from an outer shell (L or M) filling a hole created in the inner K shell by X-ray absorption, under the emission of K_α or K_β radiation.[25]

X-Rays and Matter

X-ray photons of wavelength $\lambda \sim$ Å and wave number $k = \frac{2\pi}{\lambda}$ are able to interact with matter in two different ways: first, by absorption the X-ray photon causes the ionisation of an atom by energy transfer to the interacting electron, creating a hole in the inner shell (e.g. K). If the hole is filled from an outer shell under emission of a photon, this process is described as fluorescent X-ray emission. Dependent on the source shell of the outer electron, the emitted radiation is classified as the K_α line (transition L $\rightarrow$ K), or K_β (transition M $\rightarrow$ K). Since this radiation is element specific and depends on the atom's abundance in the material interacting with the X-ray, this footprint is widely used to estimate the concentration of certain elements in a sample, or to identify the elemental composition of unknown materials. In addition, to provide depth information about the the fluorescent emission, X-ray fluorescence under grazing incidence angles (GIXF) can be used. Further details about this method will be given in section 2.2. However, if the radiation emitted in the process is immediately re-absorbed by a valence electron, the valence electron can be ejected from the atom as an Auger electron.

The second type of interaction between X-rays and matter is scattering. Here, the photon (incident, λ^+) causes the electrons to oscillate due to its oscillating electric and magnetic field, by which the scattered wave (λ_{sc}) is radiated from the oscillating electrons. This process classically occurs elastic, with $\lambda^+ = \lambda_{sc}$, and is widely used for the structural analysis of materials. The details of this method will be given in the following paragraphs. In the occurrence of energy transfer to the

electron (quantum mechanics, $\lambda^+ < \lambda_{sc}$), the scattering is described as inelastic scattering such as the Compton effect.[25]

Refraction, Reflection, and Scattering

For X-rays, the interaction with matter is dominated by atoms and their electrons, depending on the energy of the radiation and the composition of the material. One of the characteristic properties of a material is the refractive index, that defines the interaction with photons based on its composition of atoms and electrons. The behaviour at the interface between two media of different refractive indices n_1 and n_2 can be described by Snell-Descartes' laws

$$n_1 \cos \alpha^+ = n_2 \cos \alpha_{sc}, \tag{2.1}$$

with the incident and scattered angles α^+ and α_{sc} between the X-ray and the surface. Note that this definition in X-ray optics is different from the conventional definition relative to the surface normal in visible optics. Furthermore, events of reflection and transmission are characterised by Fresnel's coefficients.[89] Therefore, the refractive index provides a link between radiation propagation and interaction with matter by representing a model of continuous medium for the behaviour of atomic scattering.[25,90]

In X-ray crystallography, the plane wave E and the corresponding scattering wave vector transfer $\boldsymbol{q}$ are defined as

$$E \propto e^{+\mathrm{i}\,(\omega t - \boldsymbol{k}\cdot\boldsymbol{r})} \tag{2.2}$$

$$\boldsymbol{q} = \boldsymbol{k}_{sc} - \boldsymbol{k}^+ \tag{2.3}$$

with incident and scattered wave vectors $\boldsymbol{k}^+$ and $\boldsymbol{k}_{sc}$, respectively. Using the description of the scattered amplitude $e^{i\,\boldsymbol{q}\cdot\boldsymbol{r}}$ from the Born approximation and the electron density $\rho(\boldsymbol{r})$, the structure factor in X-ray crystallography is determined in the form of:

$$f(\boldsymbol{q}) = \int \rho(\boldsymbol{r})\, e^{\mathrm{i}\,\boldsymbol{q}\cdot\boldsymbol{r}} d^3\boldsymbol{r}. \tag{2.4}$$

In order to describe the behaviour of X-rays at interfaces, the definition of the refractive index

$$n = 1 - \delta - \mathrm{i}\beta \tag{2.5}$$

is used, including its real part $0 < \delta < 1$, and its imaginary part $\beta > 0$. The imaginary part is calculated in dependence on the attenuation coefficient μ at position $\boldsymbol{r}$ in the sample, following $\beta = \frac{\lambda\mu(\boldsymbol{r})}{4\pi}$. Therefore, the refractive index n is dependent on wavelength λ and attenuation coefficient μ.[90]

For electromagnetic waves of energy $E = \frac{hc}{\lambda}$ matching electronic transitions in the scattering material, the refractive index n exhibits resonant behaviour. Furthermore, normal dispersion occurs for radiation below the resonant energy, as it is usually observed for visible light. Above the resonant frequency, however, n decreases with increasing radiation energy. This is typically the case for X-ray radiation, since energies in the range of shell transitions and above are used. Therefore, the unique phenomenon of a refractive index of $n < 1$ can occur.[25]

Furthermore, time dependency is defined by $e^{\mathrm{i}\omega t}$, for monochromatic waves. Following the Helmholtz equation, the propagation of a wave of incident electric field vector $\boldsymbol{E}^+(\boldsymbol{r}) = \boldsymbol{E}^+ e^{\mathrm{i}\boldsymbol{k}^+\cdot\boldsymbol{r}}$ in a medium of refractive index $n(\boldsymbol{r})$ is defined by

$$\nabla^2\boldsymbol{E}^+(\boldsymbol{r}) + |\boldsymbol{k}^+|^2 n^2(\boldsymbol{r})\boldsymbol{E}^+(\boldsymbol{r}) = 0 \tag{2.6}$$

with the magnitude of the wavevector $|\boldsymbol{k}| = 2\pi/\lambda$. Dependent on the position $\boldsymbol{r}$ in the medium, dispersion $\delta(\boldsymbol{r})$ and absorption $\beta(\boldsymbol{r})$ in equation 2.5 can be expressed in terms of the electron density $\varrho(\boldsymbol{r})$ and the linear absorption coefficient $\mu(\boldsymbol{r})$. For X-ray frequencies ω larger than the resonance frequencies ω_j of atoms j in the sample, dispersion and absorption are defined as

$$\delta(\boldsymbol{r}) = \frac{\lambda^2}{2\pi} r_e \varrho(\boldsymbol{r}) \sum_{j=1}^{N} \frac{f_j^0 + f_j'(E)}{Z} \tag{2.7}$$

and

$$\beta(\boldsymbol{r}) = \frac{\lambda^2}{2\pi} r_e \varrho(\boldsymbol{r}) \sum_{j=1}^{N} \frac{f_j''(E)}{Z} = \frac{\lambda}{4\pi}\mu(\boldsymbol{r}) \tag{2.8}$$

with classical electron radius r_e, total number of electrons Z, and forced oscillation strengths of electrons of each single atom $f_j = f_j^0 + f_j'(E) + \mathrm{i}f_j''(E)$ (including dispersion behaviour dependent on radiation energy E). At low incidence angles, the $\boldsymbol{q}$ dependence of f_j^0 gets negligibly small, allowing the approximation via $f_j^0 \approx Z_j$. Furthermore, for a homogeneous medium far away from absorption edges ϱ and μ are considered independent from $\boldsymbol{r}$, which modifies equation 2.5 with eqs.

2.7 – 2.8 to

$$n = 1 - \frac{\lambda^2}{2\pi} r_e \varrho + \mathrm{i}\frac{\lambda}{4\pi}\mu. \tag{2.9}$$

Here, the scattering length density $r_e\varrho$ can be used to define the dispersion of the medium. For X-rays, typical dispersion results in $\delta = \frac{\lambda^2}{2\pi} r_e \varrho \sim 10^{-6}$, and the range of $\beta \sim 10^{-8}$ – 10^{-7} for absorption values.[88]

Single Smooth Interface

For media of refractive index to X-rays of $n = 1 - \delta < 1$, Snell's law of refraction (eq. 2.1) for transmission from an optically denser medium (e.g. vacuum, $n_\mathrm{v} = 1$) to the optically less dense medium ($n < 1$) can be re-written as

$$\cos\alpha_0^+ = (1 - \delta)\,\cos\alpha_t^+. \tag{2.10}$$

For total reflection at the smooth interface, the critical condition for the exit angle of the transmitted wave is at $\alpha_t^+ = 0$, since in X-ray reflectivity the incident angle is defined relative to the surface and not the surface normal. This leads to the re-writing of eq. 2.10 to define the critical incident angle α_c, for which all incident angles $\alpha_0^+ < \alpha_c$ lead to total reflection:

$$\cos\alpha_c = (1 - \delta)\,\cos 0 = 1 - \delta. \tag{2.11}$$

With the small angle approximation of $\cos\alpha_c \approx 1 - \frac{\alpha_c^2}{2}$, eq. 2.11 can be expressed by

$$\cos\alpha_c \approx 1 - \frac{\alpha_c^2}{2} = 1 - \delta \tag{2.12}$$

$$\alpha_c = \sqrt{2\delta} = \lambda\sqrt{\frac{r_e\varrho}{\pi}} \tag{2.13}$$

For total reflection, only a small part of the incident radiation is penetrating into the medium defined by the evanescent field,[88] as will be described in the following paragraphs (cf. equation 2.23).

Fresnel Reflectivity To derive reflection and transmission coefficients at a single smooth interface between two homogeneous media of different refractive indices,

a plane wave $\boldsymbol{E}_0^+(\boldsymbol{r})$ is considered with wavevector $\boldsymbol{k}_0^+$ following

$$\boldsymbol{E}_0^+(\boldsymbol{r}) = \begin{pmatrix} 0 \\ A \\ 0 \end{pmatrix} \exp(\mathrm{i}\boldsymbol{k}_0^+ \cdot \boldsymbol{r}), \qquad \boldsymbol{k}_0^+ = k \begin{pmatrix} \cos\alpha_0^+ \\ 0 \\ -\sin\alpha_0^+ \end{pmatrix}, \tag{2.14}$$

where reflected and transmitted fields $\boldsymbol{E}^-$ and $\boldsymbol{E}_t^+$ with corresponding wavevectors $\boldsymbol{k}^-$ and $\boldsymbol{k}_t^+$ are defined as

$$\boldsymbol{E}^-(\boldsymbol{r}) = \begin{pmatrix} 0 \\ B \\ 0 \end{pmatrix} \exp(\mathrm{i}\boldsymbol{k}^- \cdot \boldsymbol{r}), \qquad \boldsymbol{k}^- = k \begin{pmatrix} \cos\alpha_0^+ \\ 0 \\ \sin\alpha_0^+ \end{pmatrix}, \tag{2.15}$$

$$\boldsymbol{E}_t^+(\boldsymbol{r}) = \begin{pmatrix} 0 \\ C \\ 0 \end{pmatrix} \exp(\mathrm{i}\boldsymbol{k}_t^+ \cdot \boldsymbol{r}), \qquad \boldsymbol{k}_t^+ = \begin{pmatrix} k_{t,x}^+ \\ 0 \\ k_{t,z}^+ \end{pmatrix}. \tag{2.16}$$

From the continuity consideration of the tangential component of E- and B-field at the interface $z = 0$, the well known Fresnel equations[89] of s-polarised waves ($\perp$) are obtained. Reflection coefficient equal to the ratio of reflected amplitude over incident amplitude $r^\perp = \frac{B}{A}$, and transmission coefficient via ratio of transmitted amplitude over incident amplitude $t^\perp = \frac{C}{A}$, are defined using the notation $k_z = \hat{k}$:

$$r^\perp = \frac{\hat{k}_0^+ - \hat{k}_t^+}{\hat{k}_0^+ + \hat{k}_t^+}, \tag{2.17}$$

$$t^\perp = \frac{2\hat{k}_0^+}{\hat{k}_0^+ + \hat{k}_t^+}. \tag{2.18}$$

For p-polarised waves, the refractive index n influences the reflection and transmission coefficients as a squared factor, but since for X-rays $n \approx 1$, the influence of n is negligibly small.[88]

Now, the Fresnel reflectivity $R_\mathrm{F} = |r|^2$ of the reflected wave can be calculated

from the complex transmission angle $\alpha_t = \alpha_{t+} + \mathrm{i}\alpha_{t-}$ following[88]

$$R_\mathrm{F} = \frac{(\alpha_0^+ - \alpha_{t+})^2 + \alpha_{t-}^2}{(\alpha_0^+ + \alpha_{t+})^2 + \alpha_{t-}^2}, \tag{2.19}$$

$$\text{with} \qquad \alpha_{t+/-}^2 = \frac{1}{2}\left[\sqrt{\left((\alpha_0^+)^2 - (\alpha_c)^2\right)^2 + 4\beta^2} \pm \left((\alpha_0^+)^2 - (\alpha_c)^2\right)\right], \tag{2.20}$$

where for large incident angles $\alpha_0^+ >> \alpha_c$ the approximation for $\alpha_0^+ > 3\alpha_c$ results in $R_\mathrm{F} \simeq \left(\frac{\alpha_c}{2\alpha_0^+}\right)^4$. In general, reflectivity is plotted against the z-component of the wavevector transfer, in dependence on incident angle

$$q_z = \frac{4\pi}{\lambda} \sin \alpha_0^+. \tag{2.21}$$

For small $q_z < q_c$, maximum reflectivity of $R_F = 1$ is observed due to the total external reflection.[88]

Penetration Depth For small incident angles $\alpha_0^+ \leq \alpha_c$, the transmitted electric field $\boldsymbol{E}_t^+$ is described by an exponentially decaying wave, due to the complex part of transmission angle $\alpha_t = \alpha_{t+} + \mathrm{i}\alpha_{t-}$, which governs the exponential function

$$E_t^+ = |C|\, e^{\mathrm{i}(k_{0,x}^+ x - kz\alpha_{t+})}\, e^{kz\alpha_{t-}} \tag{2.22}$$

Using the penetration depth

$$\Lambda = \frac{1}{k\alpha_{t-}} = \frac{\lambda}{\sqrt{8}\pi}\left[\sqrt{\left((\alpha_0^+)^2 - (\alpha_c)^2\right)^2 + 4\beta^2} - \left((\alpha_0^+)^2 - (\alpha_c)^2\right)\right]^{-\frac{1}{2}}, \tag{2.23}$$

it can be seen that for small angles $\alpha_0^+ \longrightarrow 0$, the penetration depth Λ_0 loses the dependence from the wavelength λ. Since $\Lambda_0 = \frac{\lambda}{2\pi\alpha_c} = \frac{1}{\sqrt{4\pi r_e \varrho}}$, only the scattering length density and therefore the composition of the medium contributes to the penetration depth. Typical values are in the range of $\Lambda_0 \sim 50\,\text{Å}$, making the small angle scattering highly attractive for fluorescence X-ray emission measurements of surface structures, since the induced fluorescence signal is restricted to originate from regions close to the interface.[91] For large angles $\alpha_0^+ > \alpha_c$, absorption processes in the medium dominate the penetration behaviour, and Λ exhibits a rapid increase. For absorbent materials in the X-ray regime, the maximum value for $\Lambda_{max} = \frac{\lambda}{4\beta}$ lies in the range of $\sim 10^4$ – 10^5Å at incident angle $\alpha_0^+ = \frac{\pi}{2}$.[88]

Rough Interface

Deviating from the ideal case of a smooth interface, experimental samples always exhibit a certain roughness. Therefore, a quasi continuous change in electron density between the two probed materials leads to the effect, that the refractive index does not change discretely, but also continuously. This continuous change can be understood as a set of thin consecutive layers of smaller changes in n. By weighting the z-coordinates of the replacement layer j with certain probability density and using the root-mean-square (rms) roughness σ_j^2, a continuous refractive index profile can be defined as

$$n_j(z) = \frac{n_j + n_{j+1}}{2} - \frac{n_j - n_{j+1}}{2} \operatorname{erf}\left(\frac{z - z_j}{\sqrt{2}\,\sigma_j}\right). \tag{2.24}$$

Using this definition to calculate reflectivity and transmittance leads to the modified Fresnel coefficients, where $\hat{k} = k_z$

$$\tilde{r}_{(j,j+1)} = r_{(j,j+1)} \exp\left(-2\,\hat{k}_j \hat{k}_{j+1}\,(\sigma_j)^2\right) \tag{2.25}$$

and

$$\tilde{t}_{(j,j+1)} = t_{(j,j+1)} \exp\left(\left(\hat{k}_j - \hat{k}_{j+1}\right)^2 \frac{(\sigma_j)^2}{2}\right) \tag{2.26}$$

at a single, rough interface between layers j and $j+1$. For the interface between liquid and vapour, however, the hyperbolic tangent should be applied instead of the error function. The difference to the error function profile lies at $\sim 5\%$.[88]

Stratified Layers

Considering samples of distinct change in refractive index within the depth profile, the continuous refractive index profile is no longer applicable. Instead, scattering from a system of stratified layers is calculated via $N+1$ layers of thickness d_j and refractive index $n_j = 1 - \delta_j + \mathrm{i}\beta_j$, as outlined in figure 2.2. Between the layers, N interfaces are present at positions $z_j \leq 0$, with the first interface at $z_0 = 0$. At each interface j, incident and transmitted waves are defined by amplitude $E^+_{(j)}$ with wavevector $\boldsymbol{k}^+_{(j)}$, and the reflected wave by amplitude $E^-_{(j)}$ with wavevector $\boldsymbol{k}^-_{(j)}$. Now, $E^-_{(j)}$ can be determined either recursively, following the Parratt formalism[92] for calculating $E^-_{(j)}$ from the electric field amplitude from the adjacent, lower

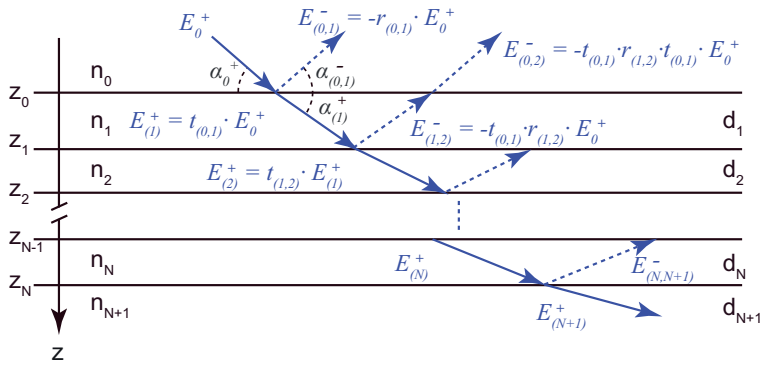

Figure 2.2.: Multiple reflections at stratified layers. Incident wave amplitude E_0^+ under incident angle α_0^+, interacting with N interfaces between $N+1$ layers of thickness d_j and refractive index n_j. Transmitted and reflected wave amplitudes $E_{(j)}^+$ and $E_{(j,k)}^-$, propagating in layer j and indicating the origin of reflection, the interface to layer k. Resulting waves from superposition of multiple reflections will be indicated by $E_{(j)}^-$, resulting in the total reflected wave amplitude E_0^-. Angles of transmission and reflection indicated by $\alpha_{(j)}^+$ and $\alpha_{(j,j+1)}^-$.

layer $E_{(j+1)}^-$, or dynamically, following the equivalent formalism of the propagation matrix between two adjacent layers as introduced by Abelès *et al.*[93,94] Here, we use the propagation matrix from layer j to $j+1$, with the change of phase between layers expressed by $\delta_\pm = \hat{k}_{(j+1)} \pm \hat{k}_{(j)}$, defined as[93–95]

$$\mathbf{P}_{(j,j+1)} = \frac{1}{t_{(j,j+1)}} \begin{bmatrix} \exp\left(\mathrm{i}\,\delta_- z_{(j+1)}\right) & r_{(j,j+1)} \exp\left(-\mathrm{i}\,\delta_+ z_{(j+1)}\right) \\ r_{(j,j+1)} \exp\left(\mathrm{i}\,\delta_+ z_{(j+1)}\right) & \exp\left(-\mathrm{i}\delta_- z_{(j+1)}\right) \end{bmatrix}. \tag{2.27}$$

Since for propagation through consequent layers of different refractive indices the propagation matrices for each interface need to be multiplied, this leads to

$$\begin{pmatrix} E_0^+ \\ E_0^- \end{pmatrix} = \prod_{i=0}^{N} \frac{1}{t_{(i,i+1)}} \prod_{i=0}^{N} \mathbf{P}_{(i,i+1)} \begin{pmatrix} E_{(N+1)}^+ \\ E_{(N+1)}^- \end{pmatrix} = \prod_{i=0}^{N} \frac{1}{t_{(i,i+1)}} \begin{bmatrix} a & b \\ c & d \end{bmatrix} \begin{pmatrix} E_{(N+1)}^+ \\ E_{(N+1)}^- \end{pmatrix}, \tag{2.28}$$

with $\prod_{i=0}^{N} \mathbf{P}_{(i,i+1)} = \left[\begin{smallmatrix} a & b \\ c & d \end{smallmatrix}\right]$.

To define the boundary conditions of the recursion, in layer $j = 0$ (vacuum), E_0^+ is set equal to 1 as incident amplitude. For the bottom edge of the layered structure at $N+1$, no radiation will be reflected due to the limited penetration depth, leaving $E_{(N+1)}^- = 0$.

For determination of the total reflection and transmission coefficients r and t,

Abelès defined the following equations:[93,94]

$$r = \frac{E_0^-}{E_0^+} = \frac{c}{a} \tag{2.29}$$

$$t = \frac{E_{(N+1)}^+}{E_0^+} = \frac{1}{a} \prod_{i=0}^{N} t_{(i,i+1)}, \tag{2.30}$$

where the experimental data yields the reflectivity $R = |r|^2 = \left|\frac{E_0^-}{E_0^+}\right|^2 = \left|\frac{c}{a}\right|^2$.

Finally, as introduced by Abelès, the amplitudes of the transmitted and reflected waves $E^+(z)$ and $E^-(z)$ at depth z in the sample can be calculated from the electric field amplitudes $E_{(j)}^+$ and $E_{(j)}^-$ at interfaces $(j-1, 1)$ and $(j, j+1)$ following

$$E^+(z) = E_{(j)}^+ \exp\left(\mathrm{i}\hat{k}_{(j)}^+ \left(z - \sum_{i=0}^{j-1} d_i\right)\right) \tag{2.31}$$

$$E^-(z) = E_{(j)}^- \exp\left(-\mathrm{i}\hat{k}_{(j)}^- \left(z - \sum_{i=0}^{j-1} d_i\right)\right), \tag{2.32}$$

considering the distance between absolute position z and the absolute position of interface j at $\sum_{i=0}^{j-1} d_i$. Using these expressions in combination with the properties of thickness, electron density, and roughness determined from fitting the experimental reflectivity data, the illumination profile across the stratified layers can be calculated. This is necessary for further investigation of element specific ion distributions in the layered system, as will be presented in the following section.

2.2. Grazing Incidence X-Ray Fluorescence GIXF

As introduced before, reflection and transmission is not the only interaction of X-rays with matter. If the radiation is absorbed by energy transfer to a core electron and the thereby created hole filled by an electron from an outer shell, this transition results in the emission of fluorescence in the X-ray regime. Since the energy of this radiation is equal to the energy difference between the two shells involved in the transition, the emitted fluorescence line is characteristic to the corresponding chemical element. Therefore, fluorescence lines are characterised by the chemical element and its shells involved in the transitions, e.g. for X-ray

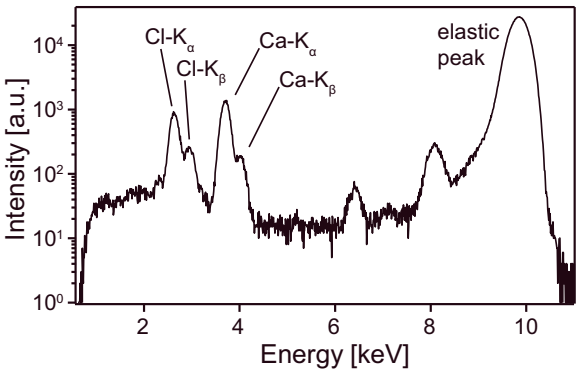

Figure 2.3.: X-ray fluorescence spectrum of pure subphase containing $CaCl_2$, measured at energy $E = 10\,\text{keV}$. Element specific lines of calcium and chloride at Ca–K$_\alpha = 3.7\,\text{keV}$, Ca–K$_\beta = 4.0\,\text{keV}$, Cl–K$_\alpha = 2.6\,\text{keV}$, and Cl–K$_\beta = 2.8\,\text{keV}$, respectively. Incident beam scattered elastically and detected at $E = 10\,\text{keV}$.

fluorescence emitted from a calcium atom, under transition from L to K shell, the line is specified as Ca–K$_\alpha$ as presented in figure 2.3. For the K$_\alpha$ line emitted by an atom of atomic number Z, an approximation for the energy can be made following Moseley's law[25]

$$E_{\text{K}\alpha} \approx 1.017 \times 10^{-2}(Z-1)^2. \tag{2.33}$$

Furthermore, the intensity of the emitted fluorescence is dependent on the abundance of the element in the sample, and on its absorption cross-section. Therefore, the fluorescence spectrum of a sample can be used to analyse its exact, element specific composition, i.e. elements present in the material with the corresponding concentration.

Using the amplitudes of the transmitted and reflected waves $E^+(z)$ and $E^-(z)$ (cf. equations 2.31 – 2.32), the illumination profile across the stratified layers is calculated with high accuracy, due to the small penetration depth of X-rays under small (grazing) incident angles (cf. eq. 2.23). In order to determine the electric field in layer j at depth z, equation 2.28 is separated at $E_{(j)}$ into the following parts:

$$\begin{pmatrix} E_0^+ \\ E_0^- \end{pmatrix} = \prod_{i=0}^{j-1} \frac{1}{t_{(i,i+1)}} \prod_{j=0}^{j-1} \mathbf{P}_{(i,i+1)} \begin{pmatrix} E_{(j)}^+ \\ E_{(j)}^- \end{pmatrix} \tag{2.34}$$

$$\begin{pmatrix} E_{(j)}^+ \\ E_{(j)}^- \end{pmatrix} = \prod_{i=j}^{N} \frac{1}{t_{(i,i+1)}} \prod_{i=j}^{N} \mathbf{P}_{(i,i+1)} \begin{pmatrix} E_{(N+1)}^+ \\ E_{(N+1)}^- \end{pmatrix} \tag{2.35}$$

For simplification, the product of the matrices $\mathbf{P}_{(j,j+1)}$ to $\mathbf{P}_{(N,N+1)}$ is defined as $\prod_{i=j}^{N} \mathbf{P}_{(i,i+1)} = \begin{bmatrix} a_j & b_j \\ c_j & d_j \end{bmatrix}$.

Using the boundary conditions defined in the previous section, equation 2.35 is derived to

$$\begin{pmatrix} E^+_{(j)} \\ E^-_{(j)} \end{pmatrix} = \prod_{i=j}^{N} \frac{1}{t_{(i,i+1)}} \begin{bmatrix} a_j & b_j \\ c_j & d_j \end{bmatrix} \begin{pmatrix} E^+_{(N+1)} \\ 0 \end{pmatrix} \tag{2.36}$$

$$\Rightarrow E^+_{(j)} = a_j \prod_{i=j}^{N} \frac{1}{t_{(i,i+1)}} E^+_{(N+1)} \tag{2.37}$$

$$E^-_{(j)} = c_j \prod_{i=j}^{N} \frac{1}{t_{(i,i+1)}} E^+_{(N+1)}. \tag{2.38}$$

Using the definition of the total transmittance (cf. eq. 2.30) gives the expression for the electric field amplitudes at the interfaces $(j-1, j)$ and $(j, j+1)$ as

$$E^+_{(j)} = \prod_{i=0}^{j-1} t_{(i,i+1)} \frac{a_j}{a} E^+_0 \tag{2.39}$$

$$E^-_{(j)} = \prod_{i=0}^{j-1} t_{(i,i+1)} \frac{c_j}{a} E^+_0. \tag{2.40}$$

The fluorescence intensity of an element at a certain distance from the interface is dependent on the illumination profile of the incident radiation at the same position. From XRR measurements, the illumination profile $I_{ill}(z, \alpha) = |E^+(z, \alpha) + E^-(z, \alpha)|^2$ in a complete set of stratified structures can be calculated in dependence on position z and incident angle α, using the matrix propagation technique, as introduced in section 2.1. Furthermore, the parameters of layer thickness and electron density obtained from XRR analysis are used for further GIXF reconstruction. From this illumination profile $I_{ill}(z, \alpha)$, the fluorescence intensity $I^f_i(z, \alpha)$ from an element i at a distance z from the air-water interface can be written as:

$$I^f_i(z, \alpha) = S \int_0^\infty I_{ill}(z, \alpha)\, c_i(z)\, e^{-z/L_i} dz. \tag{2.41}$$

Proportional constant S is scaled out after the normalisation of fluorescence signals from the sample by fluorescence signal from the blank subphase. Attenuation

of the fluorescence emission between position z and the detector is represented by the exponential term, considering the attenuation length L_i of the subphase at the characteristic fluorescence line i. For fluorescence emitted by e.g. potassium and calcium dissolved in water, the attenuation length of water regarding these chemical elements is $L_{K-K\alpha} = 68.1\,\mu\text{m}$ and $L_{Ca-K\alpha} = 93.7\,\mu\text{m}$.

Finally, to calculate the fitting function for the measured fluorescence intensity profile $I_i^f(z, \alpha)$, the lateral concentration of element i at a depth z is used in the form of:

$$c_i(z) = c_0 + c_{\max} \frac{\sqrt{e}(z - z_{\text{HC}})}{z_{\max}} \exp\left(-\frac{(z - z_{\text{HC}})^2}{2z_{\max}^2}\right). \tag{2.42}$$

Here, the bulk concentration c_0, and the position of interface between hydrocarbon chains and carbohydrate head groups z_{HC} are known from sample preparation and XRR analysis, respectively. The floating parameters of maximum ion concentration $c_{\max}$ and the peak position of the maximum concentration $z_{\max}$ are fitted to match the measured fluorescence intensity by assuming an asymmetric Gaussian distribution, using Levenberg–Marquardt nonlinear least square optimisation.[96] By this method, element-specific ion distributions can be reconstructed within Å resolution, which provides a powerful tool to unravel the electrostatic composition of interfaces.

2.3. Reflection Interference Contrast Microscopy RICM

In order to investigate mechanical properties and dynamic behaviour of hHSCs on surrogate substrates, label-free, non-invasive experimental techniques are of great importance. In the following sections, the basic principles of micro-interferometry, laser pulse detachment, and analysis of live-cell imaging are introduced.

As introduced in section 2.1, an incident beam of light illuminating a sample surface is split at interfaces of different refractive index into reflected and transmitted beams, following Fresnel's law of reflection (cf. eq. 2.17 – 2.18). Using visible, monochromatic light under homogeneous epi-illumination, geometries of objects close to a planar surface can be investigated with micrometer accuracy by the label-free optical technique of Reflection Interference Contrast Microscopy (RICM).[97]

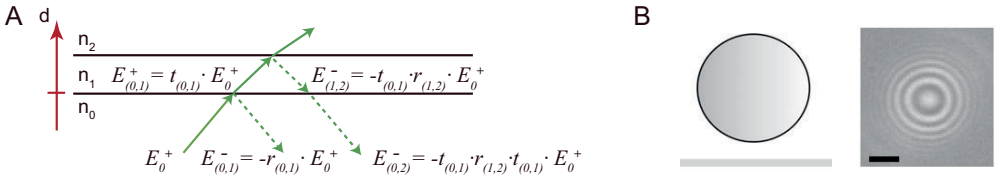

Figure 2.4.: Principle of micro-interferometry. **(A)** Reflection of incident wave E_0^+ at multiple interfaces of different refractive indices n_i. **(B)** Spherical polystyrene bead (diameter 10 µm, left) with respective characteristic interference pattern (right), showing Newton's rings.[99] Scale bar 2 µm.

For simplification, the system of interest is considered as a set of n homogeneous, isotropic layers with parallel interfaces as illustrated in figure 2.4 (A), as introduced for XRR (cf. section 2.1). Considering the superposition of electromagnetic waves reflected at each interface between layers i and $i+1$, with reflection coefficient $r_{(i,i+1)}$ and transmission coefficient $t_{(i,i+1)} = \sqrt{1 - r^2_{(i,i+1)}}$, the total reflected intensity I_{tot} can be expressed following[98]

$$I_{tot} = \left[\boldsymbol{E}^-_{(0,1)} + \boldsymbol{E}^-_{(0,2)} + ...\right]^2 = \left[r_{(0,1)}E_0^+ + (1 - r^2_{(0,1)})r_{(1,2)}E_0^+ e^{-2i\varphi_1} + ...\right]^2, \tag{2.43}$$

where $\varphi_1 ... \varphi_i$ describes the phase shift of the wave after layer i. Re-writing Fresnel's equation 2.17 in terms of refractive indices n_i and angles of reflection $\theta_r = \theta_i^-$ and transmission $\theta_t = \theta_{i+1}^+$, the reflection coefficients $r_{(i,i+1)}$ for waves polarised perpendicular ($\perp$) and parallel ($\parallel$) to the plane of incidence are defined as

$$r^{\perp}_{(i,i+1)}(\theta) = \frac{n_i \cos\theta_i^- - n_{i+1}\cos\theta_{i+1}^+}{n_i \cos\theta_i^- + n_{i+1}\cos\theta_{i+1}^+}, \qquad r^{\parallel}_{(i,i+1)}(\theta) = \frac{n_{i+1} \cos\theta_i^- - n_i\cos\theta_{i+1}^+}{n_{i+1} \cos\theta_i^- + n_i\cos\theta_{i+1}^+}, \tag{2.44}$$

Note that in visible optics, θ is considered in respective to the surface normal, while in section 2.1 for X-ray optics α is defined relative to the surface. The phase shift φ_i is calculated in dependence on the layer thickness d_i, considering Snell's law $\theta_i^- = \sin^{-1}(n_0/n_i \sin\theta_0^+)$ for defining the angle of reflection θ_i^- in terms of incident angle θ_0^+, which yields the expression

$$\varphi_i = \frac{2\pi n_i d_i}{\lambda} \cos\theta_i^- = \frac{2\pi d_i}{\lambda}\sqrt{n_i^2 - n_0^2 sin^2\theta_0^+}. \tag{2.45}$$

Using the definition of equation 2.45 and assuming the negligence of multi-

reflections, the total intensity reflected from a system of multiple layers under quasi-perpendicular illumination of incident angle $\theta_0 = 0$ can be expressed as

$$I_{tot}(x,y) = \left[E_0^+(x,y) \underbrace{\left(r_{(0,1)} + \sum_{i=1}^{m} r_{(i,i+1)} \left[\prod_{j=1}^{i} (1 - r_{(j-1,j)}^2) \, \exp\left(-\mathrm{i} \frac{2\pi}{\lambda} \cdot 2 n_i d_i(x,y) \right) \right] \right)}_{\text{effective reflection coefficient } R} \right]^2 , \tag{2.46}$$

where R represents the effective reflectivity and interference occurs between waves of identical polarisation. Dependent on the local thickness $d_i(x,y)$ at position x, y, inhomogeneities in the layered system are directly identifiable by deviations in the local interference patterns, characterised by the optical path difference $\Delta_i = 2 n_i d_i(x,y)$. In the present work, the functionalised substrate is considered as consisting of parallel, homogeneous layers, whereas the height between substrate and the bottom cell membrane is viewed as a layer of cell medium of inhomogeneous thickness. Arising from the deviations of layer thickness $d_i(x,y)$, the effective reflection coefficient R exhibits minimum and maximum values dependent on destructive and constructive interference for wavelength λ and the optical path difference of

$$\Delta_{dest} = \left(k + \frac{1}{2} \right) \lambda, \qquad \Delta_{const} = k\lambda, \qquad \text{with } k \in \mathbb{Z}. \tag{2.47}$$

In practice, these undulations are visible as the characteristic Newton's rings appearing for spherical objects (cf. fig. 2.4 (B)). In general, for an inhomogeneous layer the reconstruction of the relative height profile is possible, assuming known thickness d_i and refractive index n_i of all layers. Under the application of dual-wavelength RICM,[46] however, even the absolute height profile can be reconstructed, due to the information gained from the parallel use of two different wavelengths.

2.4. Laser-Pulse Induced Cell Detachment

For the determination of adhesion strength between cells and substrates, several methods have been developed over the years, such as single-cell detachment by micropipette aspiration,[47–51] optical and magnetic tweezers,[52–55] or AFM scratch-

ing.[56–59] Due to the disadvantages of small force ranges, low statistics, elastic deformation, and mechanical damage of the cells,[55] one of the more recent techniques circumventing these limitations was chosen for this study. Introduced by Yoshikawa *et al.*,[60] multi-photon absorption at the focal point of an infrared, high-powered pico-second laser pulse ($\lambda = 1064$ nm) induces the formation of a cavitation bubble through the evaporation of aqueous medium, upon whose collapse a strong pressure wave is created, propagating at supersonic velocity. Figure 2.5 (A) displays the schematic principle of the laser-pulse induced cell detachment, with (B) the corresponding positions of adherent (black) and detached (red) cells after exposure to the shock wave propagating from left to right. The short exposure to the detachment pressure ensures the prevention of cell deformation, whereby the detachment force can be determined without corruption. Damage to the cells caused by exposure to aqueous vapour is excluded by estimating the maximum radius of the cavitation bubble[100,101] and removing cells within this radius from analysis. A mathematical description for the propagation of cavitation bubbles yields the relation between wave pressure P and distance from the focus $r(t)$ as:[100–102]

$$P(r(t)) = c_1 \rho_0 v(t) \left(10^{\frac{u(t)-c_0}{c_2}} - 1 \right) + p_\infty, \tag{2.48}$$

with the density of aqueous medium before compression by the shockwave ρ_0, velocity of the shock wave v, sound velocity c_0, hydrostatic pressure p_∞, and the empirical constants $c_1 = 5190\,\mathrm{m/s}$ and $c_2 = 25306\,\mathrm{m/s}$.[103] Using the modified Rayleigh equation, the maximum radius of the cavitation bubble in dependence on its collapse time T_c can be written as[104]

$$R_{max} = \frac{T_c}{0.915} \sqrt{\frac{P_\infty - P_0}{\rho_0}}, \tag{2.49}$$

where the difference between static pressure and vapour pressure inside the cavitation bubble is given by $P_\infty - P_0 = (10^5 - 2330)\,\mathrm{Pa}$ at $20\,^\circ\mathrm{C}$.[105] Considering the boundary of the planar substrate, the collapse time T_c is altered by factor κ, depending on the ratio of distance L between laser focus and boundary, and the cavitation radius R_{max}[106]

$$\kappa = \frac{T_c'}{T_c} = 1 + 0.41 \frac{R_{max}}{2L}. \tag{2.50}$$

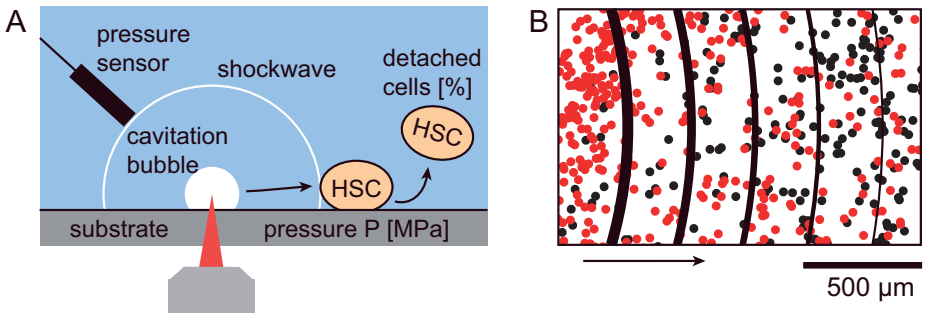

Figure 2.5.: Schematic principle of laser-induced cell detachment.
(A) Detachment of cells by shock wave induced via pico-second laser pulse. Pressure P dependent on distance to position of laser focus, determined via calibration measurement using pressure sensor. **(B)** Positions of adherent (black) and detached (red) cells after exposure to shock wave propagating from left to right (black arrow). Wave fronts of decreasing pressure with increasing distance indicated by black semi-circles of decreasing line thickness.

For simplification, it is assumed that the distance to the rigid boundary of the sample is significantly larger than the radius of the cavitation bubble ($L >> R_{max}$), leading to a value of $\kappa = 1$. Therefore, R_{max} can be estimated by the measurement of the collapse time T_c', as determined to be $\sim 100\,\mu s$ from experiments in the present work.

By inducing pressure via laser power in the range of 1 – 30 mJ, detachment forces applied in the present work are approximately six orders of magnitude larger than those of the aforementioned detachment experiments. Cell statistics in this experiment depend on the size and density of seeded cells. Throughout this work, each sample contained several 1000 cells, that could be analysed after the exposure to one single pressure wave.

2.5. Deformation Analysis

To assess active energy consumption, i.e. by processes such as the bending of membranes and the remodelling of cytoskeletal structures,[107–109] spatial frequency domain analysis is used to quantify the temporal changes of cell shapes and migration. Motility is most commonly viewed as static translation under the negligence of deformation processes.[110–112] In this study, however, not only translation, but also deformation is analysed, using the definition of cell shape in terms of its av-

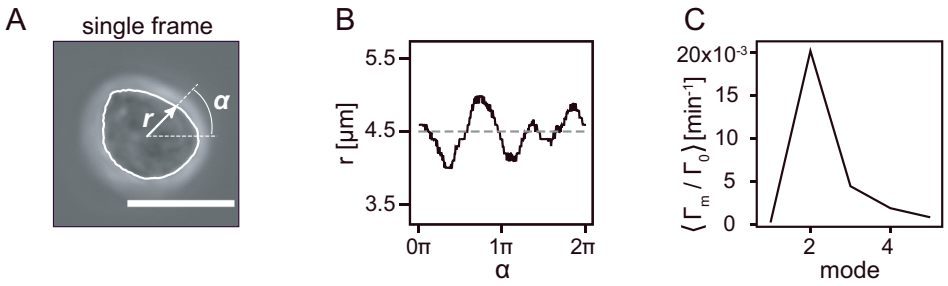

Figure 2.6.: Shape analysis of time lapse experiments. **(A)** Single frame of cell in phase contrast image, indicating cell radius $r(\alpha)$. **(B)** Polar plot of $r(\alpha)$ for determination of contribution from individual modes of deformation, and **(C)** power spectrum of deformation for exemplary single frame.

erage radius r_0 with deviations $\delta r(\alpha, t)$ in space and time, following[113]

$$r(\alpha, t) = r_0(1 + \delta r(\alpha, t)). \tag{2.51}$$

Figure 2.6 (A) presents a single frame from a time series of phase contrast images, displaying the cell radius r in dependence on polar angle α. In panel (B), $r(\alpha)$ is plotted in polar coordinates, including the average cell radius r_0 (dashed line). Treated as a spatio-temporal wave, the normalised shape deviations $\delta r(\alpha, t)$ can be represented by spatial harmonics of sinusoidal frequencies, using Fourier series expansion to calculate the corresponding Fourier coefficients c_m[114]

$$\delta r_m(\alpha, t) = \sum_{m=-\infty}^{\infty} c_m(t) e^{\mathrm{i}m\alpha}. \tag{2.52}$$

For assessing the contribution of each spatial mode m to the overall shape of the cell, the complex fast Fourier transform is utilised to calculate the power spectrum of shape deviation

$$\Gamma_m = \left\langle FT_m\left(\delta r(\alpha, t)\right) \cdot \overline{FT_m\left(\delta r(\alpha, t)\right)} \right\rangle_t. \tag{2.53}$$

Here, time-coefficients for cells with high motility can be calculated by a second, temporal FFT over the temporal fluctuations of the spatial harmonics, where dynamic changes are characterised by the corresponding temporal frequencies.[113] In the present study, however, cells exhibited only a low amount of motility, wherefore the amplitude of temporal changes in spatial harmonics was very low. Therefore,

only the spatial FFT was further analysed, presented by the time-average over one hour of observation time.

In general, spatial frequency domain analysis is sensitive to the cell size, represented by mode $m = 0$. To provide comparability between different experiments and cell types, the power spectrum Γ_m is normalised by the contribution of mode 0, namely Γ_0, excluding effects of isotropic expansion and contraction from analysis. Furthermore, the contribution of translation (mode $m = 1$) is also removed from analysis by the definition of center-of-mass position as the origin in the inertial frame. Due to these normalisation steps, Γ_m is presented in dimensionless units. As presented in fig. 2.6 (C), the normalised power spectrum exhibits amplitudes corresponding to the contribution of each mode to the overall shape. This calculation of power spectral density allows the comparative analysis of cell deformation, since it is proportional to the mechanical power dissipated by morphological dynamics.[115]

For analysis of temporal patterns, exemplary auto-correlation maps were calculated following the auto-correlation function of shape deviations

$$ACF_{\delta r \delta r}(\Delta\alpha, \Delta t) = \frac{\langle \delta r(\alpha + \Delta\alpha, t + \Delta t) \cdot \delta r(\alpha, t) \rangle_t}{\left\langle (\delta r(\alpha, t))^2 \right\rangle_t}, \tag{2.54}$$

where the time period T of oscillatory deformations could be extracted (cf. section 3.6, figure 3.9).

2.6. Migration Analysis

For migration analysis, experiments considering not only start-to-end point determination, but also cell behaviour during migration are of great importance. Experimental systems of migration are typically investigated by performance of time-lapse experiments, from which the center-of-mass position of cells is tracked over time T, with a time interval of Δt. The resulting trajectories are analysed in terms of persistence and mean squared-displacement.

Persistence Following the migration analysis presented by Ohta *et al.*[86] and Svensson *et al.*,[116] trajectories of migrating cells are analysed in terms of persistence. Describing the correlation between velocity $\boldsymbol{v}$ at time points t and $t + \Delta t$,

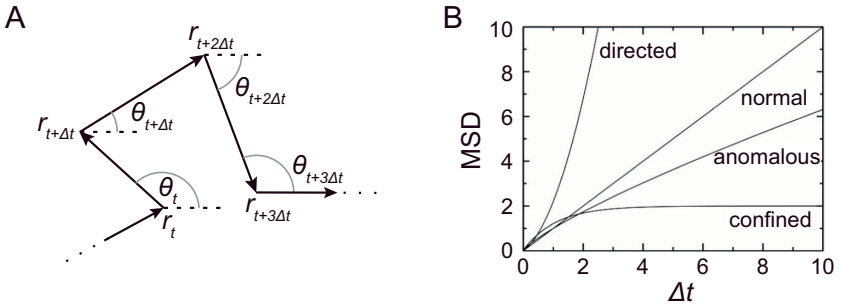

Figure 2.7.: Migration analysis. (A) Exemplary trajectory indicating positions r at time points t and $t+n\Delta t$, with motion between time points at angles $\theta_{t+n\Delta t}$. **(B)** Behaviour of $MSD(\Delta t)$ for different types of migration following $MSD = 4D(\Delta t)^{\alpha}$: supra-linear relation $\alpha > 1$ for directed migration, linear relation $\alpha = 1$ for normal diffusion, i.e. free diffusion, and power-law behaviour $\alpha < 1$ for anomalous diffusion. Exponential relation $MSD \sim -e^{-(\Delta t)}$ for confined diffusion.[117]

the persistence time τ increases with more directed trajectories. For determination of persistence time τ, the autocorrelation function of the direction of motion is calculated using[86]

$$ACF(\Delta t) = \langle cos\,\theta_t \cdot cos\,\theta_{t+\Delta t} + sin\,\theta_t \cdot sin\,\theta_{t+\Delta t} \rangle_t = \exp\left(-\frac{\Delta t}{\tau}\right), \qquad (2.55)$$

where the angle θ describes the absolute orientation of the movement at time t, as depicted in fig. 2.7 (A). Fitted with an exponential decay function, the persistence time τ is determined as the exponential decay time of the ACF. An alternative approach is to analyse the correlation not in time, but in space, which results in the determination of the persistence length.

Mean Squared-Displacement The dynamic properties of a moving object not only result in a typical behaviour of migration direction, but also a characteristic mean squared-displacement (MSD), which can be calculated from the object's trajectory. From the individual positions r_t over a total tracking time T, the MSD is calculated using the following equation:

$$MSD(\Delta t) = \left\langle (\Delta r_{\Delta t})^2 \right\rangle = \frac{1}{T - \Delta t} \sum_{t=1}^{T-\Delta t} (r_t - r_{t+\Delta t})^2 . \qquad (2.56)$$

In order to achieve uniform sampling and equivalent weighting of all segments, the MSD is averaged over all pairs of points with time lag Δt, i.e. total internal

averaging.[118] Figure 2.7 (A) displays an exemplary trajectory with positions r_t and $r_{t+n\Delta t}$, as used to determine the MSD. In panel (B), the different types of migration are displayed with their characteristic curves, which are defined dependent on their time-behaviour following the general form[119]

$$MSD(\Delta t) = 4D(\Delta t)^{\alpha}, \tag{2.57}$$

where D describes the diffusion constant and α the anomalous exponent.

For migration at random walk, the anomaly parameter α is known to be equal to 1, representing the linear behaviour of $\langle r^2 \rangle \sim \Delta t$ labelled as 'normal migration'. This behaviour is most often found in experiments using cells in a 2D-environment in the absence of external stimulation, where the non-directed migration behaviour can be described by Brownian motion.[120]

For values of $\alpha > 1$, migration occurs in a directed behaviour, where the special case of $\alpha = 2$ leads to the linear relation between change in position and time interval $\sqrt{MSD} \sim \Delta t$, characterised as ballistic motion. This type of motion can be expected from cells following mechanical or chemical cues e.g. a chemokine gradient.[121–124]

For a cell in a heterogeneous environment, anomalous or confined migration is observed in most cases. This type of migration may occur in systems, where not all neighbouring sites can be visited with equal probability, due to e.g. inhomogeneities on the substrate or collision with neighbouring cells. Dependent on the environment, the migration behaviour can be described as anomalous, following equation 2.57 at $\alpha < 1$. Another variation of restricted behaviour is described as confined migration, which is mostly found in crowded systems, where collisions with neighbouring objects restrict the path of random walk. To determine the relation between diffusion coefficient D and the geometry and mobility of obstacles, the dynamic behaviour of crowded systems can be defined from Monte Carlo and Brownian dynamics simulations as[117,125–128]

$$MSD(\Delta t) = \langle r_c^2 \rangle \left(1 - A\, e^{-\frac{4BD\Delta t}{\langle r_c^2 \rangle}} \right), \tag{2.58}$$

where $\langle r_c^2 \rangle$ describes the size of the subdomain, within which the observed object is able to migrate, and A and B represent parameters set by the geometry of the domain.

Throughout this work, the diffusion coefficient D of each trajectory is determined by a linear fit to the linear part of each MSD according to equation 2.57 with $\alpha = 1$. Artefacts that occur in the statistical analysis of trajectories are dependent on the length of the trajectories N_T and the number of time steps N_D used for fitting the MSD. In order to minimise the error due to statistical inaccuracies, the fitted region of the MSD curves should be chosen to be 10 - 25% of the total trajectory length, since the number of pairs averaged over is much smaller for large time lags Δt than for short time steps.[118]

Migration Velocity In order to follow previously published results from cell migration experiments, trajectories were further analysed in terms of migration velocity. Therefore, the average migration speed was calculated according to Monzel *et al.* by averaging over the step size in each frame[87]

$$\langle v \rangle_t = \left\langle \frac{\Delta r_{\Delta t}}{\Delta t} \right\rangle_t \tag{2.59}$$

2.7. Theoretical Model of Cell Crawling

To understand self-organisation on a macroscopic scale far from equilibrium, the dynamics of self-propelled particles are of great interest. Many theoretical studies, however, consider force generation through the cytoskeleton and dynamic adhesion to the substrate ligands, but neglect the occurrence of deformation,[73,74] although most experimental systems show deformation caused by the particle's motion or the exertion of propulsion forces by deformation. Other models that focus on membrane bending forces, surface tension, and cross-linked actin filament fields exclude the occurrence of interaction with the substrate,[76] although propulsion forces to the substrate are exerted via friction. Therefore, it is of great importance to consider friction and deformation for modelling the self-propulsion of biological particles.[62]

Throughout this work, single-cell experiments were performed using primary stem cells from umbilical cord blood. Since these cells were used within 6 h after donation, no culturing or molecular markers could be introduced. Therefore, a theoretical model excluding molecular processes was applied to simulate the collision-free migration of single, deformable particles.

In the following section, the principle of the model introduced by Ohta *et al.* will be explained. First, in section 2.7.1 the cell's deformation will be derived from the deformation tensors on the predominant modes of deformation, whereafter the time-evolution of the intrinsic forces will be introduced in section 2.7.2. Finally, the results of the differential equations will be presented in the overall equation of motion in section 2.7.3.

2.7.1. Deformation Tensors

The aim of this model is the simulation of migration, induced by the deformation of biological particles. In general, this type of migration is observed in crawling cells, where elongation in combination with formation of head-tail asymmetry leads to self-propulsion. Using the same definition as introduced in section 2.5 for deformation analysis, the simulated shape of the self-propelled particle is expressed in terms of its average radius R_0 with deviations $\delta R(\alpha, t)$ in space and time

$$R(\alpha, t) = R_0(1 + \delta R(\alpha, t)). \tag{2.60}$$

Treated as a spatio-temporal wave, shape deviations $\delta R(\alpha, t)$ can be represented by a Fourier series determining the Fourier coefficients c_n and the extent of deformation from the circular shape s_n, following[63]

$$\delta R_n(\alpha, t) = \sum_{n=-\infty}^{\infty} c_n(t) e^{\mathrm{i}n\alpha}, \tag{2.61}$$

$$\text{with} \qquad c_n = \frac{s_n}{2}\, e^{\mathrm{i}n\alpha}. \tag{2.62}$$

The motion of deformation and migration in two dimensions is described by the coupling of symmetric, 2nd and 3rd rank deformation tensors[62] $S_{ij} = s(n_i n_j - \frac{1}{2}\delta_{ij})$ and $U_{ijk} = s\left(n_i n_j n_k - \frac{1}{4}\left(\delta_{ij} + \delta_{jk} + \delta_{ki}\right)\right)$ to the velocity components v_k of the center of mass[63]

$$v_k = \gamma S_{ij} U_{ijk}, \tag{2.63}$$

with the components of the unit vector $\boldsymbol{n} = (n_i, n_j)$ in direction of the elongated axis of the simulated cell, $i, j, k \in [1, 2]$, and the mobility γ representing the friction between cell and substrate.

The tensors for elliptical and triangular deformation S_{ij} and U_{ijk} can be rewrit-

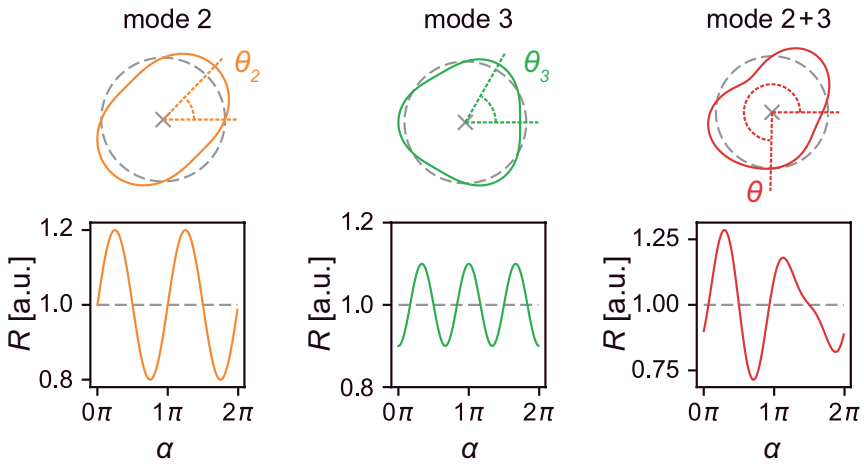

Figure 2.8.: Simulated modes of deformation. Illustration of simulated deformation modes $n = 2, 3$ and combined simulation of mode 2+3 in Cartesian (top) and polar (bottom) coordinates, including simulation angles θ_2, θ_3, and θ. Polar plots of radius $R(\alpha)$ (coloured lines) in arbitrary units, average radius $R_0 = 1$ (broken lines).

ten using the Fourier coefficients defined from the shape of the cell in eq. 2.62. Due to normalisation, the coefficient for isotropic expansion c_0 is removed from the series, and the coefficients for translation $c_{\pm 1}$ are implemented in the velocity of center of mass v_k. With θ_2 and θ_3 defining the direction of the elliptical (mode 2) and triangular (mode 3) deformation, the tensors are rewritten as:[62]

$$S_{11} = c_2 + c_{-2} = 2a_2 \cos 2\theta_2 = -S_{22}, \tag{2.64}$$

$$S_{12} = \mathrm{i}(c_2 - c_{-2}) = 2a_2 \sin 2\theta_2 = S_{21}, \tag{2.65}$$

$$U_{111} = c_3 + c_{-3} = 2a_3 \cos 2\theta_3 = -U_{122} = -U_{212} = -U_{221}, \tag{2.66}$$

$$U_{222} = -\mathrm{i}(c_3 - c_{-3}) = -2a_3 \sin 2\theta_3 = -U_{112} = -U_{211} = -U_{221}, \tag{2.67}$$

where $a_2, a_3 > 0$.

Using this definition, eq. 2.63 can be expressed as

$$v_1 = \gamma[(S_{11} - S_{22})\, U_{111} - 2S_{12}U_{222}] = \gamma[2s_2 s_3 \cos(3\theta_3 - 2\theta_2)], \tag{2.68}$$

$$v_2 = \gamma[(S_{22} - S_{11})\, U_{222} - 2S_{12}U_{111}] = \gamma[2s_2 s_3 \sin(3\theta_3 - 2\theta_2)], \tag{2.69}$$

with $s_2 = 2a_2 > 0$ and $s_3 = 2a_3 > 0$.

The vector components $v_1 = v \cos\theta$ and $v_2 = v \sin\theta$ of velocity $\boldsymbol{v}$ lead to the

expression of amplitude $|v|$ and direction θ of the cell's movement following

$$|v| = 2|\gamma| s_2 s_3, \tag{2.70}$$

$$\theta = 3\theta_3 - 2\theta_2 - \Psi_v. \tag{2.71}$$

The experimentally observed behaviour of the cell following the direction of a broader 'head' instead of a narrow 'tail' after break of symmetry is implemented by the definition of $\Psi_v = 0$ for $\gamma > 0$ and $\Psi_v = \pi$ for $\gamma < 0$.[63] Simulated modes of deformation $n = 2, 3$ are plotted with corresponding simulation angles θ_2, θ_3, and θ in figure 2.8. For calculation of $\boldsymbol{v}$ using equations 2.70 and 2.71, the time evolution of deformation parameters s_2, s_3, θ_2, and θ_3 will be derived in the following section.

2.7.2. Time Evolution and Intrinsic Forces

In order to compute the migration of a cell over time, the time evolution of deformation needs to be defined. This time evolution is implemented in the time-derivatives of the deformation tensors, which are governed by time-dependent intrinsic deformation forces $F_{ij}^{(2)}(t)$ and $F_{ijk}^{(3)}(t)$. Obeying the definition for the time-derivative of velocity $\frac{d}{dt}v_i = \kappa v_i - a|\boldsymbol{v}^2|v_i + a' S_{ij} v_j + a'' S_{ij} U_{ijk}$ including general constants a, a', and a'', the derivation of the deformation tensors are given by[62,63]

$$\frac{S_{ij}}{dt} = -\kappa_2 S_{ij} + b_0 \left(v_i v_j - \frac{\delta_{ij}}{2} v_k v_k \right) + F_{ij}^{(2)}(t), \tag{2.72}$$

$$\frac{U_{ijk}}{dt} = -\kappa_3 U_{ijk} + d_0 \left[v_i v_j v_k - \frac{v_n v_n}{4} \left(\delta_{ij} v_k + \delta_{jk} v_i + \delta_{ki} v_j \right) \right] + F_{ijk}^{(3)}(t). \tag{2.73}$$

The line tension of the cell membrane is represented by the relaxation rates κ_2 and κ_3, which are positive constants defined in eqs. 2.72 and 2.73 with a negative sign. Without changes in the deformation by an intrinsic force, the relaxation rates will cause the shape to return to its relaxed, circular state, at which the equilibrium of $\frac{S_{ij}}{dt} = \frac{U_{ijk}}{dt} = 0$ is reached. The non-linear coupling between direction of deformation and velocity is induced by the constant, non-linear coupling parameters b_0 and d_0, which can be used to introduce persistence to the system. Further non-linear coupling of $U_{ijk} v_n$ and $S_{ij} v_k$ is excluded from this model.[62,63]

To induce deformation, intrinsic force moments $F_{ij}^{(2)}(t)$ and $F_{ijk}^{(3)}(t)$ acting on the cell membrane are introduced. By integrating the forces $f_j(a, t)$ over all positions

a on the cell boundary, the force moments are written as[63]

$$F_{ij}^{(2)}(t) = \int da\, x_i f_j(a,t), \tag{2.74}$$

$$F_{ijk}^{(3)}(t) = \int da\, x_i x_j f_k(a,t). \tag{2.75}$$

For simplification, the force tensors are defined in the same symmetry behaviour as the deformation tensors defined in eqs. 2.64 – 2.67, and can be expressed in terms of time-dependent amplitudes $g^{(n)}(t)$ and phases $\Theta^{(n)}$ by[63]

$$F_{ij}^{(2)}(t) = g^{(2)}(t)\ \cos 2\Theta_{ij}^{(2)}, \tag{2.76}$$

$$F_{ijk}^{(3)}(t) = g^{(3)}(t)\ \cos 3\Theta_{ijk}^{(3)}. \tag{2.77}$$

For constant deformation amplitudes $g^{(2)}$ and $g^{(3)}$, continuous migration would occur at constant elongated shape. Phases $\Theta_{ij}^{(2)}$ and $\Theta_{ijk}^{(3)}$ can either be chosen to match the direction of deformation, i.e. defining the migration to be induced by deformation, or to match the direction of motion, i.e. defining the deformation to be induced by migration. Throughout this work, the first case of deformation induced migration is considered, and the phases are defined as[63]

$$\Theta_{11}^{(2)} = \theta_2, \tag{2.78}$$

$$\Theta_{12}^{(2)} = \theta_2 - \frac{\pi}{2}, \tag{2.79}$$

$$\Theta_{111}^{(3)} = \theta_3, \tag{2.80}$$

$$\Theta_{222}^{(3)} = \theta_3 + \frac{\pi}{2}. \tag{2.81}$$

In general, the computation of deformation induced cell migration is based on the time-dependent amplitudes of deformation forces, where elongation is followed by break of symmetry in a recurring manner. This time behaviour can be realised by defining the deformation force amplitudes e.g. as oscillatory forces or an excitable system of certain time period,[63] and by introducing a phase shift between mode 2 and mode 3 deformation so that mode 3 follows mode 2. Since recent reports[86] as well as experiments performed within the framework of this thesis showed oscillatory behaviour in the deformation patterns of hHSCs, the deformation forces were also defined as oscillatory throughout this work. The time-dependent amplitudes

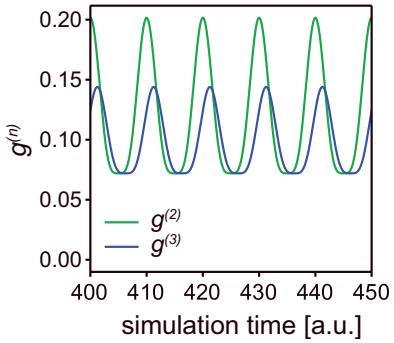

Figure 2.9.: Time evolution of deformation force amplitudes. Amplitudes $g^{(n)}$ of mode 2 (green) and mode 3 (blue) deformation forces with oscillation period $T = 10$ time units and phase shift Φ between modes 2 and 3, over simulation time $400 - 450$ of 500 time units.

of deformation forces are defined as[86]

$$g^{(2)}(t) = g_c^{(2)} + g_0^{(2)} \left(\frac{1 + \cos(\omega t)}{2} \right)^2, \tag{2.82}$$

$$g^{(3)}(t) = g_c^{(3)} + g_0^{(3)} \left(\frac{1 + \cos(\omega t - \Phi)}{2} \right)^2, \tag{2.83}$$

with the offset $g_c^{(n)}$, amplitude $g_0^{(n)}$, and phase shift Φ between mode 2 (elongation) and mode 3 (break of symmetry) oscillations. For simplification, the number of free parameters is reduced by the definition of the offset $g_c^{(2)} = g_c^{(3)} = g_c$ and the amplitude $g_0^{(2)} = 2g_0^{(3)} = 2g_c$ of deformation forces.[86] Time evolution of deformation forces $g^{(n)}(t)$ is plotted in figure 2.9 for mode 2 (green) and mode 3 (blue) over simulation time $400 - 450$, with oscillation period $T = \frac{2\pi}{\omega} = 10$ time units. Note that with a time increment of δt in the simulations 1 time unit [t.u.] $= \frac{1}{\delta t}$ simulation steps.

For reproduction of the stochasticity observed in magnitude and direction of deformation from cell experiments presented in this work, both amplitude $g^{(n)}$ and phase $\Theta^{(n)}$ of the deformation force are introduced to random Gaussian noise. Using the noise terms ξ_n on force amplitude, η_n on force phase, and eqs. 2.78 –

2.81, equations 2.76 and 2.77 can now be rewritten as

$$F_{11}^{(2)} = \left(g^{(2)}(t) + \xi_2(t)\right) \cos 2\left(\theta_2 + \eta_2(t)\right), \tag{2.84}$$

$$F_{12}^{(2)} = \left(g^{(2)}(t) + \xi_2(t)\right) \sin 2\left(\theta_2 + \eta_2(t)\right), \tag{2.85}$$

$$F_{111}^{(3)} = \left(g^{(3)}(t) + \xi_3(t)\right) \cos 3\left(\theta_3 + \eta_3(t)\right), \tag{2.86}$$

$$F_{222}^{(3)} = \left(g^{(3)}(t) + \xi_3(t)\right) \sin 3\left(\theta_3 + \eta_3(t)\right), \tag{2.87}$$

where $\langle \eta_n \rangle = \langle \xi_n \rangle = 0$. For both noise terms, non time-correlated Gaussian noise of amplitude D_ζ is used, following

$$\langle \zeta \rangle = 0, \tag{2.88}$$

$$\langle \zeta(t)\zeta(t') \rangle = D_\zeta^2\, \delta(t - t'). \tag{2.89}$$

For simulations in terms of discrete steps i of time increment δt, also a discretised form of the noise is applied, using the random uniform distribution $G_i \in [-1, 1]$ to define the noise

$$\zeta_i = D_\zeta\, G_i, \tag{2.90}$$

which is numerically accurate for sufficiently small δt.[63,129] The discretised noise term is then implied into the differential equations of general form

$$\frac{dX(t)}{dt} = f(X(t)) + h(X(t))\zeta(t) \tag{2.91}$$

via Euler-Maruyama scheme for discretised simulations, where values of function X at time step $i + 1$ are determined from previous step i by[130]

$$X_{i+1} - X_i = f(X_i)\delta t + D_\zeta G_i h(X_i)\sqrt{\delta t}. \tag{2.92}$$

This stochasticity in the time-evolution of deformation is essential for the simulation of random cell migration.

2.7.3. Differential Equations of Deformation

For calculation of deformation induced migration in the absence of inertia following equation 2.63, the differential equations of $\frac{dS_{ij}}{dt}$ and $\frac{dU_{ijk}}{dt}$ (cf. eqs. 2.72 – 2.73) are expressed using the definitions of migration angle θ (cf. eq. 2.71) and deformation

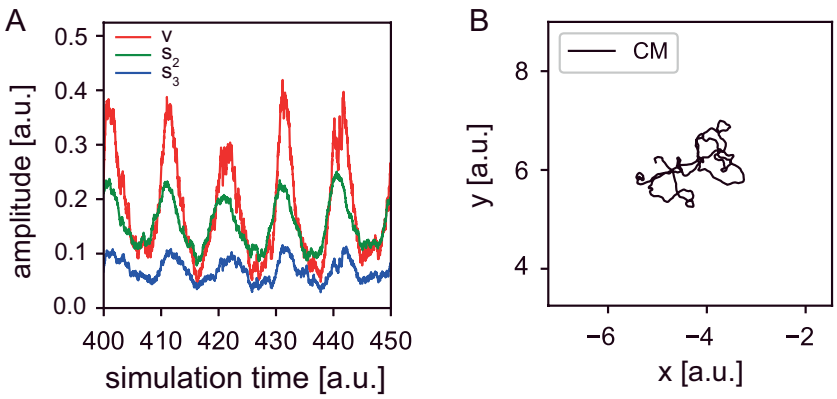

Figure 2.10.: Time evolution of deformation amplitudes, migration velocity, and center of mass position. (A) Amplitudes of mode 2 (green) and mode 3 (blue) deformation, with migration velocity (red) over simulation time $400 - 450$ of 500 time units, and oscillation period of deformation forces $T = 10$ time units. **(B)** Trajectory of center-of-mass position (CM) calculated from velocity $\boldsymbol{v}$ according to $|v| = 2|\gamma|s_2 s_3$ (cf. eq. 2.70) and $\theta = 3\theta_3 - 2\theta_2 - \Psi_v$ (cf. eq. 2.71).

forces $F^{(n)}$ (cf. eqs. 2.84 – 2.87), which yields the set of differential equations for amplitude s_n and orientation θ_n of deformation[62,63]

$$\frac{ds_2}{dt} = -\kappa_2 s_2 + \frac{b_0 v^2}{2}\cos(6\theta_{23} + 2\Psi_v) + g^{(2)}(t) + \xi_2(t), \tag{2.93}$$

$$\frac{d\theta_2}{dt} = -\frac{b_0 v^2}{4s_2}\sin(6\theta_{23} + 2\Psi_v) + \frac{g^{(2)}(t)}{s_2}\eta_2(t), \tag{2.94}$$

$$\frac{ds_3}{dt} = -\kappa_3 s_3 + \frac{d_0 v^3}{4}\cos(6\theta_{23} + 3\Psi_v) + g^{(3)}(t) + \xi_3(t), \tag{2.95}$$

$$\frac{d\theta_3}{dt} = -\frac{d_0 v^3}{12 s_3}\sin(6\theta_{23} + 3\Psi_v) + \frac{g^{(3)}(t)}{s_3}\eta_3(t), \tag{2.96}$$

where $\theta_{23} = \theta_2 - \theta_3$. Relaxation rates κ_2 and κ_3 are positive constants, yielding a stable, circular shape in the absence of intrinsic forces. Front-rear asymmetry of simulated cells is produced by intrinsic forces, and values for $\kappa_{2/3}$ are chosen by results from experimental analysis.[63] The trajectory of center-of-mass position is calculated from initial cell position (x_0, y_0), following the velocity $\boldsymbol{v}$ defined by $|v| = 2|\gamma|s_2 s_3$ (eq. 2.70) and $\theta = 3\theta_3 - 2\theta_2 - \Psi_v$ (eq. 2.71). Figure 2.10 (A) displays an exemplary time evolution of deformation amplitudes s_n and migration velocity $|v|$ over simulation time 400 – 450 of 500 time units, according to oscillatory forces defined in the previous section 2.7.2, alongside with the corresponding trajectory fig. 2.10 (B) calculated from equations 2.70 – 2.71. In the case of persistent

migration, the direction of migration is coupled to the orientation of mode 2 and 3 deformation by the positive non-linear coupling parameters b_0 and $d_0 > 0$. If b_0 and $d_0 < 0$ are defined as negative, migration occurs perpendicular to the elongation axis, as observed e.g. from experiments on Keratocytes.[79] Throughout this work, none of the experimentally obtained trajectories exhibited persistent behaviour, therefore the non-linear coupling parameters were set to $b_0 = d_0 = 0$ for further simulations.

Finally, from the time evolution of amplitudes s_n and directions θ_n of deformation, the cell periphery in polar coordinates is calculated using the angular component $0 \leq \alpha < 2\pi$, following

$$R(\alpha, t) = R_0 \left(1 + \underbrace{s_2(t)\ \cos 2\left(\alpha - \theta_2(t)\right) + s_3(t)\ \cos 3\left(\alpha - \theta_3(t)\right)}_{\delta R(\alpha, t)} \right). \tag{2.97}$$

3. Materials and Methods

3.1. Materials for Characterisation of LPS Ra Monolayers

3.1.1. Buffers

All buffers were prepared using ultrapure water (resistivity R > 18 MΩcm, Merck Millipore, Darmstadt, Germany). Calcium(II)chloride dihydrate ($CaCl_2 * 2\,H_2O$), and potassium chloride (KCl) were purchased from Sigma Aldrich (Munich, Germany), 4-(2-hydroxyethyl)-1-piperazineethanesulfonic acid (HEPES) was acquired from Carl Roth (Karlsruhe, Germany). All chemicals were used without further purification. For preparations of samples at the air-water interface, the following buffers were used:

Ca^{2+}-free buffer:

100 mM KCl, 5 mM HEPES, titrated with KOH to pH 7.4

Ca^{2+}-loaded buffer:

50 mM $CaCl_2$, 5 mM HEPES, titrated with $Ca(OH)_2$ to pH 7.4

3.1.2. Lipopolysaccharide LPS Ra

For experiments at the air-water interface, lipopolysaccharide LPS Ra was used, purified from the bacterial rough strains of *Salmonella enterica* (serovar Minnesota) rough mutant R60.[131] As demonstrated in previous accounts, the use of LPS molecules purified from wild type strains makes the quantitative structural XRR analysis practically impossible due to long, highly polydispersive O-side chains.[7] To overcome the intrinsic heterogeneity of LPS molecules from wild type bacteria, LPS Ra was used due to its uniform saccharide head groups. As presented in figure 3.1 (A), the carbohydrate headgroup of the molecule consists of uncharged

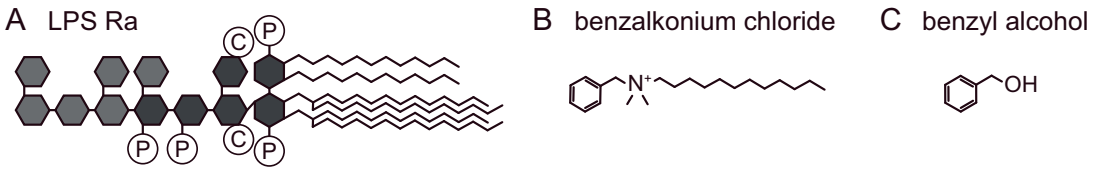

Figure 3.1.: Chemical structures of **(A)** lipopolysaccharide LPS Ra,[132,133] **(B)** benzalkonium chloride (cationic surfactant, BAC),[135] and **(C)** benzyl alcohol (aromatic alcohol, BA).[135]

(light grey, outer core) units, and units carrying negative charges (dark grey, inner core). The outer core of the headgroup is built by one N-acetylglucosamine, two glucose, two galactose, and one heptose unit. The inner core of the headgroup consists of two phosphorylated (Ⓟ) heptose units, and two negatively charged 2-keto-3-deoxyoctonoic acid (KDO, Ⓒ) units. With this full length of core saccharides, LPS Ra shows similar structure to other bioactive wild type LPSs. The remaining part of the LPS molecule (defined as 'lipid A') is built by two negatively charged phosphorylated (Ⓟ) glucosamines and six hydrocarbon chains.[132,133]

LPS Ra was lyophilised as reported by K. Brandenburg and U. Seydel,[133,134] and kindly provided by K. Brandenburg and T. Gutsmann (Research Center Borstel, Leibniz Lung Center, and Brandenburg Antiinfektiva GmbH, Borstel, Germany). The lyophilised powder of LPS Ra was dissolved in a mixture of liquid phenol, chloroform, and petroleum ether at a volume ratio of 2 : 5 : 8. Additionally, small amounts of solid phenol were added until the stock solution was fully transparent, since upon dissolving the solution appeared cloudy. The final concentration was adjusted to 0.7 mg/ml.

3.1.3. Additives

Cationic surfactant benzalkonium chloride (BAC, hydrocarbon chain length n = 12) and aromatic alcohol (benzyl alcohol, BzA) were purchased from Sigma-Aldrich (Munich, Germany). Chemical structures of the additives are presented in figure 3.1. BAC (fig. 3.1 (B)) is composed of one aromatic benzyl ring, one positively charged ammonium group, and an alkyl chain of length n = 12. BzA (fig. 3.1 (C)) consists of one aromatic benzyl ring and one hydroxy group.

For experiments at the air-water interface, buffer solutions were prepared as indicated in figure 3.2 (A). Solutions for (1) Ca^{2+}-free and (2) Ca^{2+}-loaded condi-

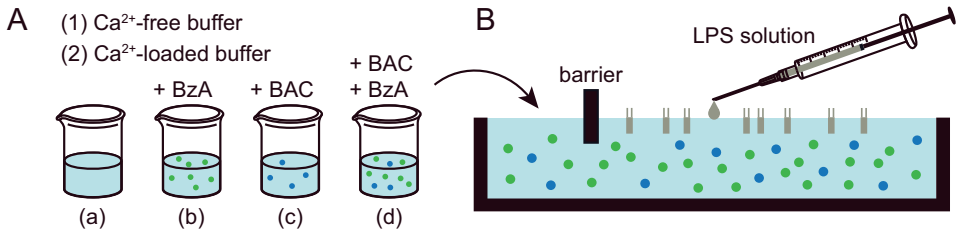

Figure 3.2.: Sample preparation of LPS Ra monolayers. (A) Composition of buffers in (1) absence and (2) presence of Ca^{2+} ions, containing no, single, and combined surface active additives BzA and BAC. **(B)** Spreading of LPS Ra monolayers on the subphase of a Langmuir film balance.

tions were prepared containing (a) no additives, (b) 100 mM BzA, (c) 5 µM BAC, and (d) 100 mM BzA + 5 µM BAC. To ensure maximum homogeneous distribution of surface active additives in the buffer solutions, all buffers were stirred until immediate use.

3.2. Experimental Methods for Characterisation of LPS Ra Monolayers

Experiments at the air-water interface were performed on a Langmuir trough. Prior to adding the subphase and deposition of LPS Ra, the trough was thoroughly cleaned. To ensure the absence of trace amounts of additives or EtOH at the exchange of subphases of different additive composition, the trough was cleaned with EtOH, followed by 10× rinsing with ultrapure water. Details of the membrane preparation are shown in figure 3.2 (B). After filling the Langmuir trough with the subphase, the surface pressure was allowed to equilibrate for $\sim$ 15 minutes, especially in the presence of surface active additives. LPS Ra stock solution was spread on the subphase surface using a Hamilton syringe to form a monolayer. To exclude the influence of trace amounts of organic solvents on the stability of LPS-Ra monolayers, the solvent was allowed to evaporate for 30 minutes prior to all experiments.

3.2.1. Pressure-Area Isotherms

Pressure-area ($\pi - A$) isotherms were recorded using a KSV Nima film balance (Biolin Scientific, Vaestra Froelunda, Sweden) at symmetric compression by a barrier speed of 0.5 mm/min, under constant temperature of 20 °C set by water circulation under the Langmuir trough controlled by a thermostat. By calculating the change in surface pressure $\partial\pi$ over the change in area per molecule ∂A at the air-water interface, the compressibility κ was analysed in terms of it's inverse, the compressional modulus κ^{-1}, following[136,137]

$$\kappa^{-1} = -A\left(\frac{\partial\pi}{\partial A}\right)_T \tag{3.1}$$

at constant temperature T. Dependent on the phase behaviour of the lipid monolayer, the compressional modulus can be categorised into different ranges: in liquid-expanded (LE) phase, κ^{-1} exhibits values between 10 and 50 mN/m, while in liquid-condensed (LC) phase, κ^{-1} ranges from 100 to 250 mN/m.[138,139] This categorisation allows the identification of phase transition of lipid monolayers at the air-water interface.

3.2.2. Simultaneous XRR and GIXF

Simultaneous specular X-ray reflectivity (XRR) and grazing incidence X-ray fluorescence (GIXF) experiments were carried out at beamline ID10 of the European Synchrotron Radiation Facility (ESRF, Grenoble). Prior to measurements, the monolayer was compressed to a surface pressure corresponding to a comparable area per LPS-Ra molecule on Ca^{2+}-free and Ca^{2+}-loaded subphases, namely ~ 200 Å at 20 mN/m for Ca^{2+}-free, and 15 mN/m for Ca^{2+}-loaded subphase. For irradiation, a monochromatic synchrotron beam with a photon energy of either 8 keV or 10 keV ($\lambda_{8\,\mathrm{keV}} = 1.55$ Å, $\lambda_{10\,\mathrm{keV}} = 1.24$ Å) was used. During all measurements, the Langmuir trough was held at a sealed He gas atmosphere to minimise the scattering of the fluorescence emission by air molecules. Furthermore, the stability the surface pressure was monitored throughout all experiments, to ensure identical conditions.

Figure 3.3 shows the experimental setup of simultaneous XRR and GIXF measurements. XRR experiments were performed under incident angles α_i across the

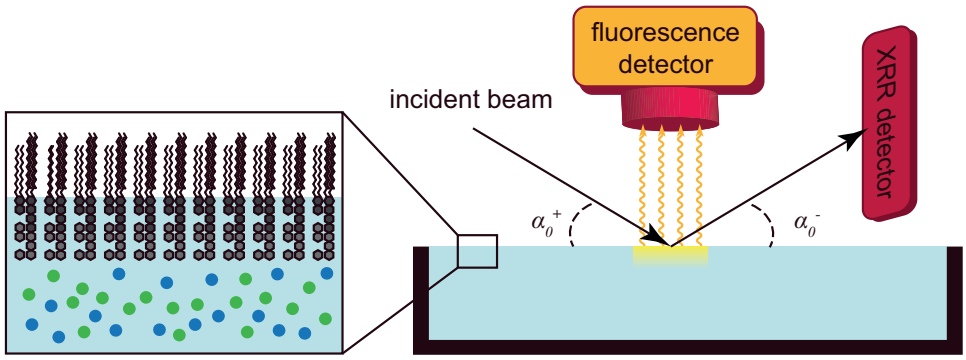

Figure 3.3.: Experimental setup of simultaneous measurement of XRR and GIXF. X-ray reflectivity and fluorescence measurements of LPS Ra monolayers at the air-water interface.

critical angle of total reflection, $\alpha_c = 0.154°$. Signals collected by a linear detector (Mythen 1K, Dectris, Switzerland) were analysed as described in section 2.1 with a genetic minimisation algorithm implemented in the MOTOFIT software package in Igor Pro (WaveMetrics, Portland, OR, USA).[88,140] All parameters extracted by fitting the XRR data were used to calculate the illumination profile for GIXF analysis.

GIXF measurements were carried out using the same settings as for XRR experiments, for each subphase in absence and presence of LPS Ra monolayer. X-ray fluorescence emitted from elements within the illumination volume was recorded using an energy sensitive detector (Vortex, SII NanoTechnology, USA). Intensities from each characteristic, element-specific emission line were normalised by the intensity of the elastically scattered beam, to exclude systematic differences between conditions in the illumination pathway. The normalised intensity of each characteristic line was extracted by fitting the spectra with a self-written multiple Gaussian peak fitting procedure in Igor Pro 6.37 (WaveMetrics, Portland, OR, USA) established by Dr. W. Abuillan.[141] To exclude artefacts from the geometry of the beam footprint or detector aperture, each fluorescence signal in the presence of LPS Ra monolayer was normalised to the corresponding reference measurement on the blank buffer. Due to differences in the beam energy, comparability between experiments was ensured by analysing all data in terms of scattering vector component q_z (eq. 2.21) normal to the interface.

3.3. Materials for Cell Experiments

3.3.1. Buffers and Culture Media

Buffers For buffer preparation, sonication, and rinsing, ultrapure water was used (resistivity R > 18 MΩcm, Merck Millipore, Darmstadt, Germany). Calcium(II)chloride dihydrate ($CaCl_2 * 2\,H_2O$), hydrogen chloride (HCl), sodium chloride (NaCl), and nickel(II)chloride hexahydrate ($NiCl_2 * 6\,H_2O$) were purchased from Sigma Aldrich (Munich, Germany), 4-(2-hydroxyethyl)-1-piperazineethanesulfonic acid (HEPES) was acquired from Carl Roth (Karlsruhe, Germany), and PBS tablets were purchased from Gibco^{TM} (ThermoFisher Scientific Inc., Waltham, USA). All chemicals were used without further purification, and all buffers were filtered using a MCE filter unit (pore size 0.22 µm, Merck Millipore, Darmstadt, Germany) under sterile conditions. For preparations of biological samples, the following buffers were used:

PBS-buffer:

150 mM NaCl, 10 mM phosphate, 2.68 mM KCl, pH = 7.45

HBS-buffer:

100 mM NaCl, 10 mM HEPES, titrated with NaOH to pH 7.4

Ca^{2+}-buffer:

100 mM NaCl, 10 mM HEPES, 1 mM $CaCl_2$, titrated with NaOH to pH 7.4

Ni^{2+}-buffer:

100 mM NaCl, 10 mM HEPES, 5 mM $NiCl_2$, titrated with NaOH to pH 7.4

Culture Media and Supplements Isocove's Modified Dulbecco's Medium (IMDM) and Trypan Blue were purchased from Gibco by Life Technologies (Thermo Fisher Scientific, Waltham, USA). Fetal calf serum (FCS) and horse serum were purchased from Stemcell Technologies Inc. (Vancouver, Canada). Hydrocortisone 100, L-glutamine, and penicillin/streptomycin were purchased from Merck (Sigma–Aldrich Co., St. Louis, USA). Hydrocortisone was reconstituted in ultrapure H_2O at 10 mg/ml and sterilised using MCE filter units (pore size 0.22 µm, Merck Millipore, Darmstadt, Germany). Cytokines FLT3, TPO, SCF, and IL3 were purchased from R&D Systems (Bio Techne, Wiesbaden, Germany). FLT3, SCF, and IL3 were reconstituted at 100 µg/ml in PBS containing 1 mg/ml BSA. TPO was reconstituted at 100 µg/ml in 4 mM HCl containing 1 mg/ml BSA.

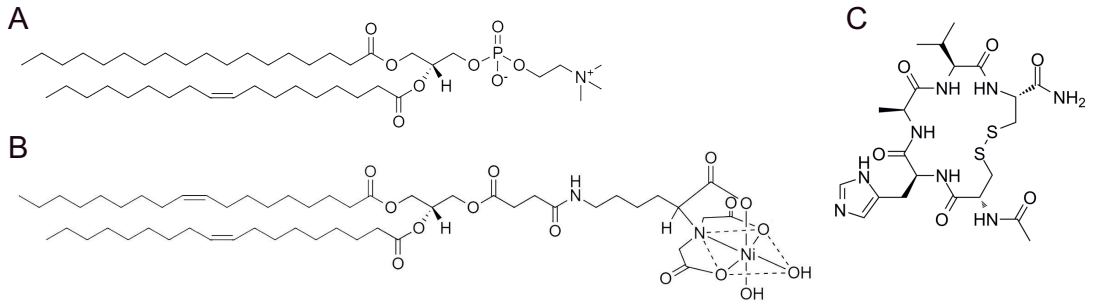

Figure 3.4.: Molecular structures of **(A)** 1-stearoyl-2-oleoyl-*sn*-glycero-3-phosphocholine (SOPC),[142] **(B)** 1,2-dioleoyl-*sn*-glycero-3-[(N-(5-amino-1-carboxypentyl)-iminodiacetic acid) succinyl] (nickel salt) (DGS-NTA (Ni^{2+})),[142] and **(C)** Exherin (ADH-1).[143]

Long-term bone marrow culture (LT-BMC) medium was prepared using 75% IMDM, 12.5% FCS, and 12.5% horse serum, supplemented with 2 mM L-glutamine, 100 U/ml penicillin/streptomycin, 0.05 w% hydrocortisone 100, and 10 µg/l of cytokines FLT3, TPO, SCF, and IL3 each, following the protocol described by Dexter *et al.*[33] All supplement and media aliquots were sterilised, stored at -20 °C, and used within 3 months after first reconstitution of supplements. All media were pre-warmed at 37 °C before further usage. Throughout this work, cells were pre-incubated in LT-BMC, and all cell experiments on surrogate substrates were performed in serum free IMDM.

3.3.2. Lipids and Cell Adhesion Molecules

1-stearoyl-2-oleoyl-*sn*-glycero-3-phosphocholine (SOPC) and 1,2-dioleoyl-*sn*-glycero-3-[(N-(5-amino-1-carboxypentyl)-iminodiacetic acid) succinyl] (nickel salt) (DGS-NTA (Ni^{2+})) were purchased from Avanti Polar Lipids (Alabaster, USA). Both lipids were diluted individually in a mixture of ethanol and chloroform (volume ratio 3 : 7) at a concentration of 5 mg/ml and stored at -20 °C. Molecular structures of SOPC and DGS-NTA are displayed in figure 3.4 (A) and (B). Histidine-tagged human N-cadherin was purchased from R&D Systems (Bio Techne, Wiesbaden, Germany) and diluted in sterile H_2O containing 2 mM calcium, to a stock concentration of 25 µg/ml. SOPC with a molecular weight of 788.13 g/mol was used as matrix lipid to prepare the supported membranes, and DGS-NTA (Ni^{2+}) with a molecular weight of 1057.02 g/mol was used to anchor histidine-tagged human N-cadherin to the phospholipid bilayer.

3.3.3. Clinical Drug ADH-1

Cyclic pentapeptide Exherin / ADH-1 (Adherex Technologies, Durham, NC, USA) was kindly provided by Prof. Dr. A. D. Ho and Dr. R. Saffrich, with the chemical structure presented in fig. 3.4 (C). Designed as a synthetic peptide containing the sequence His-Ala-Val (HAV), ADH-1 has been reported to inhibit N-cadherin-based functions, including cell adhesion.[144,145] Stock solutions of ADH-1 with a molecular weight of 570.69 g/mol were stored at -20 °C and a concentration of 5 ng/µl until further use.

3.4. Sample Preparation for Cell Experiments

3.4.1. Sample Chambers

Glass substrates were cleaned following a modified RCA protocol.[146] In brief, for live-cell imaging and laser detachment assays, respectively, rectangular cover slides of 26 × 76 mm^2 and circular cover slides of ∅ = 28 mm (Gerhard Menzel GmbH, Braunschweig, Germany) were sonicated subsequently in acetone, ethanol, methanol, and ultrapure water for 5 minutes each. Afterwards, the substrates were incubated in 1 : 1 : 5 (v/v/v) H_2O_2 (30%) / NH_4OH (25%) / H_2O for 60 minutes at 60 °C. All glass slides were rinsed 10× with ultrapure water and dried at 70 °C. Bottomless µ-Slide VI 0.4 and bottomless culture dishes of ∅ = 35 mm (Ibidi, Martinsried, Germany) were sonicated subsequently in 2% Hellmanex (neoLab Migge GmbH, Heidelberg, Germany) and ultrapure water for 10 minutes each, rinsed by a total of 10× with ultrapure water, and dried at 70 °C. Glass substrates were sealed to the corresponding sample chambers using polydimethylsiloxane (SYLGARD184, Dow Corning Co., USA) and sterilised under UV light for 30 minutes.

3.4.2. Vesicle Solution

For membrane preparation, vesicle solutions were prepared from lipid stock solutions. For setting the desired average lateral distance $\langle d \rangle$ between anchored proteins, the necessary molar fraction χ of DGS-NTA (Ni^{2+}) anchors within the

SOPC matrix lipids was calculated using[147]

$$\chi = \frac{A_{lipid}}{\langle d \rangle^2}, \tag{3.2}$$

the geometric relation between molar fraction, average distance, and average lipid area $A_{lipid} \approx 65\,\text{Å}$. Solutions of the desired molar fraction were mixed from stock solutions of 5 mg/ml in $CHCl_3$, whereafter the solvent was evaporated under N_2 and vacuum overnight. After re-suspension of the lipids in HBS buffer, small unilamellar vesicles were produced by tip sonication for 30 minutes at 4 W (S3000 tip sonicator, Misonix Inc., Farmingdale, USA). Residual titanium particles detached from the sonicator tip were removed by centrifugation at 13.4×10^3 rcf for 15 minutes (Centrifuge 5415R, Eppendorf Vertrieb Deutschland GmbH, Köln/ Wesseling, Germany).

3.4.3. Membrane Preparation and Functionalisation

For membrane formation via vesicle fusion,[148] vesicle solutions were injected into the sample chambers under sterile conditions and incubated for 60 minutes at 37 °C. To reduce the extension of the seeding area for laser detachment assays, all previously prepared ∅ = 35 mm culture dishes were equipped with a micro-insert 4 well (Ibidi, Martinsried, Germany) prior to vesicle fusion. Excess vesicles were removed by rinsing the chambers with Ni^{2+}-buffer, followed by a 45-minute incubation to saturate the NTA headgroups with Ni^{2+} ions prior to the functionalisation with N-Cadherin. After exchange for Ca^{2+}-buffer, supported membranes were incubated with 10 µg/ml N-cadherin solutions for 12 h at room temperature. Prior to cell seeding, unbound proteins were removed using pre-warmed IMDM, and sample chambers were equilibrated at 37 °C.

3.4.4. Isolation of hHSCs

All experiments within this study were conducted following the guidelines of the ethics committee on the use of human subjects of Heidelberg University. Written consent was obtained for all voluntary donors in accordance with the relevant guidelines and regulations. Human HSCs were derived from umbilical cord blood (CB) and isolated using the Ficoll-Hypaque technique (Merck KGaA, Darmstadt,

Germany) followed by the AutoMACS affinity column (Miltenyi Biotec GmbH, Bergisch-Gladbach, Germany). In short, mononuclear cell (MNC) fractions were isolated from CB samples by density gradient centrifugation (Ficoll-Hypaque technique). Subsequently, $CD34^+$ cells were separated by magnetic microbead labelling and double sorting (AutoMACS). Prior to performing the experiments, hHSCs were separated into two samples (control and test), and allowed to rest for 7 h at 37 °C and 5% CO_2 in long-term bone marrow culture (LT-BMC) medium.

3.4.5. Preparation of Cell Samples

For ADH-1 experiments, 500 ng/ml of soluble ADH-1 were administered to the test portion during the last 2 h of resting in LT-BMC, while control cells remained unaltered. Prior to seeding, LT-BMC was exchanged for serum-free, prewarmed IMDM and cells were seeded into the sample chambers at a density of 1×10^5 cells/cm^2 in the presence and absence of 500 ng/ml soluble ADH-1. All further measurements were performed 2 – 4 h after seeding, and viability of hHSCs was confirmed before and after performing measurements to be $> 90 - 95\%$ by dye exclusion test using Trypan Blue.

3.4.6. Statistics

For all measurements, 3 independent experiments were performed using two samples of control and +ADH-1 each. For RICM and time lapse experiments, 20 – 30 cells were analysed per sample, each corresponding to one datapoint in the boxplots. For the laser detachment assay, 2000 – 2500 cells per experiment were analysed, resulting in the representation of 50 – 700 cells per one bar in the bargraph.

3.5. Experimental Methods for Cell Experiments

3.5.1. Reflection Interference Contrast Microscopy RICM

Reflection interference contrast microscopy (RICM) experiments were performed on an inverted Zeiss Axio Observer Z1 microscope using a laser light source Colibri 7 (Carl Zeiss AG, Oberkochen, Germany) and a 63x/1.25 Antiflex oil-

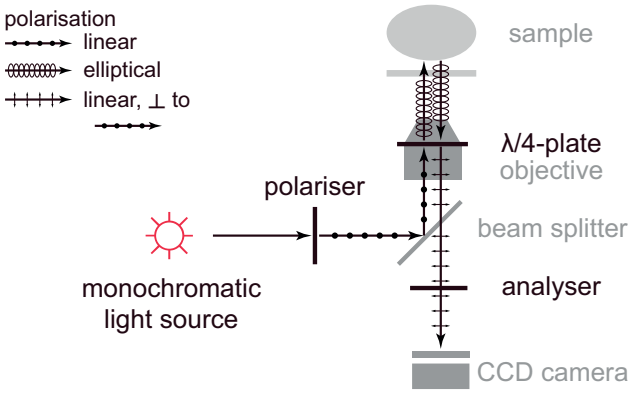

Figure 3.5.: Experimental setup of micro-interferometry. Light path of Antiflex technique[149] for RICM using monochromatic laser light, a polariser, a $\lambda/4$-plate, and an analyser. Adapted from Monzel *et al.*[46]

immersion objective equipped with a built-in $\lambda/4$-plate. Quasi-monochromatic light of $\lambda = 555\,\mathrm{nm}$ was produced with high spatial coherence in direction of the optical axis, where the influence of the optical pathway from the microscopy setup was considered negligible compared to the influence of the sample. Live-cell µ-interferometry was performed using a Stage Top Incubator System (Ibidi, Martinsried, Germany) at 37 °C and 5% CO_2. Sequences of 100 consecutive images of time interval $\Delta t = 30\,\mathrm{ms}$ were acquired 2 h after cell seeding using an Orca ER CCD camera (Hamamatsu Photonics, Hamamatsu, Japan).

For optimisation of experimental realisation, the Antiflex technique is used as introduced by Ploem *et al.*[149] To enhance the contrast of detected intensity, stray light from diffuse origin is filtered out by using perpendicularly arranged polariser and analyser in combination with a $\lambda/4$-plate in the optical path. As illustrated in figure 3.5, incident light is linearly polarised before passing through an Antiflex objective equipped with a $\lambda/4$-plate. The thereby elliptically polarised light receives a phase shift of π upon reflection from interface $(i, i+1)$, whereafter the second passing through the $\lambda/4$-plate causes conversion back to linear polarisation, now perpendicular to the initial wave. Due to the application of the analyser perpendicular to the polariser, stray light from diffuse sources is filtered out from the further light path, and only light reflected from the interface is reaching the detector of the CCD camera.

For high temporal coherence in the incident light, a monochromatic laser is used as light source. For achieving high spatial coherence, Köhler illumination[99]

is applied, using the alignment of collector lens in combination with aperture and field stop. By adjusting aperture and field stop, the illumination aperture $NA_{ill} = n \sin \alpha$ is chosen in dependence on the opening angle α. Matching the geometry of the sample, NA_{ill} has to be set to optimise the dimensions of the depth of field (i.e. sheet of focus plane), and the area of full spatial coherence. In general, both the depth of field and the diameter d of the area of full spatial coherence are defined in reciprocal dependence on NA_{ill}.[150] Furthermore, the lateral resolution δ_R is set by the Rayleigh criterion of[151]

$$\delta_R = \frac{0.61\,\lambda}{NA_{ill}}. \tag{3.3}$$

Therefore, NA_{ill} has to satisfy the requirements of depth of field, spatial coherence, and lateral resolution. For small NA_{ill}, large objects can be analysed utilising the information from deeper and more expanded structures via large depth of field and a large area of full spatial coherence, at the cost of low resolution from high δ_R. Furthermore, the small diameter of the aperture necessary for the small value of NA_{ill} reduces the intensity of the incident light, which reduces the signal-to-noise ratio and therefore the overall contrast. Setting NA_{ill} to high values, small objects close to the interface can be investigated at high resolution (small δ_R), with the advantage of reducing signals from upper layers in the sample, at the cost of a smaller area of full spatial coherence. In addition, however, the larger opening of the aperture provides higher intensity of incident light, enhancing the signal-to-noise ratio and therefore the overall contrast. Throughout this work, NA_{ill} was set to high values, in order to investigate the interface between functionalised substrate and bottom cell membrane at high resolution.

Analysis of RICM images was performed using a self-written procedure in MATLAB 7.7.0 (R2008b), established by Dr. B. Fröhlich.[152] For normalisation, raw image intensity at position x, y was divided by the background intensity from the substrate, averaged over empty positions x', y' in each frame at time-point t

$$\hat{I}_t(x, y) = \frac{I_t(x, y)}{\langle I_t \rangle_{x', y'}}. \tag{3.4}$$

To determine the area of close contact, the gradient images of normalised intensity, averaged over all frames N, are analysed in respect of the gradient maximum

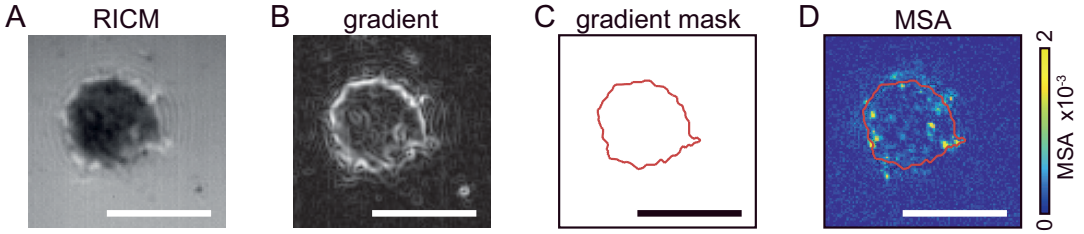

Figure 3.6.: *MSA* analysis of RICM data. **(A)** RICM image with **(B)** corresponding gradient image for determination of area of close contact. **(C)** Mask created by gradient maximum, and **(D)** MSA image for determination of area of tight adhesion. Scale bars 5 µm.

caused by the first change from intensity minimum to maximum in the interference pattern, where d_i changes for the optical path difference from Δ_{dest} to Δ_{const} (cf. eq. 2.47). In figure 3.6, exemplary data is displayed showing the original RICM image (A) with its corresponding gradient image (B) and the image mask (C) determined by maximum gradient. Since the height between substrate and lower cell membrane cannot be reconstructed without dual-wavelength RICM or the knowledge of refractive indices inside the inhomogeneous cytosol, all further analysis is conducted regarding the normalised intensity $\hat{I}$. In the area of tight adhesion, height fluctuations of the lower cell membrane are considered to be very small due to adhesive forces. For small changes in height, a linear change in intensity $\Delta\hat{I}$ is assumed, which is further analysed by the mean squared-amplitude of its fluctuations for N frames, calculated by

$$MSA(x,y) = \frac{1}{N}\sum_{n=1}^{N}\left(\hat{I}(x,y,n) - \langle\hat{I}(x,y)\rangle_n\right)^2. \tag{3.5}$$

Due to the lack of height fluctuations, the pixel area A_{px} of each position x, y is counted as adherent if the corresponding MSA does not exceed an experimentally determined threshold MSA_T, following

$$A_{adh} = \sum_{x=1,y=1}^{x_{max},y_{max}} A_{px}(x,y)\,\Big|_{MSA(x,y)\leq MSA_T}. \tag{3.6}$$

This threshold is dependent on the type of cells under investigation, and typically determined from fully adherent cells, representing average membrane fluctuations without detachment from the substrate. In figure 3.6 (D), a corresponding MSA

image is displayed. For this work, the threshold fluctuation of human HSC was determined to be $MSA_{T,\,\mathrm{hHSC}} = 0.0005$, while previous studies on erythrocytes (red blood cells) yielded $MSA_{T,\,\mathrm{RBC}} = 0.02$.[152] Since intensity fluctuations in the area of close contact can also arise from the movement of structures of inhomogeneous refractive index inside the cells, the area of tight adhesion is corrected for holes created by areas falsely categorised as non-adherent.

3.5.2. Laser-Induced Cell Detachment

Prior to laser detachment experiments, $\varnothing = 35$ mm culture dishes were filled with IMDM before removal of the micro-insert 4 well. For the laser induced cell detachment,[60] a pulsed Nd:YAG laser system ($\lambda = 1064\,\mathrm{nm}$, $\tau_L = 28 \pm 3\,\mathrm{ps}$, EKSLPLA, Vilnius, Lithuania) was coupled to an inverted microscope (Eclipse TE2000-U, Nikon Europe). Throughout all experiments, samples were held at 37 °C using a self-built incubation chamber. As illustrated in figure 3.7 (A), pressure waves were created by the expansion and collapse of cavitation bubbles induced by multiphoton absorption from a picosecond laser pulse. Focus height through a 10× objective was set at 700 µm above the glass substrate at all times. Prior to each experiment, pressure-energy and pressure-distance relations between shock wave P, laser energy E, and distance d from the laser focus position were recorded using a piezoelectric pressure sensor (Müller Instruments, Oberursel, Germany). Resulting calibration curves are presented in figure 3.7 (B) and (C). Fitting functions using the relations of[60]

$$\text{(i)} \quad P \propto E^a \qquad \text{and} \qquad \text{(ii)} \quad P \propto d^{-b}, \tag{3.7}$$

determined the parameters of $a = 0.24$, and $b = 1.25$ and 0.97 for the pressure in the near- and far-field, respectively.[100]

During the experiments, non-adherent cells were removed from the substrate using a weak pressure wave induced by a 0.5 mJ laser pulse. Detachment of adherent cells was induced by laser power of 12.7 mJ, and damage to hHSCs was excluded by positioning the laser focus at a distance from the region of interest that was larger than the maximal possible radius of the cavitation bubble (cf. section 2.4). Before and after each pulse, a 11×14 array of bright field images spanning an area of $5.5 \times 6.5\,\mathrm{mm}^2$ was recorded and manually analysed using Fiji.[153] Cell po-

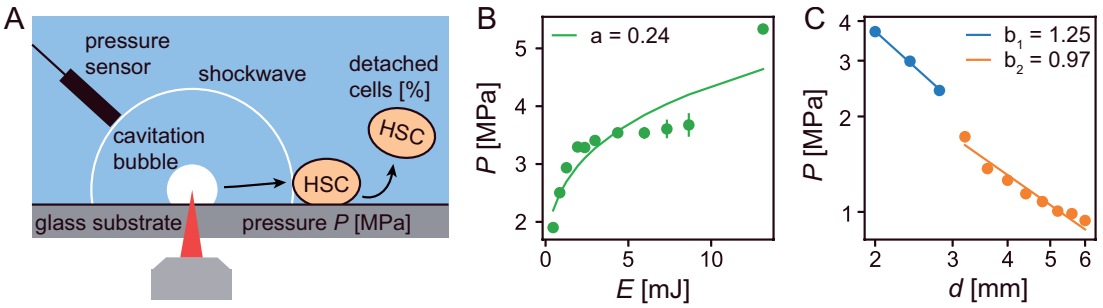

Figure 3.7.: Laser-induced cell detachment. **(A)** Scheme of the experimental procedure for cell detachment via laser-pulse induced shockwave. **(B)** Calibration data of wave pressure P vs. laser energy E, fitted by power-law following eq. 3.7 (i). **(C)** Calibration data of wave pressure P vs. distance d in logarithmic plot, fitted by power-law following eq. 3.7 (ii), in the near- and far-field from the laser focus.[100]

sitions before and after exposure to the pressure wave were determined to classify hHSCs as 'adherent' and 'detached', whereafter the fraction of adherent cells χ_{adh} was calculated in respect to the pressure values P obtained from the distance to the laser focus in bins of equal ΔP, containing 50 – 700 individual cells per bin. Assuming the behaviour of the cell population following a Gaussian distribution of P^* and standard deviation σ, the resulting transition curve from adhesion to detachment was fitted using an adapted error function

$$X_0(P) = A + A \operatorname{erf}\left(\frac{P - P^*}{\sigma}\right), \tag{3.8}$$

with the critical pressure P^* of cell detachment at the inflection point of the curve. Due to the extended transition range between adhesion and detachment, no difference between samples could be identified using the Gaussian peak $P^* \pm \sigma$ determined by the derivative of fitted error function. To test statistical significance between samples and fit curves, the Kolmogorov-Smirnov test for goodness-of-fit[154] was adapted, where the raw data of one condition was tested against the fitted error function of the respective other sample, and *vice versa*. In short, the null hypothesis that the empirical distribution function $\chi(P_i)$ given by the sample data follows the probability distribution $X_0(P_i)$ given by the fitted error function to the respective other sample was rejected at significance level α, if the maximum

difference between $\chi(P_i)$ and $X_0(P_i)$

$$d_{max} = \sup_P \{ \, | \, \chi(P_i) - X_0(P_i) \, | \, , \, | \, \chi(P_{i-1}) - X_0(P_i) \, | \, \} \tag{3.9}$$

exceeded a threshold value d_α corresponding to the significance level α.[155]

3.5.3. Time-Lapse Imaging

Time-lapse experiments were performed on an inverted Axio Observer Z1 microscope (Carl Zeiss AG, Oberkochen, Germany) equipped with a 63x/1.25 Antiflex oil-immersion objective and a Stage Top Incubator System (Ibidi, Martinsried, Germany). Images were recorded 2 – 3 h after seeding at a time interval Δt of 40 – 70 s. Per sample, 10 positions were recorded for the duration of 1 h, and throughout all experiments an atmosphere of 37 °C and 5% CO_2 was maintained.

Image sequences were binarised by hand using Fiji/ImageJ[153] for shape analysis and tracking of the center-of-mass position in Igor Pro 6.37, using self-written procedures established by Dr. A. Yamamoto. All further analysis was performed in Python 3.8 as described in sections 2.5 and 2.6.

Shape Analysis Cell shapes in each frame were analysed in polar coordinates (cf. equation 2.51), from which the power spectrum $\hat{\Gamma}_m$ of shape deviation was calculated via spatial frequency domain analysis (cf. equation 2.53).[22,109,113,156] This approach allows the identification of predominant modes of deformation, alongside with the mechanical power dissipated by deformation processes due to the proportionality to the power spectral density.[86,115]

Migration Analysis Persistence of migration was analysed using the auto-correlation function of the direction of motion (cf. equation 2.55) and fitting for the exponential decay time of persistence τ. From mean squared-displacement MSD (cf. equation 2.56), the diffusion constant D characterising the migration behaviour is calculated by fitting the linear part of each MSD curve according to equation 2.57 with $\alpha = 1$. In order to minimise the error due to statistical inaccuracies, the fitted region was chosen to be 10 - 25% of the total trajectory length.[118]

3.6. Numerical Simulations of Cell Crawling

All simulations were performed using self-written procedures in Python 3.8. Using the Euler method for the numerical, iterative solving of differential equations, the time evolution of deformation was modelled over $N = 50000$ iterations, converted by $\delta t = 0.01$ into $N_T = 500$ time units. In the following, the example code is given for calculating deformation parameters s_n and θ_n of iteration step $[\,\mathrm{i}+1\,]$ from the previous step $[\,\mathrm{i}\,]$ with a time difference of δt:

$$
\begin{aligned}
&\text{for i in range (N} - 1) :\\
&\quad s_2[\,\mathrm{i}\,+\,1\,] = s_2[\,\mathrm{i}\,] - \kappa_2 s_2[\,\mathrm{i}\,]\,\delta t + g_2[\,\mathrm{i}\,]\,\delta t + D_{\xi,2} G_{\xi,2}[\,\mathrm{i}\,]\sqrt{\delta t}\\
&\quad s_3[\,\mathrm{i}\,+\,1\,] = s_3[\,\mathrm{i}\,] - \kappa_3 s_3[\,\mathrm{i}\,]\,\delta t + g_3[\,\mathrm{i}\,]\,\delta t + D_{\xi,3} G_{\xi,3}[\,\mathrm{i}\,]\sqrt{\delta t}\\
&\quad \theta_2[\,\mathrm{i}\,+\,1\,] = \theta_2[\,\mathrm{i}\,] + \frac{g_2[\,\mathrm{i}\,]}{s_2[\,\mathrm{i}\,]} D_{\eta,2} G_{\eta,2}[\,\mathrm{i}\,]\sqrt{\delta t}\\
&\quad \theta_3[\,\mathrm{i}\,+\,1\,] = \theta_3[\,\mathrm{i}\,] + \frac{g_3[\,\mathrm{i}\,]}{s_3[\,\mathrm{i}\,]} D_{\eta,3} G_{\eta,3}[\,\mathrm{i}\,]\sqrt{\delta t}
\end{aligned}
$$

The time evolution of velocity $\boldsymbol{v}$ of each step $[\,\mathrm{i}\,]$ was calculated by

$$
\begin{aligned}
&\text{for i in range (N} - 1) :\\
&\quad v\,[\,\mathrm{i}\,] = 2|\gamma| s_2[\,\mathrm{i}\,] s_3[\,\mathrm{i}\,]\\
&\quad \theta\,[\,\mathrm{i}\,] = 3\theta_3[\,\mathrm{i}\,] - 2\theta_2[\,\mathrm{i}\,] - \Psi_v,
\end{aligned}
$$

followed by the center-of-mass position (x_{cm}, y_{cm})

$$
\begin{aligned}
&\text{for i in range (N} - 1) :\\
&\quad x_{cm}[\,\mathrm{i}\,+1] = x_{cm}[\,\mathrm{i}\,] + v[\,\mathrm{i}\,]\cos\theta[\,\mathrm{i}\,]\,\delta t\\
&\quad y_{cm}[\,\mathrm{i}\,+1] = y_{cm}[\,\mathrm{i}\,] + v[\,\mathrm{i}\,]\sin\theta[\,\mathrm{i}\,]\,\delta t
\end{aligned}
$$

To exclude boundary effects, only the last 90 time steps equiv. to $90 \times 40\,\mathrm{s} = 60\,\mathrm{min}$ were considered in the analysis, and the established model was used without further alteration to the basic principle. For determination of parameters, results from analysis of experiments were considered. As described in the previous section, cell contours and center-of-mass positions were extracted from the time series of live-cell images (fig. 3.8 (A) and (B)) and analysed in polar coordinates (fig. 3.8 (C)). Treating $r(\alpha, t)$ as a spatio-temporal wave, Fourier coefficients could be determined by Fourier expansion, which allowed the calculation of the power spectrum (fig. 3.8 (D)). From the power spectra of the experiments, contribution

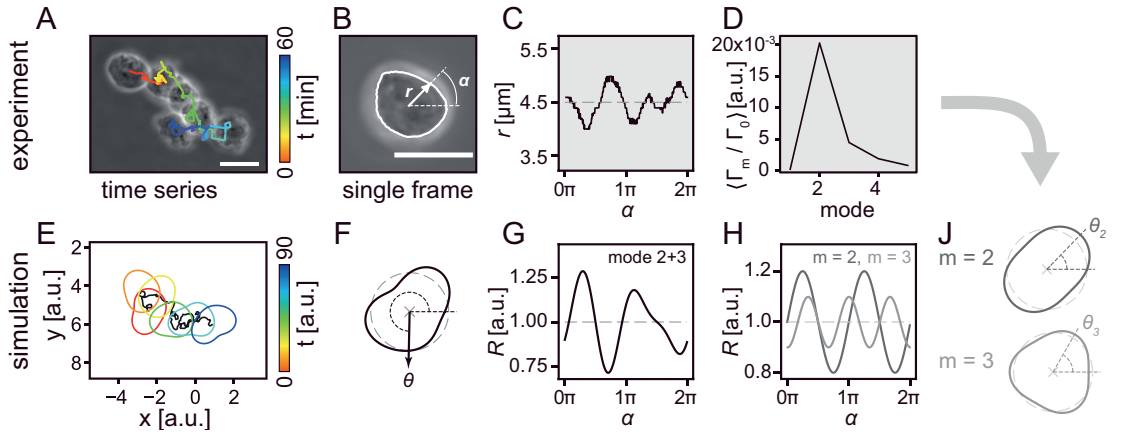

Figure 3.8.: Schematic illustration of procedure from time lapse experiments to simulations. **(A)** Time series and **(B)** single frame of cell migrating on functionalised surface, indicating radius $r(\alpha)$. **(C)** Polar plot of $r(\alpha)$, and **(D)** power spectrum of deformation for exemplary single frame. **(J)** Contribution of single modes 2 and 3 to the particle shape, following the orientation of corresponding angles θ_2 and θ_3. **(H)** Polar plot of single radii from $m = 2, 3$. Overlay of mode 2 and 3 deformation in **(G)** polar and **(F)** Cartesian coordinates, indicating direction of motion θ. **(E)** Simulated time series of particle contour and trajectory, following the results from experimental analysis.

of mode 2 and 3 deformation was extracted, and transferred into contributions of s_2 and s_3 deformation of simulated particles (fig. 3.8 (J) and (H)). Overlaying both modes of deformation following eq. 2.97 resulted in the overall shape of the particle in polar and Cartesian coordinates (fig. 3.8 (G) and (F)). From the time evolution of s_n, θ_n, v, and θ, the time series of deformation induced migration was modelled.

Simulated Length Unit As determined from live cell imaging, hHSCs exhibited average radii of 4.5 – 5.5 µm. Since in all simulations the average cell radius R_0 was set to unity, one simulated length unit corresponds to 5 µm in real units.

Simulated Time Unit In difference to the previously performed simulations of Ohta *et al.*[86] on CXCL12-functionalised substrates, experiments on N-cadherin showed a different scaling in time. Analysis of the auto-correlation function of cell shapes (cf. eq. 2.54) allowed the determination of predominant time period of oscillatory elliptical deformations. Figure 3.9 shows an exemplary ACF map, where the time period of shape changes $T = 10$ min can be read from the time

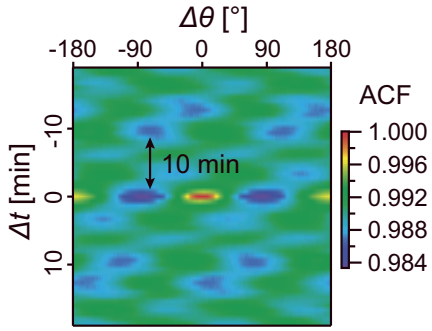

Figure 3.9.: *ACF* map of cell deformation. Colour-map of auto-correlation function of cell shape for determination of time scaling for simulations. Average time period of shape oscillations $T = 7 - 10\,\text{min}$.

interval between correlation minima.

While on CXCL12 cells exhibited oscillatory forces on time scales of $T = 5\,\text{min}$, the average time period of shape oscillations on N-cadherin was determined to be $T = 7 - 10\,\text{min}$, increasing the definition of time unit Δt in the simulations from 30 s to 40 s.

Calculation of Mobility In order to estimate the mobility of simulated cells on the substrates, eq. 2.70 was rearranged to

$$|\gamma_{calc}| = \frac{\langle v \rangle}{2\sqrt{\Gamma_2 \Gamma_3}}. \tag{3.10}$$

From the average $\langle v \rangle$, Γ_2, and Γ_3 of three independent repetitions of cell experiments, $|\gamma_{calc}|$ was calculated to be 8.05 ± 1.80 in the absence, and 11.1 ± 3.4 in the presence of ADH-1.

Intrinsic Force and Line Tension Determination of parameters g_c and κ_2 was performed numerically, for which combinations of values for the two parameters were used to calculate the deformability $\langle s_2^2 \rangle + \langle s_3^2 \rangle$. Results are displayed as a surface plot in figure 3.10 (A), with the colour scaling from $\langle s_2^2 \rangle + \langle s_3^2 \rangle \approx 0.010$ (red) to $\langle s_2^2 \rangle + \langle s_3^2 \rangle \approx 0.040$ (blue). Value pairs of g_c and κ_2 resulting in the correct deformability of $\langle s_2^2 \rangle + \langle s_3^2 \rangle = 0.031 \pm 0.001$ for control simulations, and 0.014 ± 0.01 for simulations in the presence of ADH-1 are plotted in figure 3.10 (B). Linear fit between g_c and κ_2 resulted in $\frac{\kappa_2}{g_c} = 0.09$ for control simulations, and 0.06 for simulations in the presence of ADH-1.

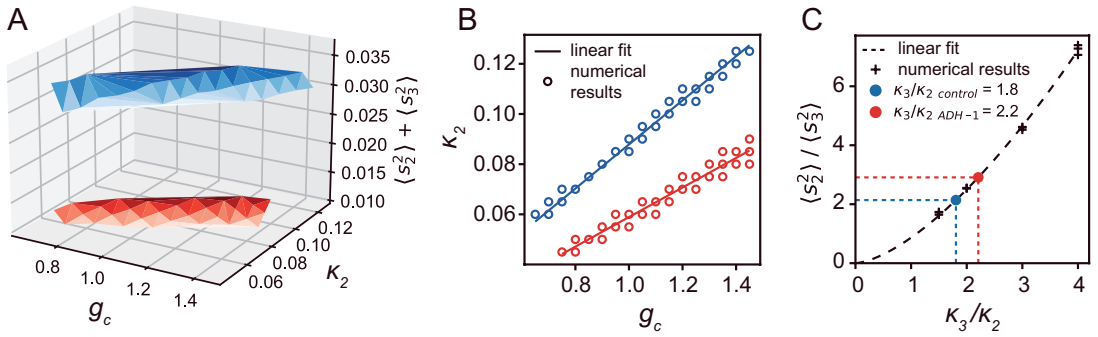

Figure 3.10.: Determination of parameter sets $\frac{\kappa_2}{g_c}$ and $\frac{\kappa_3}{\kappa_2}$. **(A)** 3D plot of results of $\langle s_2^2\rangle + \langle s_3^2\rangle$ from different parameter sets of κ_2 and g_c. **(B)** Scatter plot of $\langle s_2^2\rangle + \langle s_3^2\rangle \approx 0.031$ (blue) for control and $\langle s_2^2\rangle + \langle s_3^2\rangle \approx 0.014$ (red) for +ADH-1, fitted with linear relation between κ_2 and g_c. $\frac{\kappa_2}{g_c} = 0.09$ for control, and $\frac{\kappa_2}{g_c} = 0.06$ for +ADH-1, respectively. **(C)** Plot of ratio $\frac{\langle s_3^2\rangle}{\langle s_2^2\rangle}$ equivalent to $\frac{\Gamma_3}{\Gamma_2}$ from experiments, vs. $\frac{\kappa_3}{\kappa_2}$.

Ratio Between Contribution of Mode 2 and Mode 3 Determination of the ratio between line tensions κ_3 and κ_2 for mode 2 and mode 3 deformation was performed numerically. Simulations were performed for multiple ratios κ_3/κ_2, and corresponding results of $\langle s_2^2\rangle/\langle s_3^2\rangle$ are plotted in fig. 3.10 (C). Power law fit to the numerically determined data points allowed the calculation of necessary ratio κ_3/κ_2 for reaching the desired $\langle s_2^2\rangle/\langle s_3^2\rangle$ corresponding to $\Gamma_2/\Gamma_3 = 2.1$ from control experiments, and 2.9 in the presence of ADH-1. The resulting ratio was determined to be 1.8 for control simulations, and 2.2 for simulations in the presence of ADH-1.

Noise on Amplitude and Direction of Deformation Noise amplitude $D_{\xi,n}$ on amplitude of deformation was chosen to be 0.025 so that no negative velocities were created. Amplitude $D_{\eta,n}$ was set according to simulated migration parameters D, v, and τ, so that simulations matched the experimental results. Best results were achieved by setting $D_{\eta,n} = D_\eta = 0.5$ for both modes 2 and 3.

4. Structural and Electrostatic Characterisation of Lipopolysaccharide Monolayers at the Air-Water Interface

As introduced in chapter 1, the endo-toxicity of LPS displayed at the outer membrane of Gram-negative bacteria is a severe issue in public health. Considering the enhanced survival capability of those bacteria in the presence of divalent cations such as Ca^{2+}, the impact of two components used in sanitisers will be analysed and discussed for Ca^{2+}-free and Ca^{2+}-loaded environment in the present chapter.

To understand the physical mechanism underlying the killing of bacteria, a defined model of the outermost surface of bacteria was fabricated by the deposition of a monolayer of LPS Ra from *Salmonella enterica* (serovar Minnesota) rough mutant at the air-water interface. To investigate the influence of additives on the behaviour and structure of LPS Ra monolayers, surface pressure-area ($\pi - A$) isotherms, X-ray reflectivity experiments, and GIXF measurements were performed on Ca^{2+}-free and Ca^{2+}-loaded subphases, in the presence and absence of various concentrations of benzylalcohol (BzA), benzalkonium chloride (BAC), and combinations of both additives.

4.1. Influence of Additives on Compressibility of LPS Monolayers

In the following section, the influence of additives on the monolayer behaviour of LPS Ra is studied by surface pressure-area ($\pi - A$) experiments. First, in section 4.1.1 the stability of LPS Ra monolayers is presented on Ca^{2+}-free and Ca^{2+}-loaded

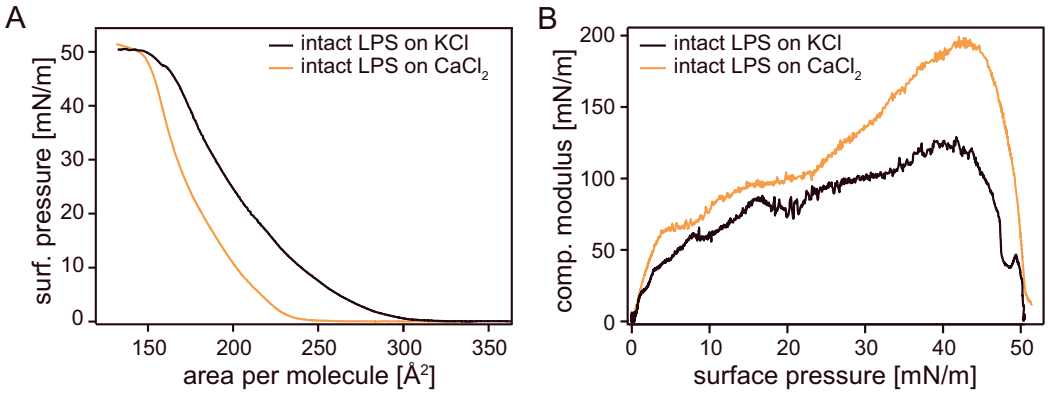

Figure 4.1.: LPS monolayers on subphases without additives. (A) Pressure-area isotherms and **(B)** compressional modulus of LPS Ra in the absence (black) and presence (orange) of Ca^{2+} ions in the subphase.

subphases. Subsequently, the influence of additives is investigated in the absence (section 4.1.2) and presence (section 4.1.3) of divalent Ca^{2+} ions.

4.1.1. Intact Monolayers on Subphases without Additives

In the first step, the impact of Ca^{2+} ions on the stability of LPS Ra monolayers is investigated by recording Langmuir isotherms on subphases containing K^+ (Ca^{2+}-free) or Ca^{2+} (Ca^{2+}-loaded). Figure 4.1 (A) shows pressure-area ($\pi - A$) isotherms of LPS Ra monolayers in the absence (KCl buffer, black) and presence ($CaCl_2$ buffer, orange) of Ca^{2+} ions. In the absence of Ca^{2+}, the onset of the pressure increase upon compression occurs at an area per molecule of $\sim 300\,Å^2$, whereafter the pressure increases continuously to a maximum at $A \sim 150\,Å^2$ with $\pi = 50\,mN/m$, where the collapse of the monolayer is indicated by an abrupt flattening of the curve. In the presence of Ca^{2+} ions, the onset of the pressure increase upon compression occurs at an area per molecule of $\sim 240\,Å^2$, whereafter the pressure increases also continuously until the maximum at $A \sim 150\,Å^2$ with $\pi = 50\,mN/m$, where the monolayer collapses. The shift in the onset of surface pressure change indicates that the the presence of Ca^{2+} ions reduces the range of repulsive interactions between LPS molecules that possess 6 negative charges.

Compressional modulus κ^{-1} calculated from $\pi - A$ isotherms according to equation 3.1 is presented in figure 4.1 (B) in the absence (black) and presence (orange) of Ca^{2+}. In general, LPS Ra monolayers exhibit higher κ^{-1} values in the presence of Ca^{2+} than on Ca^{2+}-free buffer. This reduction of compressibility shows

the enhanced intermolecular interaction between negatively charged head groups and positively charged Ca^{2+} ions. Regions at which the compressional modulus exhibits values of $\sim 100\,mN/m$ indicate that LPS Ra monolayers are in liquid-expanded phase at $\pi \sim 30\,mN/m$ in the absence of Ca^{2+}, and at $\pi \sim 20\,mN/m$ in the presence of Ca^{2+} ions. Further increase of κ^{-1} shows the phase transition to liquid-condensed phase on Ca^{2+}-free subphase at $\pi \sim 35\,mN/m$, and on Ca^{2+}-loaded buffer at $\pi \sim 25\,mN/m$. Maximum values of $\kappa^{-1} \sim 120\,mN/m$ and $\sim 200\,mN/m$ are reached at $\sim 40\,mN/m$ for both samples, whereafter the collapse of the LPS Ra monolayers is indicated by the drop to $\kappa^{-1} = 0$ at $\sim 50\,mN/m$.

4.1.2. Pressure-Area Isotherms in the Absence of Ca^{2+}

To highlight the impact of BzA and BAC on their bactericidal effect, the stability of LPS Ra monolayers is presented in the absence of Ca^{2+} ions, in which condition the bacterial survival is known to be low. Figure 4.2 shows pressure-area ($\pi - A$) isotherms and compressibility analysis of LPS Ra monolayers on Ca^{2+}-free buffer, under the influence of various concentrations of BzA (green curves), BAC (blue curves), and the combined presence of both (purple and red curves).

Influence of BzA Figure 4.2 (A) shows $\pi - A$ isotherms of LPS Ra monolayers on Ca^{2+}-free buffer, in the absence (black), presence of 10 mM (light green), 100 mM (medium green), and 200 mM (dark green) BzA.

When 10 mM BzA is added (light green curve), the pressure increase upon compression starts at larger molecular areas ($\sim 400\,Å^2$), which indicates an interaction between the LPS molecules at larger distances compared to the pure subphase (black curve), caused by the BzA molecules between LPS Ra headgroups. The collapse pressure is reduced to $\sim 40\,mN/m$, relative to the buffer in the absence of LPS Ra monolayer. When the concentration of BzA is increased by a factor of 10 (100 mM, medium green curve), the onset of pressure increase occurs already at areas per molecule $> 500Å^2$. The overall curve is flattened in comparison to the addition of 10 mM BzA, and the collapse pressure of the LPS monolayer is reduced to $\sim 33\,mN/m$, relative to the sole buffer. It should be noted that the condition of 100 mM BzA corresponds to the commonly used concentration in sanitisers.

To test a condition that would completely destabilise the bacterial membrane, the condition of 200 mM BzA was measured (dark green curve). Here, the onset of

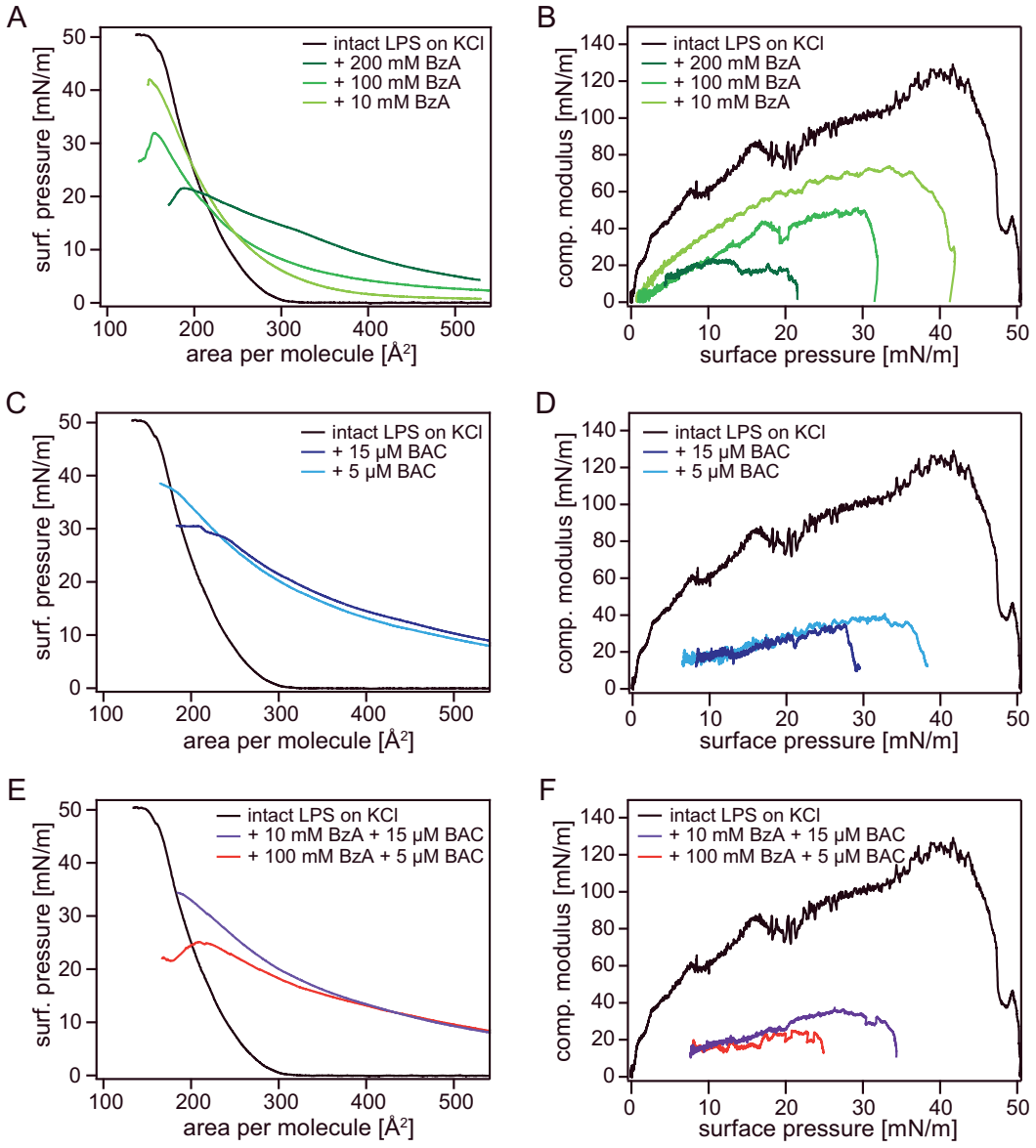

Figure 4.2.: LPS Monolayers on Ca^{2+}-free buffer. **(A)** Pressure-area isotherms and **(B)** compressional modulus in the presence of 10 mM (light green), 100 mM (medium green), and 200 mM (dark green) of BzA. **(C)** Pressure-area isotherms and **(D)** compressional modulus in the presence of 5 µM (light blue) and 15 µM (dark blue) of BAC. **(E)** Pressure-area isotherms and **(F)** compressional modulus in the presence of 10 mM BzA + 15 µM BAC (purple), and in the presence of 100 mM BzA + 5 µM BAC (red).

pressure increase was significantly larger than 500Å^2 per molecule, and the curve was significantly flattened. The collapse of the monolayer occurred at $\sim 22\,\mathrm{mN/m}$, relative to the corresponding subphase without monolayer.

Compressional modulus κ^{-1} calculated from $\pi - A$ isotherms on Ca^{2+}-free buffer is presented in figure 4.2 (B), in the absence (black), presence of 10 mM (light green), 100 mM (medium green), and 200 mM (dark green) BzA. On Ca^{2+}-free buffer, LPS Ra monolayers exhibit a general reduction of κ^{-1} values with increasing concentration of BzA. Maximum values of $\kappa^{-1} \sim 70\,\mathrm{mN/m}$, $\sim 50\,\mathrm{mN/m}$, and $\sim 20\,\mathrm{mN/m}$ are reached at $\sim 35\,\mathrm{mN/m}$, $\sim 30\,\mathrm{mN/m}$, and $\sim 10\,\mathrm{mN/m}$ by increasing concentrations of BzA, respectively. Collapse of the LPS Ra monolayer occurs at $\sim 40\,\mathrm{mN/m}$, $\sim 30\,\mathrm{mN/m}$, and $\sim 20\,\mathrm{mN/m}$, respectively. This successive reduction of compressibility and collapse pressure shows the enhanced intermolecular interaction between negatively charged head groups and BzA molecules, increasing with the concentration of the additive. All samples in the presence of BzA exhibit values of $\kappa^{-1} < 100\,\mathrm{mN/m}$, which indicates that LPS Ra monolayers are in liquid-expanded phase and no transition to liquid-condensed phase is observed.

Influence of BAC Figure 4.2 (C) shows $\pi - A$ isotherms of LPS Ra monolayers on Ca^{2+}-free buffer, in the absence (black), presence of 5 µM (light blue), and 15 µM (dark blue) BAC.

With the addition of 5 µM BAC (light blue curve), the onset of pressure increase is already changed for large areas per molecule $>> 500\,\text{Å}^2$. This indicates a strong interaction between positively charged BAC molecules and negatively charged LPS Ra headgroups. Furthermore, the presence of 5 µM BAC flattens the $\pi - A$ curve significantly, and the collapse pressure is reduced to $\sim 40\,\mathrm{mN/m}$. When the concentration of BAC is increased by a factor of 3 (15 µM, dark blue curve), onset and change of compressibility is not altered compared to 5 µM BAC. The collapse pressure of the LPS monolayer is further reduced to $\sim 30\,\mathrm{mN/m}$.

Compressional modulus κ^{-1} calculated from $\pi - A$ isotherms on Ca^{2+}-free buffer is presented in figure 4.2 (D), in the absence (black), presence of 5 µM (light blue), and 15 µM (dark blue) BAC. On Ca^{2+}-free buffer, LPS Ra monolayers exhibit a significant reduction of κ^{-1} values in the presence of BAC. Maximum values of $\kappa^{-1} \sim 30\,\mathrm{mN/m}$ are reached at $\sim 30 - 35\,\mathrm{mN/m}$ and $\sim 28\,\mathrm{mN/m}$ by increasing concentrations of BAC, whereafter the monolayer almost immediately collapses.

Similar behaviour of compressibility between the different concentrations of BAC indicate that the range of interactions between BAC and LPS Ra headgroups reaches an equilibrium state, independent from concentration. The decrease in collapse pressure, however, leaves room for further investigation about the decrease of stability with increasing BAC concentration.

Synergistic Effect of BzA and BAC In the next step, the influence of the combined presence of the two additives BzA and BAC was investigated. $\pi - A$ isotherms are presented in figure 4.2 (E) with corresponding compressional modulus (F). First, the maximum concentration of 15 µM BAC was combined with the minimum addition of 10 mM BzA (purple curves), to see if the LPS Ra monolayer could further be destabilised. As can be seen by both isotherm and compressional modulus, the addition of 10 mM BzA did not cause major changes to the behaviour compared to the pure presence of 5 and 15 µM BAC. The onset of pressure change upon compression is comparable to that of the single presence of BAC. At molecular areas of $\sim 25 - 30\,\mathrm{mN/m}$, maximum compressional modulus of $\sim 30\,\mathrm{mN/m}$ is reached, whereafter the monolayer collapses at $\pi = 35\,\mathrm{mN/m}$.

Second, minimum concentration of 5 µM BAC was combined with 100 mM BzA (red curves), the concentration present in the commercial sanitiser used for control experiments (cf. appendix A.1). The onset of pressure change upon compression is comparable to that of the single presence of BAC. Maximum compressional modulus of $\sim 20\,\mathrm{mN/m}$ is reached at $\pi \sim 20\,\mathrm{mN/m}$, and the collapse of the monolayer is observed at a maximum surface pressure of $\pi = 25\,\mathrm{mN/m}$. Compared to the presence of single additives, the combined effect seems to be similar to that of 200 mM BzA, and more effective than 15 µM BAC. This indicates that a strong effect of destabilisation of bacterial membranes can be achieved with the combination of lower concentrations of additives, than necessary for the single components.

4.1.3. Pressure-Area Isotherms in the Presence of Ca^{2+}

In the next step, the stability of LPS Ra monolayers was measured against the effect of BzA and BAC molecules in the presence of Ca^{2+} ions, in which condition Gram-negative bacteria exhibit resistance against a wide range of cationic surfactants.[13,15] Figure 4.3 shows pressure-area ($\pi - A$) isotherms and compressibility

analysis of LPS Ra monolayers on Ca^{2+}-loaded buffer, under the influence of various concentrations of BzA (green curves), BAC (blue curves), and the combined presence of both (purple and red curves).

Influence of BzA Presented in figure 4.3 (A) are the $\pi - A$ isotherms of LPS Ra monolayers on Ca^{2+}-loaded buffer, in the absence (black), presence of 10 mM (light green), 100 mM (medium green), and 200 mM (dark green) BzA. When 10 mM BzA is added (light green curve), the pressure increase upon compression is shifted from $\sim 240\,Å^2$ to slightly larger molecular areas of $\sim 260\,Å^2$, which remains comparable to the pure subphase (black curve). The collapse pressure remains unchanged.

When the concentration of BzA is increased by a factor of 10 (100 mM, medium green curve), the onset of pressure increase occurs already at areas per molecule $> 350\,Å^2$. The overall curve is flattened in comparison to the addition of 10 mM BzA, and the collapse pressure of the LPS monolayer is reduced to $\sim 40\,mN/m$, relative to the sole buffer.

The condition of 200 mM BzA, that destabilised the LPS Ra monolayer in the absence of Ca^{2+} without further additives, is also presented on Ca^{2+}-loaded buffer (dark green curve). Here, the onset of pressure increase was comparable to the condition of 100 mM BzA, as well as the measured curve in the region of $> 230\,Å^2$. Below $\sim 230\,Å^2$, the curve was further flattened, and the collapse of the monolayer was reached at $\sim 25 - 30\,mN/m$, relative to the buffer without monolayer.

Compressional modulus κ^{-1} calculated from $\pi - A$ isotherms on Ca^{2+}-loaded buffer is presented in figure 4.3 (B), in the absence (black), presence of 10 mM (light green), 100 mM (medium green), and 200 mM (dark green) BzA. Also on Ca^{2+}- loaded buffer, LPS Ra monolayers exhibit a general reduction of κ^{-1} values with increasing concentration of BzA. Maximum values of $\kappa^{-1} \sim 140\,mN/m$, $\sim 70\,mN/m$, and $\sim 50\,mN/m$ are reached at $\sim 40\,mN/m$, $\sim 25\,mN/m$, and $\sim 20\,mN/m$ by increasing concentrations of BzA, respectively. Collapse of the LPS Ra monolayer occurs at $\sim 50\,mN/m$, $\sim 40\,mN/m$, and $\sim 25 - 30\,mN/m$, respectively. This successive reduction of compressional modulus upon increasing the concentration of BzA prevents the phase transition of LPS Ra monolayers into the liquid condensed phase. Only the condition of 10 mM BzA exhibits values of $\kappa^{-1} > 100\,mN/m$, which indicates the phase transition from liquid-expanded phase to liquid-condensed phase at $\sim 20\,mN/m$, as observed for the control con-

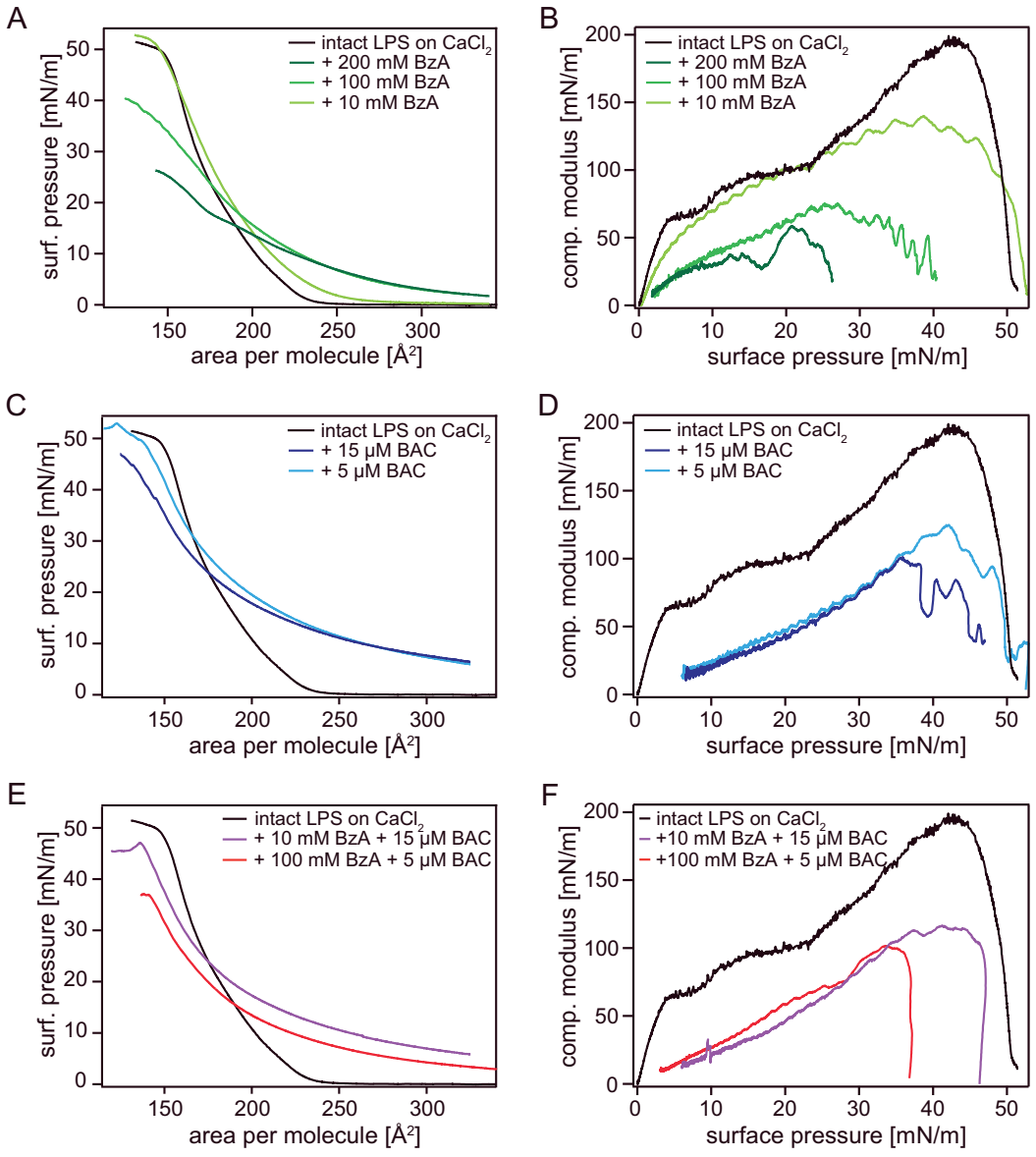

Figure 4.3.: LPS Monolayers on Ca^{2+}-loaded buffer. **(A)** Pressure-area isotherms and **(B)** compressional modulus in the presence of 10 mM (light green), 100 mM (medium green), and 200 mM (dark green) of BzA. **(C)** Pressure-area isotherms and **(D)** compressional modulus in the presence of 5 µM (light blue) and 15 µM (dark blue) of BAC. **(E)** Pressure-area isotherms and **(F)** compressional modulus in the presence of 10 mM BzA + 5 µM (light purple) and 15 µM (dark purple) of BAC, and in the presence of 100 mM BzA + 5 µM (light red) and 15 µM (dark red) of BAC.

dition. For the two higher concentrations of 100 mM and 200 mM BzA, the values of κ^{-1} remain below 100 mN/m, where no transition to liquid-condensed phase can be observed. LPS Ra monolayers remaining in liquid expanded phase exhibit an increased membrane fluidity in the presence of BzA molecules, which in fact increases the membrane permeability. Furthermore, the decrease of collapse pressure by increasing BzA concentration reflects the mechanical instability of the monolayer. This combination of effects explains the antibacterial properties of the aromatic alcohol BzA at high concentrations.

Influence of BAC Figure 4.3 (C) shows $\pi - A$ isotherms of LPS Ra monolayers on Ca^{2+}-loaded buffer, in the absence (black), presence of 5 µM (light blue), and 15 µM (dark blue) BAC.

With the addition of 5 µM BAC (light blue curve), the onset of pressure increase is already changed for large areas per molecule $>> 350\,Å^2$. This indicates a strong interaction between positively charged BAC molecules and negatively charged LPS Ra headgroups. Furthermore, the presence of 5 µM BAC flattens the $\pi - A$ curve significantly, but the collapse pressure remains unchanged. When the concentration of BAC is increased by a factor of 3 (15 µM, dark blue curve), onset and change of compressibility are not altered compared to 5 µM BAC. The collapse pressure of the LPS monolayer remained at ~ 50 mN/m.

Compressional modulus κ^{-1} calculated from $\pi - A$ isotherms on Ca^{2+}-loaded buffer is presented in figure 4.3 (D), in the absence (black), presence of 5 µM (light blue), and 15 µM (dark blue) BAC. On Ca^{2+}- loaded buffer, LPS Ra monolayers exhibit a significant reduction of κ^{-1} values in the presence of BAC. Maximum values of $\kappa^{-1} \sim 120$ mN/m and ~ 100 mN/m are reached at ~ 40 mN/m and ~ 35 mN/m for increasing concentrations of BAC. The collapse of the monolayer occurs at a higher surface pressure of ~ 50 mN/m, compared to the corresponding values in the absence of Ca^{2+} ions.

As observed on Ca^{2+}-free conditions, the similar behaviour of compressibility between the different concentrations of BAC indicate that the range of interactions between BAC and LPS Ra headgroups reaches an equilibrium state, independent from concentration.

Synergistic Effect of BzA and BAC Also in the presence of Ca^{2+}, the influence of the combined addition of BzA and BAC was investigated. $\pi - A$ isotherms

are presented in figure 4.3 (E) with corresponding compressional modulus (F). First, the maximum concentration of 15 µM BAC was combined with the minimum addition of 10 mM BzA (purple curves). As can be seen by both isotherms and compressional modulus, the addition of 10 mM BzA did not cause major changes to the behaviour compared to the pure presence of 5 and 15 µM BAC. The onset of pressure change upon compression is comparable to that of the single presence of BAC. At molecular areas of $\sim 40 - 45$ mN/m, maximum compressional modulus of ~ 100 mN/m is reached, whereafter the monolayer immediately collapses at $\pi = 45$ mN/m.

Second, low concentration of 5 µM BAC was combined with 100 mM BzA (red curves). The onset of pressure change upon compression is comparable to that of the single presence of BAC. Maximum compressional modulus of ~ 100 mN/m is reached at $\pi \sim 35$ mN/m, whereafter the immediate collapse of the monolayer is observed. Compared to the presence of single additives, the combined effect seems to be similar to that of 15 µM BAC, with a shift of π values towards lower molecular areas, and the collapse behaviour of the monolayer to an immediate effect at lower value.

4.1.4. Discussion

In this section, changes in stability and compressibility of LPS Ra monolayers caused by the addition of surface active molecules were presented. As indicated by CFU experiments in appendix A.1, the effect of additives is more pronounced in the absence of divalent cations. For the single addition of BzA, the collapse pressure was significantly reduced starting from 10 mM BzA, while on Ca^{2+} containing subphase a similar effect only occurred at a 10 times higher concentration. Furthermore, the condition that destabilised the bacterial membrane in the absence of Ca^{2+} did not achieve the same effect in the presence of Ca^{2+} ions.

The successive reduction of compressional modulus $\kappa_{\mathrm{max}}^{-1}$ upon increasing the concentration of BzA indicated a change in phase transition behaviour of LPS Ra monolayers. In the absence of Ca^{2+} ions, all concentrations of BzA caused $\kappa_{\mathrm{max}}^{-1}$ to remain below 100 mN/m, showing the prevention of phase transition from liquid-expanded into liquid-condensed phase. Under Ca^{2+}-loaded conditions, only the addition of 10 mM BzA provided values of $\kappa_{\mathrm{max}}^{-1} > 100$ mN/m, which indicates a phase transition from liquid-expanded to liquid-condensed phase. For higher con-

Table 4.1.: Collapse pressure π_{max} [mN/m] obtained from $\pi - A$ isotherms on Ca^{2+}-free and Ca^{2+}-loaded subphase, in the presence of different concentrations of BzA, BAC, and combination of both additives.

	Ca^{2+}-free			**Ca^{2+}-loaded**		
BzA \ BAC	0 µM	5 µM	15 µM	0 µM	5 µM	15 µM
0 mM	50	40	30	50	50	50
10 mM	40		35	50		45
100 mM	33	25		40	35	
200 mM	22			27		

centrations of BzA, values of κ_{max}^{-1} remain below 100 mN/m, where no transition to liquid-condensed phase can be observed. LPS Ra monolayers remaining in liquid expanded phase exhibit an increased membrane fluidity, which in fact increases the membrane permeability. Furthermore, the decrease of collapse pressure by increasing BzA concentration reflects the mechanical instability of the monolayer. The combination of those effects explains the antibacterial properties of the aromatic alcohol BzA at high concentrations.

In the presence of single additive BAC, a concentration-dependent reduction of collapse pressure was observed on Ca^{2+}-free subphase, while under Ca^{2+}-loaded conditions the collapse pressure remained unchanged. For the change of maximum κ^{-1} indicating the phase transition behaviour of LPS Ra monolayers, BAC caused

Table 4.2.: Maximum compressional modulus κ_{max}^{-1} [mN/m] obtained from $\pi - A$ isotherms on Ca^{2+}-free and Ca^{2+}-loaded subphase, in the presence of different concentrations of BzA, BAC, and combination of both additives.

	Ca^{2+}-free			**Ca^{2+}-loaded**		
BzA \ BAC	0 µM	5 µM	15 µM	0 µM	5 µM	15 µM
0 mM	120	30	30	200	120	100
10 mM	70		30	140		100
100 mM	50	20		70	100	
200 mM	20			50		

an immediate decrease below 100 mN/m on Ca^{2+}-free condition, independent from concentration. Therefore, by the presence of cationic surfactant, LPS monolayers were prevented from transition into liquid-condensed phase, indicating increased membrane fluidity causing an increase in membrane permeability. Furthermore, the mean molecular area at $\pi = 20\,\mathrm{mN/m}$ increased by $\Delta A \approx 90\,\text{Å}^2$ in the presence of BAC, which suggests the incorporation of the hydrocarbon chains of BAC into the LPS membrane.[11] In the presence of Ca^{2+}, however, the reduction of $\kappa_{\mathrm{max}}^{-1}$ was less pronounced, and $\kappa_{\mathrm{max}}^{-1}$ remained above 100 mN/m for all concentrations investigated in this section. Furthermore, at $\pi = 15\,\mathrm{mN/m}$, the increase in the mean molecular area caused by BAC, $\Delta A \approx 30\,\text{Å}^2$, was less than one half compared to the effect on Ca^{2+}-free subphase.

The combined application of 100 mM BzA and 5 µM BAC caused further decrease of both collapse pressure and $\kappa_{\mathrm{max}}^{-1}$ on Ca^{2+}-free conditions, while the addition of 10 mM BzA did not alter the impact of 15 µM BAC significantly. On Ca^{2+}-loaded subphase, the collapse pressure was decreased by the addition of both 10 mM and 100 mM BzA to previously discussed concentrations of BAC. Maximum compressional modulus, however, remained unchanged at values of $\sim 100\,\mathrm{mN/m}$, indicating a potential of transition into liquid-condensed phase.

The investigation of monolayer stability and phase transition behaviour provides insight into the combined effect of the surface active compounds BzA and BAC. As presented in this paragraph, the combined influence of non-lethal concentrations of both additives seems to be as effective as the impact of lethal concentrations of aromatic alcohol, and will be further investigated in the next sections. Following to the onset of effect for single additives and the combined condition from film stability and compressibility analysis, the intermediate concentration of 100 mM BzA and the minimum concentration of 5 µM BAC were chosen for further studies, focussing on fine structures as well as the reconstruction of ion distribution profiles across LPS Ra monolayers using synchrotron radiation.

4.2. Influence of BzA on the Structure of Bacterial Outer Membranes

In the following section, the impact of aromatic alcohol BzA on the structure of LPS Ra monolayers is investigated in the absence and presence of Ca^{2+} ions. Experiments considering 100 mM BzA were measured at 10 keV and performed at ESRF, Grenoble, France. On Ca^{2+}-free buffer, surface pressure was held constant at $\pi = 20\,\mathrm{mN/m}$, corresponding to a mean molecular area of A $\approx 205\,\text{Å}^2$ in the absence of additives. In the presence of 100 mM BzA, $\pi = 20\,\mathrm{mN/m}$ was set relative to the surface pressure of the blank subphase ($\pi_{\mathrm{BzA}} \approx 15\,\mathrm{mN/m}$). Isotherm data including this offset level are presented in appendix A.2 figure A.3 (A) and (D), confirming that the area per molecule near the collapse converges with that of the intact LPS Ra monolayer.

Since the LPS Ra monolayer is compacted in the presence of Ca^{2+} ions,[5,8] XRR measurements on Ca^{2+}-loaded condition were performed at $\pi = 15\,\mathrm{mN/m}$, corresponding to a mean molecular area of A $\approx 203\,\text{Å}^2$ in the absence of additives. The surface pressure of the blank subphase containing the additive remained unchanged compared to the Ca^{2+}-free condition.

4.2.1. Structural Changes on Ca^{2+}-free Subphase

In the first step, the impact of adding 100 mM BzA on the structure of LPS Ra monolayers was studied in the absence of divalent cations. XRR data (symbols) and the corresponding best fit curves (solid lines) are presented in figure 4.4 (A) in the absence (black) and presence (green) of 100 mM BzA. Electron density profiles reconstructed from the fitting results are shown in panel 4.4 (B). For fitting, two layers were applied in the slab model, representing the hydrocarbon chains as the first layer, and the carbohydrate headgroups as the second. For starting values, results from previously published XRR measurements were used.[8]

Resulting fitting parameters from the best matching fit curves are summarised in table 4.3. While the thickness of both chains and headgroups remained unchanged by the presence of 100 mM BzA, only the roughness of the interface between hydrocarbon chains and carbohydrate head groups was elevated from $\sigma = 3.9\,\text{Å}$ to 5.6 Å by factor of 1.4. This suggests that BzA molecules adsorb to the interface between hydrocarbon chains and carbohydrate head groups and roughen this in-

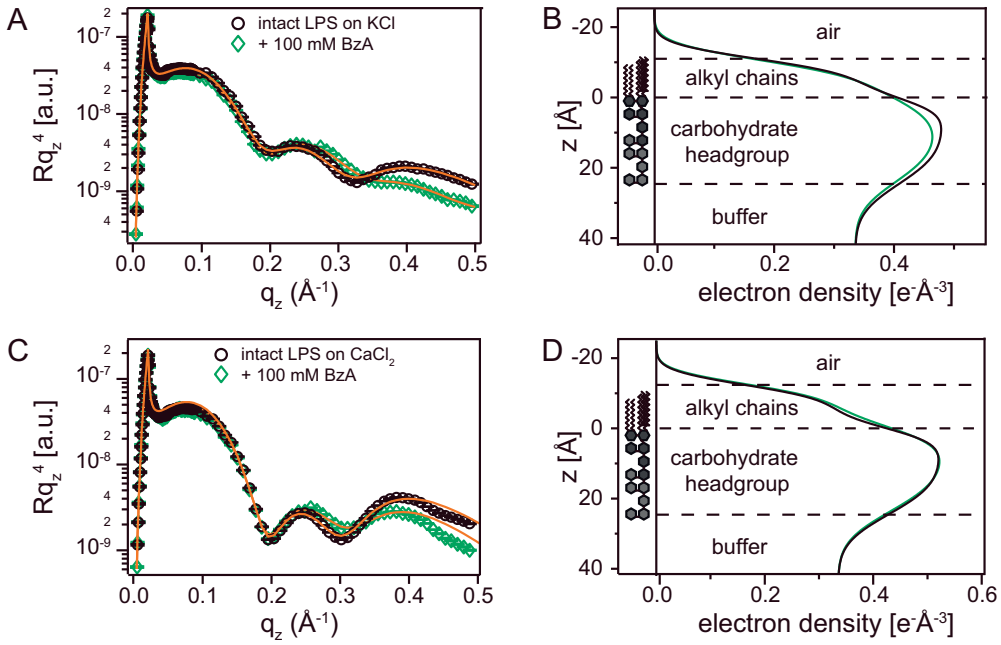

Figure 4.4.: Influence of BzA on LPS Ra monolayers in the absence and presence of Ca^{2+} ions. **(A)** XRR data and **(B)** reconstructed electron density profiles of LPS Ra monolayers in the absence (black) and presence (green) of 100 mM BzA, measured on Ca^{2+}-free subphase. **(C)** XRR data and **(D)** reconstructed electron density profiles in the absence (black) and presence (green) of 100 mM BzA, measured on Ca^{2+}-loaded subphase.

Table 4.3.: Structural parameters on Ca^{2+}-free condition in the presence of 100 mM BzA from fitting two layers in the slab model. Thickness d, electron density ρ, and roughness σ of alkyl chains and saccharide head groups of LPS Ra monolayers.

Ca^{2+}-free				**+ 100 mM BzA**		
	d [Å]	ρ [e^-Å^{-3}]	σ [Å]	d [Å]	ρ [e^-Å^{-3}]	σ [Å]
alkyl chains	10.6	0.326	3.4	10.8	0.323	3.9
head group	24.0	0.483	3.9	24.3	0.472	5.6
bulk	∞	0.334	6.8	∞	0.334	6.5

terface, while the roughness of the other interfaces showed no remarkable changes. The electron density was slightly reduced at the headgroups in the presence of BzA. These minor changes in the monolayer structure seem to explain the additional data presented in appendix A.1 figure A.2 (A), showing that 100 mM BzA caused a decrease in CFU/mL in Ca^{2+}-free buffer, but is not sufficient to kill all bacteria.

4.2.2. Structural Changes on Ca^{2+}-loaded Subphase

In the next step, XRR experiments as described in the previous section were repeated in the presence of Ca^{2+} ions. XRR data (symbols) and the corresponding best fit curves (solid lines) are presented in figure 4.4 (C) in the absence (black) and presence (green) of 100 mM BzA. Electron density profiles reconstructed from the fitting results are shown in panel 4.4 (D). In the presence of Ca^{2+}, the difference in the global shape of XRR data caused by 100 mM BzA was minor, and the electron density profiles reconstructed from the XRR data are almost identical. Results from the fitting are summarised in table 4.4, and no roughening of the head–tail interface was caused (constant $\sigma = 3.7$ Å). This lack of effect is different from the results on Ca^{2+}-free buffer, and seems to coincide with the fact that the CFU/mL level in the presence of BzA was about 2 orders of magnitude higher in Ca^{2+}-loaded buffer appendix A.1 figure A.2 (A) compared to the Ca^{2+}-free condition. This indicates that 100 mM BzA alone is non-lethal for *Salmonella enterica* (serovar Minnesota) rough mutant R60.

Table 4.4.: Structural parameters on Ca^{2+}-loaded condition in the presence of 100 mM BzA from fitting two layers in the slab model. Thickness d, electron density ρ, and roughness σ of alkyl chains and saccharide head groups of LPS Ra monolayers.

Ca^{2+}-loaded				**+ 100 mM BzA**		
	d [Å]	ρ [e^-Å^{-3}]	σ [Å]	d [Å]	ρ [e^-Å^{-3}]	σ [Å]
alkyl chains	12.4	0.319	3.3	12.7	0.348	3.7
head group	24.6	0.525	3.7	23.0	0.525	3.7
bulk	∞	0.334	6.7	∞	0.334	6.8

4.3. Influence of BAC on the Structure of Bacterial Outer Membranes

In the following section, results from analysis of the impact of cationic surfactant BAC on the structure of LPS Ra monolayers is presented in the absence and presence of Ca^{2+} ions. In the presence of 5 µM BAC, XRR was measured at 8 keV. Surface pressure of $\pi = 20\,\mathrm{mN/m}$ on Ca^{2+}-free buffer was set relative to the surface pressure of the blank subphase containing the additive ($\pi_{\mathrm{BAC}} \approx 7\,\mathrm{mN/m}$). The data including this offset level are presented in appendix A.2 figure A.3, confirming that the area per molecule near the collapse converges with that of the intact LPS Ra monolayer. In the presence of Ca^{2+} ions, XRR measurements were performed at $\pi = 15\,\mathrm{mN/m}$. The surface pressure of the blank subphase containing the additive remained unchanged compared to the Ca^{2+}-free condition.

4.3.1. Structural Changes on Ca^{2+}-free Subphase

First, structural changes of LPS Ra monolayers by the addition of 5 µM BAC were probed in the absence of Ca^{2+} ions. XRR data (symbols) and the corresponding best fit curves (solid lines) are presented in figure 4.5 (A) in the absence (black) and presence (blue) of 5 µM BAC, and e^- density profiles reconstructed from the fitting results are shown in figure 4.5 (B). By the addition of BAC, periodic oscillations are lost in the XRR data, which shows a distinct difference to the intact LPS Ra monolayer. The reconstructed electron density profile (panel B) clearly indicates that the structural integrity of the LPS Ra monolayer, the stratified membrane structure with conformal roughness, was significantly disturbed by BAC alone.

Results from fitting two layers in the slab model are summarised in table 4.5. While the layer thickness of both chains and headgroups remained mostly unchanged, the roughness of the interfaces was altered by the presence of 5 µM BAC. While the interfacial roughness of air-chain and chain-headgroup was elevated from 3.4 Å to 5.0 Å and from 3.9 Å to 7.3 Å (factor 1.5 – 1.9), the roughness at the headgroup-bulk interface was reduced from 6.8 Å to 4.3 Å by factor of 1.6. This disturbance of the integrity of the stratified membrane structure by BAC alone seems consistent with the fact that no bacteria survived after 5 min incubation only with BAC appendix A.1 figure A.2 (B). The electron density at the headgroups was reduced from $0.483\,e^-/Å^3$ to $0.356\,e^-/Å^3$ by factor of 1.4 in the

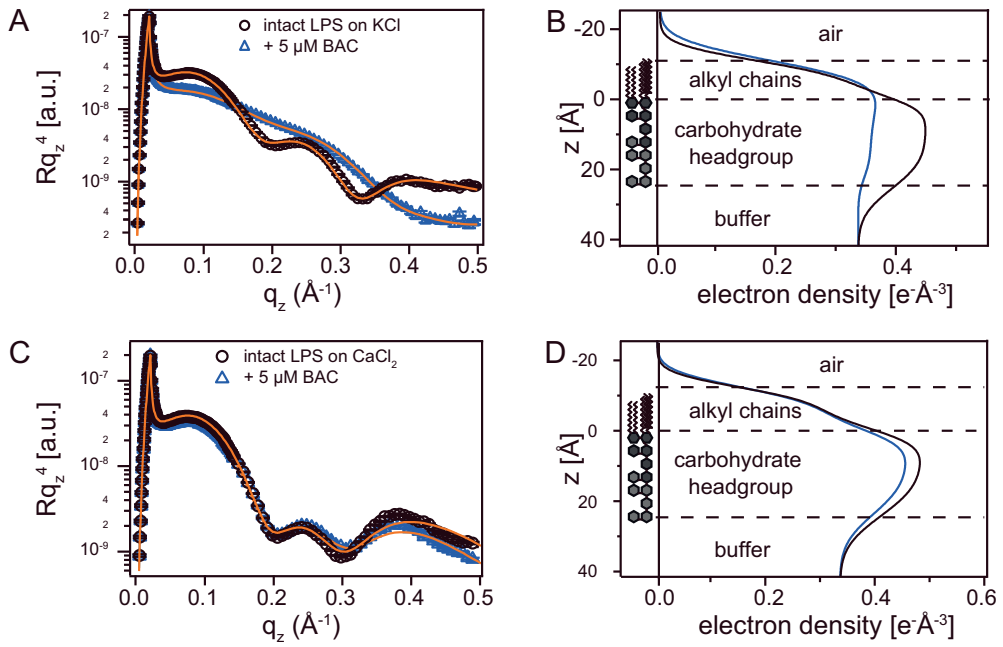

Figure 4.5.: Influence of BAC on LPS Ra monolayers in the absence and presence of Ca^{2+} ions. **(A)** XRR data and **(B)** reconstructed electron density profiles of LPS Ra monolayers in the absence (black) and presence (blue) of 5 µM BAC, measured on Ca^{2+}-free subphase. **(C)** XRR data and **(D)** reconstructed electron density profiles in the absence (black) and presence (blue) of 5 µM BAC, measured on Ca^{2+}-loaded subphase.

Table 4.5.: Structural parameters on Ca^{2+}-free condition in the presence of 5 µM BAC from fitting two layers in the slab model. Thickness d, electron density ρ, and roughness σ of alkyl chains and saccharide head groups of LPS Ra monolayers.

Ca^{2+}-free				**+ 5 µM BAC**		
	d [Å]	ρ [e^-Å^{-3}]	σ [Å]	d [Å]	ρ [e^-Å^{-3}]	σ [Å]
alkyl chains	10.6	0.326	3.4	11.9	0.377	5.0
head group	24.0	0.483	3.9	21.6	0.356	7.3
bulk	∞	0.334	6.8	∞	0.334	4.3

presence of BAC. This decrease indicates a loss of LPS Ra molecules from the interface, and combined with the increased roughness leads to the destabilisation of the monolayer.

4.3.2. Structural Changes on Ca^{2+}-loaded Subphase

Similar to the experiments presented in the previous section, the structure of LPS Ra monolayers was also characterised in the presence of Ca^{2+} ions and 5 µM BAC. XRR data (symbols) and the corresponding best fit curves (solid lines) are presented in figure 4.5 (C) in the absence (black) and presence (blue) of 5 µM BAC. Electron density profiles reconstructed from the fitting results are shown in panel 4.5 (D). The global XRR curve in the presence of BAC resembles that of intact LPS Ra, but the main difference can be seen in the head group region of the e^- density curve.

Results from fitting two layers in the slab model are summarised in table 4.6. While the thickness of both chains and headgroups remained unchanged by the presence of 5 µM BAC, roughness of the interface between hydrocarbon chains and carbohydrate head groups was slightly elevated from $\sigma = 3.7$ Å to 4.2 Å. The electron density of the headgroups was slightly reduced from 0.525 to 0.460 $e^-/Å^3$. These minor structural changes suggest the decrease in the packing density of negatively charged saccharide head groups by the binding of cationic BAC.

The maintenance of stratified membrane structures with conformal roughness was confirmed by the reconstructed electron density profiles (figure 4.5 (D)). The

Table 4.6.: Structural parameters on Ca^{2+}-loaded condition in the presence of 5 µM BAC from fitting two layers in the slab model. Thickness d, electron density ρ, and roughness σ of alkyl chains and saccharide head groups of LPS Ra monolayers.

Ca^{2+}-loaded				**+ 5 µM BAC**		
	d [Å]	ρ [e^-Å^{-3}]	σ [Å]	d [Å]	ρ [e^-Å^{-3}]	σ [Å]
alkyl chains	12.4	0.319	3.3	12.1	0.292	3.7
head group	24.6	0.525	3.7	23.7	0.460	4.2
bulk	∞	0.334	6.7	∞	0.334	7.2

higher stability of the LPS Ra monolayer observed on Ca^{2+}-loaded subphase seems consistent with the high CFU/mL level observed in bacterial killing assays at a concentration of 5 µM BAC (cf. appendix A.1 figure A.2 (B)). The fact that 5 µM BAC alone is not able to disturb the stratified LPS Ra membrane structure in the presence of Ca^{2+} coincides with the resistance of bacteria against QAC.[13,15]

4.4. Synergistic Effect of BzA and BAC

The next question addressed in this chapter is whether the combination of aromatic alcohol (BzA) and cationic surfactant (BAC) promotes the disturbance of bacterial outer membranes. In the presence of 100 mM BzA + 5 µM BAC, XRR was measured at 8 keV. Surface pressure of $\pi = 20$ mN/m on Ca^{2+}-free buffer was set relative to the surface pressure of the blank subphase containing the additive ($\pi_{BAC+BzA} \approx 20$ mN/m). The data including this offset level are presented in appendix A.2 figure A.3, confirming that the area per molecule near the collapse converges with that of the intact LPS Ra monolayer. In the presence of Ca^{2+} ions, XRR measurements were performed at $\pi = 15$ mN/m. The surface pressure of the blank subphase containing the additive remained unchanged compared to the Ca^{2+}-free condition.

4.4.1. Structural Changes on Ca^{2+}-free Subphase

First, the the impact of the combination of 100 mM BzA and 5 µM BAC on the structure of LPS Ra was investigated in the absence of Ca^{2+} ions, by performance of of XRR experiments. XRR data (symbols) and the corresponding best fit curves (solid lines) are presented in figure 4.6 (A) in the absence (black) and presence (red) of 100 mM BzA + 5 µM BAC, and e^- density profiles reconstructed from the fitting results are shown in figure 4.6 (B). As by the addition of BAC alone (fig. 4.5 (A)), periodic oscillations are lost in the XRR data, implying the loss of stratified membrane structures. Also the reconstructed electron density profile clearly indicates that the structural integrity of the LPS Ra monolayer was significantly disturbed. This finding seems reasonable, since no bacterial survival was observed in Ca^{2+}-free buffer at a concentration of ≥ 1 µM BAC, independent from additional BzA concentration appendix A.1 figure A.2 (B) and (C).

A summary of results from fitting two layers in the slab model is presented

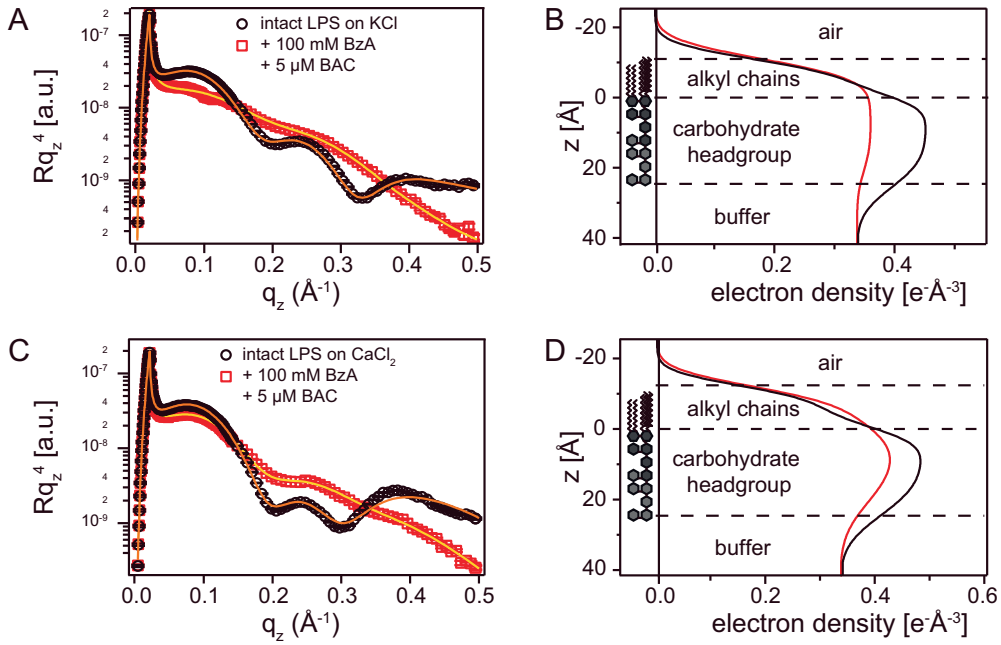

Figure 4.6.: Synergistic influence of BzA and BAC on LPS Ra monolayers in the absence and presence of Ca^{2+} ions. **(A)** XRR data and **(B)** reconstructed electron density profiles of LPS Ra monolayers in the absence (black) and presence (red) of 100 mM BzA + 5 µM BAC, measured on Ca^{2+}-free subphase. **(C)** XRR data and **(D)** reconstructed electron density profiles in the absence (black) and presence (red) of 100 mM BzA + 5 µM BAC, measured on Ca^{2+}-loaded subphase.

Table 4.7.: Structural parameters on Ca^{2+}-free condition in the presence of 100 mM BzA + 5 µM BAC from fitting two layers in the slab model. Thickness d, electron density ρ, and roughness σ of alkyl chains and saccharide head groups of LPS Ra monolayers.

Ca^{2+}-free				**+ 100 mM BzA + 5 µM BAC**		
	d [Å]	ρ [e^-Å^{-3}]	σ [Å]	d [Å]	ρ [e^-Å^{-3}]	σ [Å]
alkyl chains	10.6	0.326	3.4	11.7	0.356	4.6
head group	24.0	0.483	3.9	20.6	0.360	4.9
bulk	∞	0.334	6.8	∞	0.334	5.7

in table 4.7. While the layer thickness of both chains and headgroups remained mostly unchanged, the combined presence of BzA and BAC caused an increase in interfacial roughness between chains and headgroups by factor of 1.3 from 3.9 Å to 4.9 Å. Furthermore, the electron density at the headgroups was reduced by factor of 1.3 from 0.483 $e^-/Å^3$ to 0.360 $e^-/Å^3$. As discussed for the results on the single addition of BAC in section 4.3.1, this effect can be interpreted as loss of LPS from the interface and destabilisation of the membrane structure.

4.4.2. Structural Changes on Ca^{2+}-loaded Subphase

In the next step, structural changes of LPS Ra monolayers were analysed in the presence of Ca^{2+} ions and a combination of 100 mM BzA and 5 µM BAC. XRR data (symbols) and the corresponding best fit curves (solid lines) are presented in figure 4.6 (C) in the absence (black) and presence (red) of 100 mM BzA + 5 µM BAC. Electron density profiles reconstructed from the fitting results are shown in figure 4.6 (D). Remarkably, the global shape of the XRR curve (panel C) is clearly different from the curves in the presence of BzA alone (fig. 4.4 (C)) or BAC alone (fig. 4.5 (C)).

Results from fitting two layers in the slab model are summarised in table 4.8. Thickness of the alkyl chains was slightly reduced from 12.4 Å to 10.2 Å in the combined presence of additives (factor 1.2). Most remarkably, the roughness of the interface between hydrocarbon chains and carbohydrate head groups was significantly elevated by factor of 1.7 from σ = 3.7 Å to 6.2 Å which is an additional

Table 4.8.: Structural parameters on Ca^{2+}-loaded condition in the presence of 100 mM BzA + 5 µM BAC from fitting two layers in the slab model. Thickness d, electron density ρ, and roughness σ of alkyl chains and saccharide head groups of LPS Ra monolayers.

Ca^{2+}-loaded				**+ 100 mM BzA + 5 µM BAC**		
	d [Å]	ρ [$e^-Å^{-3}$]	σ [Å]	d [Å]	ρ [$e^-Å^{-3}$]	σ [Å]
alkyl chains	12.4	0.319	3.3	10.2	0.313	4.0
head group	24.6	0.525	3.7	22.9	0.437	6.2
bulk	∞	0.334	6.7	∞	0.334	7.9

increase by factor of 1.5 compared to the effect of 5 µM BAC alone (σ = 4.2 Å table 4.6). The electron density of the headgroups was reduced from 0.525 $e^-/Å^3$ to 0.437 $e^-/Å^3$ (factor 1.2).

The obtained results clearly indicate the synergistic function of BzA and BAC. As a reference, the XRR measurement of 50 mM BzA + 5 µM BAC is presented in appendix A.3 figure A.3 (E), where the integrity of the stratified layers is clearly indicated by the periodic oscillations of the XRR data. While the addition of 50 mM BzA to 5 µM BAC leaves the layered structure in the presence of Ca^{2+} mostly intact, the disturbance of the stratified membrane structures by 100 mM BzA enables the incorporation of BAC.

4.5. Influence of Additives on the Ion Concentration Profiles near the Interface

As a LPS Ra molecule contains charged saccharide units (cf. fig. 3.1), the disturbance of structural integrity of membranes should result in the change in ion distribution near the membrane surface.[7,8] To determine the ion concentration profiles of K^+ and Ca^{2+} within the LPS Ra monolayers, each XRR experiment was followed by the recording of GIXF signals at incident angles below (surface information) and above (bulk information) the critical angle of total external reflection (cf. chapter 2.1, eq. 2.13). To highlight the protective function of divalent Ca^{2+} ions, the density profiles of K^+ and Ca^{2+} will be compared on Ca^{2+}-free and Ca^{2+}-loaded subphase.

4.5.1. Concentration Profile of K^+

Figure 4.7 (A) shows the normalised X-ray fluorescence signals from the K–K_α line measured on Ca^{2+}-free buffer in the absence of additives (black), in the presence of 100 mM BzA (green), 5 µM BAC (blue), and 100 mM BzA + 5 µM BAC (red), plotted as a function of q_z. Signals collected below the critical angle ($q_z \leq q_c$ = 0.022 $Å^{-1}$) arise from K^+ near the interface, while the data from the angle beyond the critical angle $q_z > q_c$ represent the K^+ in the bulk subphase. Experimental data was fitted using equation 2.41, section 2.2, where the illumination profile was calculated using the results from XRR analysis (cf. sec. 4.2 – 4.4, tables 4.3 – 4.7).

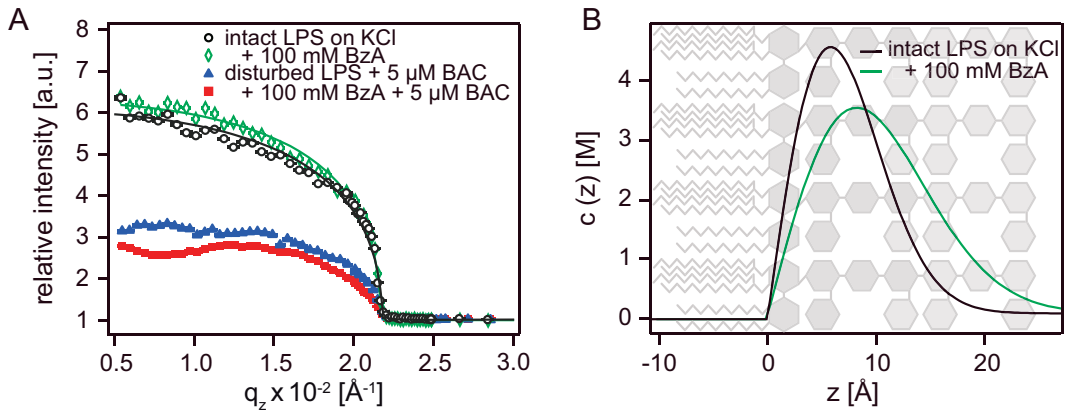

Figure 4.7.: Influence of additives on ion concentration profiles in the absence of Ca^{2+} ions. (A) Normalised X-ray fluorescence signals from the K–K_α line measured in the absence of additives (black), in the presence of 100 mM BzA (green), 5 µM BAC (blue), and 100 mM BzA + 5 µM BAC (red). **(B)** Reconstructed ion concentration profiles of K^+ in the absence (black) and presence (green) of 100 mM BzA. Signals from disturbed layers could not be fitted for calculation of ion density profiles.

For all samples, counts at $q_z \leq q_c$ exhibit higher values than in the bulk, which suggests the accumulation of K^+ near the interface. In the presence of 100 mM BzA (green), no major changes in the normalised fluorescence signal were observed, compared to the measurement in absence of additives (black). In the presence of 5 µM BAC (blue), the fluorescence signal near the interface was significantly reduced. This reduction was further increased by the combined addition of 5 µM BAC + 100 mM BzA (red). For the absence of additives (black) and presence of 100 mM BzA, data sets were fitted using equation 2.41, while in the presence of 5 µM BAC and 100 mM BzA + 5 µM BAC, no reasonable fitting results could be achieved. This coincides with the observation from XRR data, suggesting the strong disturbance of the layered membrane structures (cf. sections 4.3 – 4.4, figures 4.5 – 4.6).

Ion density profiles of K^+ ions corresponding to the best fit results and calculated by equation 2.42 are presented in figure 4.7 (B). Bulk concentration was considered constant at 100 mM K^+, and thicknesses of layers were obtained from XRR analysis (cf. section 4.2, table 4.3). For the intact LPS Ra monolayer in absence of additives (black), the concentration of K^+ ions exhibits a maximum value of $c_{\max(K)} = 4.6$ M

at $z_{\max(K)} = 6$ Å from the chain/headgroup interface. This concentration is 46 times higher than the bulk level (100 mM KCl), and the peak position corresponds to the position of inner core saccharides consisting of two phosphorylated glucosamine units and two 2-keto-3-deoxyoctonoic acid units. Lateral density c_L of K^+ ions was calculated by integration of the concentration along the z-axis, to $c_{L(K)} = 2.6 \times 10^{14}$ ions/cm^2. With the area per LPS Ra molecule at $\pi = 20$ mN/m, A ≈ 210 Å^2 (π – A isotherms, sec. 4.1.2, fig. 4.2 (A)), the number of K^+ ions associated with one LPS Ra molecule was determined to be N = 5.5. The obtained value is in agreement with previously published data,[8] and seems reasonable from the net charge of 6 e^- per core saccharide.[5]

For the intact LPS Ra monolayer in the presence of 100 mM BzA (green), the concentration of K^+ ions exhibits a maximum value of $c_{\max(K)} = 3.5$ M at $z_{\max(K)} = 8$ Å from the chain/headgroup interface. This minor broadening of the K^+ peak can be attributed to the roughening of the interface between hydrocarbon chains and head groups suggested by XRR (sec. 4.2, fig. 4.4 (A), tab. 4.3). The apparent shift in the peak position (Δz = 2 Å) is within the spatial resolution[9] of ± 3 Å. The calculated lateral ion density ($c_{L(K)} = 2.9 \times 10^{14}$ ions/cm^2) and the number of associating K^+ ions (N = 5.7) suggest that the charge neutrality and thus the electrostatic barrier were not disturbed by 100 mM BzA.

For the LPS Ra monolayer in the presence of 5 µM BAC and 100 mM BzA + 5 µM BAC, no reasonable fitting results of fluorescence data and therefore no reconstruction of the ion density profile could be achieved, due to the strong disturbance of the layered membrane structures.

4.5.2. Concentration Profile of Ca^{2+}

In the following section, Ca^{2+} ion concentration profiles near the LPS Ra monolayers are reconstructed in the presence of Ca^{2+}-loaded buffer containing 100 mM BzA, 5 µM BAC, or the combination of both. Figure 4.8 (A) shows the normalised X-ray fluorescence signals from the Ca–K_α line measured on Ca^{2+}-loaded buffer in the absence of additives (black), in the presence of 100 mM BzA (green), 5 µM BAC (blue), and 100 mM BzA + 5 µM BAC (red), plotted as a function of q_z. For fitting of the experimental data, the illumination profiles were calculated using the results from XRR analysis (cf. sections 4.2 – 4.4, tables 4.4 – 4.8).

For all samples, counts at $q_z \leq q_c$ exhibit higher values than in the bulk, which

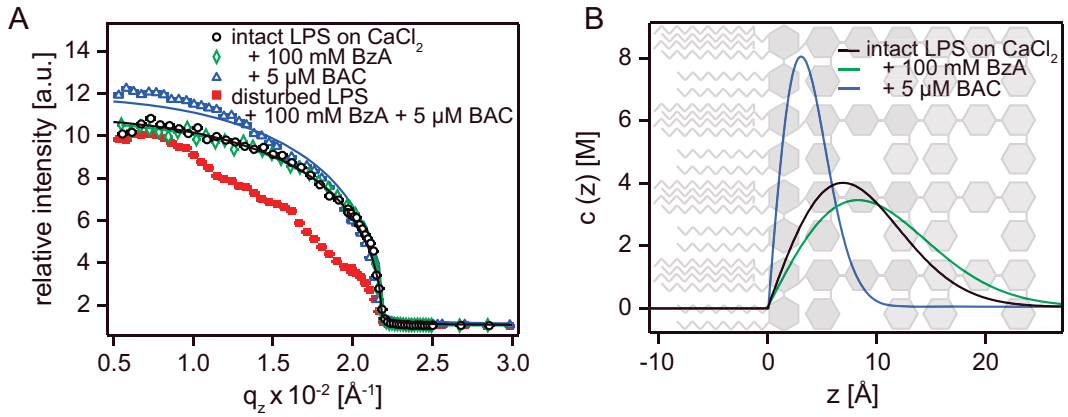

Figure 4.8.: Influence of additives on ion concentration profiles in the presence of Ca^{2+} ions. (A) Normalised X-ray fluorescence signals from the Ca–K_α line measured in the absence of additives (black), in the presence of 100 mM BzA (green), 5 µM BAC (blue), and 100 mM BzA + 5 µM BAC (red). **(B)** Reconstructed ion concentration profiles of Ca^{2+} in the absence of additives (black) and in the presence of of 100 mM BzA (green) and 5 µM BAC (blue). Signals from the disturbed layer could not be fitted for calculation of the ion density profile.

suggests the condensation of Ca^{2+} near the interface. In the presence of 100 mM BzA (green), no changes in the normalised fluorescence signal were observed, compared to the measurement in absence of additives (black). In the presence of 5 µM BAC (blue), the fluorescence signal near the interface showed minor enhancement compared to the absence of additives. The addition of the combination of 5 µM BAC + 100 mM BzA (red) resulted in a clear reduction of fluorescence signal near the interface, and the characteristic shape of the Ca^{2+} ion density profile was strongly altered.

For the absence of additives, presence of 100 mM BzA, and presence of 5 µM BAC, data sets were fitted using equation 2.41. In the presence of 100 mM BzA + 5 µM BAC, no reasonable fitting results could be achieved. This coincides with the observation from XRR data, suggesting that even in the presence of divalent Ca^{2+} the layered membrane structures is strongly disturbed by the combined presence of BzA and BAC (cf. section 4.4, fig. 4.6).

Ion density profiles of Ca^{2+} ions corresponding to the best fit results and calculated by equation 2.42 are presented in figure 4.8 (B). Bulk concentration was considered constant at 50 mM Ca^{2+}, and thickness of layers was obtained from XRR analysis (sections 4.2 – 4.3, tables 4.4 – 4.6). For the intact LPS Ra monolayer in absence of additives (black), the concentration of Ca^{2+} ions exhibits a

maximum value of $c_{\max(Ca)} = 4.0\,M$ at $z_{\max(Ca)} = 7\,Å$ from the chain/headgroup interface, almost identical to $z_{\max(K)}$ on Ca^{2+}-free subphase. Lateral density c_L of Ca^{2+} ions was calculated by integration of the concentration along the z-axis, to $c_{L(Ca)} = 2.5 \times 10^{14}$ ions/cm^2. With the area per LPS Ra molecule at surface pressure $\pi = 15\,mN/m$, A $\approx 190\,Å^2$ (cf, $\pi - A$ isotherms, sec. 4.1.3, fig. 4.3 (A)), the number of Ca^{2+} ions associated with one LPS Ra molecule was determined to be N = 4.7. This value is in agreement with previously published data.[7,8] The accumulation of $Q_{Ca2+} \sim +9\,e$ charges per LPS Ra molecule carrying $Q_{LPS} \sim -6\,e$ can be explained by the gain in cavitational energy outweighing the low electrostatic energy penalty, as interpreted within the framework of dielectric continuum theory.[157–159]

For the intact LPS Ra monolayer in the presence of 100 mM BzA (green), the concentration of Ca^{2+} ions exhibits a maximum value of $c_{\max(Ca)} = 3.4\,M$ at $z_{\max(Ca)} = 8\,Å$ from the chain/headgroup interface, almost identical to the results in the absence of additives. The calculated lateral ion density ($c_{L(Ca)} = 2.4 \times 10^{14}$ ions/cm^2) and the number of associating Ca^{2+} ions (N = 4.8) suggest that the addition of 100 mM BzA did not alter the electrostatic barrier compared to the control measurement. This analysis shows that the presence of Ca^{2+} not only preserves the structures (sec. 4.2, fig. 4.4) but also the ion density profiles near the interface from the influence of 100 mM BzA.

For the intact LPS Ra monolayer in the presence of 5 µM BAC (blue), the distribution of Ca^{2+} exhibited a distinct difference from the results in the absence of additives, as well as the analysis of K^+ measured on Ca^{2+}-free subphase (cf. sec. 4.5.1, fig. 4.7 (B)). The reconstruction of the ion concentration profile resulted in a maximum concentration of Ca^{2+} ions of $c_{\max(Ca)} = 8.0\,M$ at $z_{\max(Ca)} = 3\,Å$ from the chain/headgroup interface. Still, the lateral density of Ca^{2+} ions remained at $c_{L(Ca)} = 2.4 \times 10^{14}$ ions/cm^2, as well as the number of Ca^{2+} ions associated with one LPS Ra molecule obtained from integration along the z-axis (N = 3.8). This shift in the peak position is caused by the penetration of BAC molecules into the outer saccharide units of LPS Ra molecules. Nonetheless, BAC alone was not able to completely dislocate the Ca^{2+} ions cross-linking the inner core of negatively charged LPS Ra molecules, but merely pushed them into a more confined layer.

For the LPS Ra monolayer under the combined influence of 100 mM BzA + 5 µM BAC (red), GIXF analysis could not achieve a reasonable fit due to the loss

of distinct layered structures, indicated by the XRR data (sec. 4.4, fig. 4.6 (C)).

4.6. Discussion

Previous works have studied the modulation of biophysical characteristics and biochemical functions of bacteria in response to sanitisers containing cationic surfactants and aromatic alcohols.[14,15,160] However, the understanding of the synergistic bactericidal mechanism of the two components has not been investigated at molecular level yet. In this study, a defined model of bacterial outer membranes was fabricated by the deposition of LPS Ra monolayers at the air-water interface.

Alterations of structure and electrostatics of LPS Ra membranes by the main ingredients of sanitisers, aromatic alcohol and cationic surfactant, were analysed in a quantitative manner by the combination of structure analysis (XRR) and element-specific ion-localisation (GIXF). As it has been shown that divalent cations, such as Ca^{2+} and Mg^{2+}, facilitate the survival of bacteria,[5–8] the conditions of Ca^{2+}-free and Ca^{2+}-loaded environment were used in the present work to demonstrate the protective role of Ca^{2+}. As control, CFU counting assays verified that the results obtained from the model system can directly be compared to the bactericidal activity of the additives. The concentrations of 10 µM BAC and 100 mM BzA commonly used in sanitisers are not at lethal levels when used as single additives. Thus, to clearly discriminate the differential roles of the two compounds in the presence and absence of Ca^{2+}, simultaneous XRR and GIXF experiments were carried out, under a slightly milder condition of 5 µM BAC and 100 mM BzA.

First, the solitary effect of 100 mM BzA on the LPS membrane was examined (cf. sec. 4.2 and 4.5). The simultaneous XRR and GIXF demonstrated that BzA slightly roughens the interface between hydrocarbon chains and saccharide head groups, but the layered structures and the electrostatic barriers remain intact. XRR data gave quantitative insight to previously reported effects that the increase in membrane fluidity is caused by the roughening of the interface between the hydrocarbon chains and saccharide head groups,[161,162] while the concentration and distribution of cations in close vicinity to the membrane remained unchanged. Second, the solitary effect of 5 µM BAC on the LPS membrane was examined (cf. sec. 4.3 and 4.5), where compared to BzA, the impact of BAC was more significant. Analysis of $\pi - A$ isotherms under Ca^{2+}-free conditions showed a remarkable

expansion of the mean molecular area in the presence of 5 µM BAC, and XRR and GIXF suggested that the layered structures of the LPS Ra membrane were significantly disturbed. This is consistent with the fact that no bacteria could survive in the absence of Ca^{2+} ions at concentrations of $\geq 1\,\mu M$ BAC (appendix A.1 figure A.2 (B)), where a penetration of the outer leaflet of the bacterial membrane by surfactants allows the dissolution of inner phospholipid structures, and subsequent loss of peptidoclycan and cytosol. In contrast to the Ca^{2+}-free condition, XRR data suggested that BAC alone did not disturb the structural integrity of the LPS Ra membrane in Ca^{2+} containing environment, but pushed the Ca^{2+} layer closer to the interface.

Remarkably for the combined presence of 100 mM BzA and 5 µM BAC, XRR data indicated that the mixture of additives disturbed the stratified LPS Ra structures even under Ca^{2+}-loaded conditions (cf. sec. 4.4). This finding provides direct evidence of the synergy of BzA and BAC from a structural point of view, which was quantitatively supported by the element-specific localisation of K^+ and Ca^{2+} ions using GIXF (cf. sec. 4.5). On one hand, the condensation of Ca^{2+} was not disturbed in the solitary presence of BAC due to the blocked incorporation by cross-linked core saccharides. On the other hand, the ion concentration profiles near the interface could not be calculated in the coexistence of BAC and BzA due to the loss of structural integrity. Interestingly, the concentration of BzA seemed to have a significant influence on the synergistic effect of both additives. For instance, in the presence of Ca^{2+} a lower concentration of 50 mM BzA in combination with 5 µM BAC left the LPS Ra monolayer intact (cf. appendix A.3 figure A.3 (E)). Therefore, it can be concluded that the bactericidal effect of sanitisers is facilitated by the roughening of the head-chain interface via BzA, whereby the increased permeability allows the incorporation of BAC into the LPS Ra membrane and subsequently leads to the creation of defects in the membrane structures and loss of cytosol.

These results demonstrate that the structural characterisation by XRR within sub-Å resolution, combined with the element-specific ion localisation by GIXF within few Å resolution, is a powerful tool to unravel the physical mechanism of reactions at biological interfaces.

5. Static and Dynamic Behaviour of hHSC - Experiment and Simulation

5.1. Influence of ADH-1 on Static and Dynamic Behaviour of hHSC

In the following chapter the influence of the clinical drug ADH-1 on the adhesion, deformation, and migration of hHSC on surrogate substrates displaying N-cadherin will be presented and discussed. In section 5.1.1, the adhesion of HSC in absence and presence of ADH-1 is investigated in terms of fraction of adherent cells, adhesion area, and critical pressure for cell detachment. Experiments are performed using reflection interference contrast microscopy (RICM) and picosecond laser pulse induced shockwaves for cell detachment. In sections 5.1.2 and 5.1.3, the deformation and migration of HSC is investigated using time-lapse microscopy and numerical simulations.

5.1.1. Adhesion Area and Strength

Adhesion of HSC on N-cadherin functionalised substrates was investigated using reflection interference contrast microscopy (RICM) and laser-induced cell detachment, resulting in the measurement of adhesion area, fraction of adherent cells, and the critical pressure P^* for cell detachment.

Area of Adhesion In figure 5.1 the results from RICM experiments are presented. Figure 5.1 (A) shows the phase contrast (left) and RICM image (right) of hHSCs on model surfaces displaying N-cadherin at intermolecular distance of

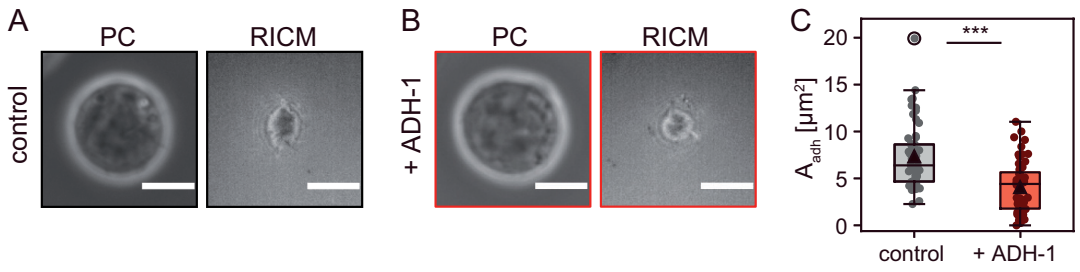

Figure 5.1.: Adhesion area in the absence and presence of ADH-1. Phase contrast (left) and RICM (right) images of HSC adhering to N-cadherin in **(A)** absence (black) and **(B)** presence (red) of ADH-1, scale bars 5 µm. Area of tight adhesion indicated by dark area of destructive interference in RICM images. **(C)** Cell adhesion area ($N > 52, p = 1.3 \times 10^{-6}$, two-sided Mann-Whitney test).

$\langle d \rangle = 18\,\text{nm}$, in absence of ADH-1 (scale bars 5 µm). In the RICM image, the area of close contact is visible by the area of minimum intensity caused by destructive interference at the center of the cell, surrounded by the typical Newton's rings generated by the increasing height between lower cell membrane and substrate. Figure 5.1 (B) shows the phase contrast (left) and RICM image (right) of hHSCs in the presence of 0.5 µg/ml ADH-1, scale bars representing 5 µm. The area of close contact visible in the RICM image is smaller compared to the control sample.

To determine the area of tight adhesion, height fluctuations of the cell membrane were analysed by MSA calculations of intensity fluctuations in the area of close contact as described in section 2.3. Figure 5.1 (C) shows the results of MSA analysis, for $N > 52$ cells from 3 independent experiments each. For control samples, the average area of tight adhesion was $7.4 \pm 3.4\,\mu\text{m}^2$, while in the presence of ADH-1, the average area of tight cell adhesion was reduced to $4.1 \pm 2.8\,\mu\text{m}^2$ ($p = 1.3 \times 10^{-6}$, two-sided Mann-Whitney test). This result proves the significant 1.8-fold reduction of adhesion area caused by the presence of clinical drug ADH-1.

Fraction of Adherent Cells Results from laser pulse assay experiments are shown in Figure 5.2. Prior to the measurement of the critical pressure for cell detachment, all samples were exposed to a shock wave induced by a 0.5 mJ laser pulse to remove non-adherent cells. Analysis of adherent vs. non-adherent cells showed an average of $73 \pm 10\,\%$ adherent cells for the control sample, while in the presence of ADH-1 the adherent fraction was reduced to $37 \pm 11\,\%$ (Figure 5.2 (A)). This reduction by factor of 2 was highly significant ($N > 750$, $p = 5 \times 10^{-7}$,

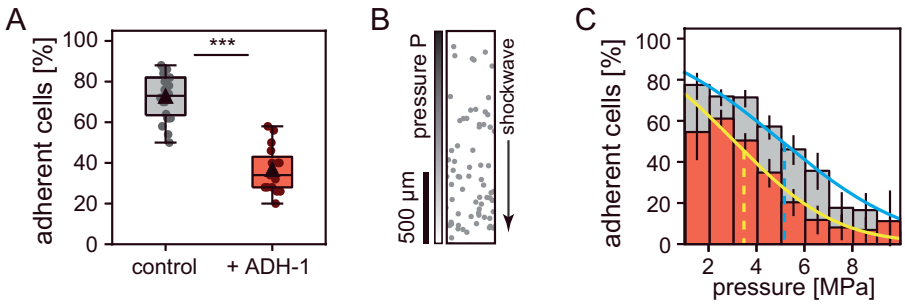

Figure 5.2.: Fraction of adherent cells and adhesion strength in the absence and presence of ADH-1. (A) Total fraction of adherent cells in absence (grey) and presence (red) of ADH-1 ($N > 750, p = 5 \times 10^{-7}$, two-sided Mann-Whitney test, each datapoint representing 50 cells). **(B)** Positions of adherent cells in absence of ADH-1, after exposure to pressure wave emanating from top to bottom. **(C)** Fraction of adherent cells in dependence on detachment pressure P. Fitted error function (blue and yellow curves) presented for indication of critical pressure P^* (broken lines). Significant difference between samples (Kolmogorov-Smirnov test for goodness-of-fit, $p < 0.05$), each bar representing 50 – 700 individual cells.

two-sided Mann-Whitney test).

Critical Pressure for Cell Detachment Bright field images of samples were analysed before and after exposure to a shock wave induced by a 12.7 mJ laser pulse. Positions of adherent cells after exposure to the pressure wave emanating from top to bottom are plotted in Figure 5.2 (B), where the lower cell density in the area exposed to higher pressure is clearly visible. Cells classified as adherent and non-adherent were counted in dependence on the induced pressure, binned, and plotted as adherent fractions in bins of equal ΔP, containing 50 – 700 individual cells per bin. Figure 5.2 (C) shows the resulting empirical distribution of adherent fraction against the applied pressure range for control samples (left, grey) and samples treated with 0.5 µg/ml ADH-1 (right, red). Empirical distributions were fitted as described in section 2.4 with an adapted error function for determination of the critical pressure of cell detachment P^* at the inflection point. The derivative Gaussian of the fitted error function (blue, solid line) is plotted on the right y-axis for indication of critical pressure P^* (blue, broken line).

In the presence of ADH-1, the critical pressure for cell detachment was reduced from 5.1 ± 2.0 MPa (control) to 3.4 ± 2.0 MPa (ADH-1) by a factor of 1.5. Due to the extended transition range between adhesion and detachment, the derivative Gaussian function corresponding to the fitted error functions could not be

utilised to determine statistical significance between the determined critical pressure P^*. Therefore, both data sets and fit curves were compared using an adapted Kolmogorov-Smirnov test for goodness-of-fit[154] as described in section 3.5.2. Analysis showed that both empirical distributions were significantly different from the respective other fitted error function at a significance level of $\alpha = 0.05$.

Discussion

Compared to previously published data on hHSC adhering to surrogate substrates displaying N-cadherin at $\langle d \rangle = 18\,\mathrm{nm}$,[22,87] control experiments in the present study exhibited a lower fraction of adherent cells and lower adhesion areas, but higher critical pressure for detachment P^*. These deviations can arise from the fact that hHSC were extracted from human donors, where behavioural variations exist between individual groups of donors. Furthermore, the critical pressure for cell detachment can not be directly compared to previous studies[22] due to the different experimental procedure used in this work. In the present study, one pressure wave induced by a single laser pulse was applied to each sample, and analysed by pressure variation at distances from 1.5 – 3.5 mm between cells and the laser focus. In Burk *et al.*,[22] however, single cells were exposed to multiple pressure waves with increasing pressure values, until detachment was observed. This repeated exposure to detachment forces can lead to a weakening of the adhesion on the N-cadherin axis. Nonetheless, the overall effect of ADH-1 can be compared to the values determined by Burk *et al.*[22] and Monzel *et al.*[87] By the administration of 0.5 µg/ml ADH-1 to the cells, the reduction of adhesion parameters was comparable to the binding-to-unbinding transition occurring at lower lateral lig-

Table 5.1.: Adhesion parameters of hHSC in the absence and presence of ADH-1 on surrogate substrates displaying N-cadherin at intermolecular distances of $\langle d \rangle = 18\,\mathrm{nm}$ 2 h after seeding. Average values of 3 independent experiments considering $N > 50$ – 2000 cells, ± standard deviation.

	control	+ ADH-1
A_{adh} [µm^2]	7.4 ± 3.4	4.1 ± 2.8
χ [%]	73 ± 10	37 ± 11
P^* [MPa]	5.1 ± 2.0	3.4 ± 2.0

and densities. In Burk *et al.*, this transition occurred at intermolecular distances of $\langle d \rangle = 30 - 50\,\mathrm{nm}$, where the adherent fraction decreased below 50% and the adhesion area was reduced to less than $4\,\mu\mathrm{m}^2$. Furthermore, the critical pressure for cell detachment P^* also is proportional to lateral ligand density.

These results present a strong indication that ADH-1 directly blocks N-cadherin on the surrogate substrates, where the reduction of adhesion parameters can be explained by the reduction of accessible binding sites, which is comparable to a lower surface density of N-cadherin.

5.1.2. Deformation Analysis and Simulations

For deformation analysis, sequences of phase contrast images were recorded over 1 h at a Δt of $40 - 70\,\mathrm{s}$, 2 h after cell seeding as described in section 3.5.3. After binarisation, cell contours were extracted from each frame, transformed into polar coordinates, and analysed regarding their Fourier coefficients (cf. sec. 2.5). Based on the experimental results, numerical simulations were performed according to the model established by Ohta *et al.*[63,86] Parameters g_c/κ_2 in equations 2.93 – 2.96 were adjusted to match the simulated behaviour to the experimentally observed deformation, as described in section 3.6.

Experiment Figure 5.3 (A) shows the outlines of deforming hHSC in the absence (left, grey) and presence (right, red) of ADH-1 for experiments (top row, grey panels). In the control experiments, hHSCs showed pronounced deformation, while in the presence of ADH-1 the active deformation was distinctly reduced.

For quantitative analysis and reproduction of results, the deformation of hHSCs was analysed in Fourier space to calculate the power spectrum and total power of deformation. Figure 5.3 (B) shows the experimentally determined power spectrum of hHSCs deforming in the absence (solid line, grey) and presence (solid line, red) of ADH-1. In both samples, the contribution of mode 2 deformation to the overall shape of the cell is most pronounced, followed by mode 3, which identifies elongation as the predominant mode of deformation. In the presence of ADH-1, the deformation power of all modes was reduced compared to the control sample. Furthermore, the ratio Γ_2/Γ_3 between mode 2 and mode 3 deformation power was increased from 2.1 (control) to 2.9 by a factor of 1.4 in the presence of ADH-1.

The total power of deformation calculated from the power spectra is presented

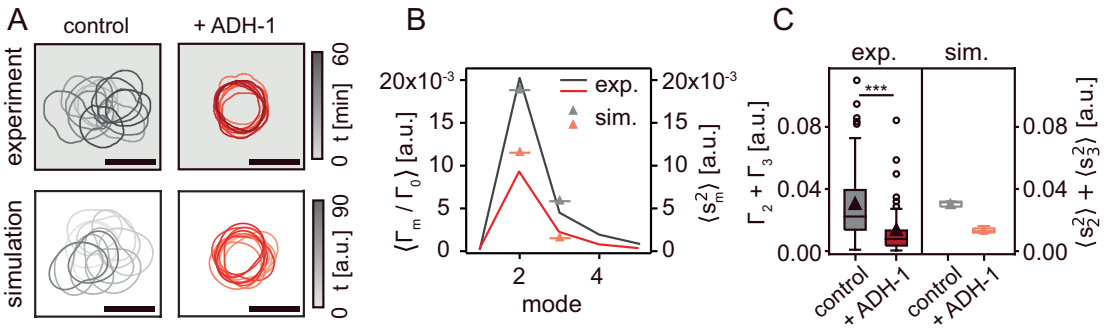

Figure 5.3.: Deformation analysis and simulations in the absence and presence of ADH-1. **(A)** Experimentally tracked (top, grey panels) and numerically simulated (bottom, white panels) cell deformation over time in absence (grey) and presence (red) of ADH-1. Scale bars of 10 µm equivalent to 2 simulated length units, 1 minute in experiments equiv. to 1.5 simulated time units. **(B)** Power spectra and **(C)** sum of deformation powers of mode 2 and mode 3, calculated from cell shapes in experiments (solid boxes, left) and determined by deformability $\langle s_2^2 \rangle + \langle s_3^2 \rangle$ in simulations (open boxes, right). Reduction of sum of deformation power by factor of 2.2 ($N > 36, p < 0.001$, two-sided Mann-Whitney test).

in figure 5.3 (C) for experiments (left, solid boxes) and simulations (right, open boxes). For experiments, analysis resulted in a total power of deformation of $\Gamma_2+\Gamma_3 = 0.031 \pm 0.025$ for control, and $\Gamma_2+\Gamma_3 = 0.014 \pm 0.018$ in the presence of ADH-1. The total power of deformation was reduced by factor of 2.2 in the presence of 0.5 µg/ml ADH-1 (3 independent experiments, $N > 36, p < 0.001$, two-sided Mann-Whitney test). This reduction could be reproduced by adjustment of parameters in the numerical simulations.

Simulation Results from simulations are shown in figure 5.3 (A) bottom row (white panels) for control samples (left, grey) and ADH-1 samples (right, red), with the scale bar of 10 µm equivalent to 2 simulated length units, and 1 minute in the experiments represented by 1.5 simulated time units. As can be seen from the qualitative appearance of plotted cell shapes, the effect of reduced deformation in the presence of ADH-1 could be reproduced.

Starting from the results of the power spectrum analysis, the parameter ratio of intrinsic force g_c vs. line tension κ_2 of cell membrane was adjusted to match the total deformability $\langle s_2^2 \rangle + \langle s_3^2 \rangle$ to the total power of deformation $\Gamma_2 + \Gamma_3$ observed from cell experiments. For control samples, a ratio of $g_c/\kappa_2 = 0.09$ resulted in the deformability of $\langle s_2^2 \rangle + \langle s_3^2 \rangle = 0.031$, matching the experimental result of $\Gamma_2 + \Gamma_3$

Table 5.2.: Deformation parameters of hHSC in the absence and presence of ADH-1 on surrogate substrates displaying N-cadherin at $\langle d \rangle = 18\,\text{nm}$ 2 h after seeding. Average values of 3 independent experiments considering $N > 50 - 2000$ cells, and $N > 40$ independent simulations, ± standard deviation.

	control	+ ADH-1
$\Gamma_2 + \Gamma_3$ [a.u.]	0.031 ± 0.025	0.014 ± 0.018
$\langle s_2^2 \rangle + \langle s_3^2 \rangle$ [a.u.]	0.031	0.014
g_c/κ_2	0.09	0.06

$= 0.031 \pm 0.025$. A reduction of g_c/κ_2 for the ADH-1 sample by factor of 1.5 from 0.09 to 0.06 could reproduce the reduction of $\Gamma_2 + \Gamma_3$ to 0.014 ± 0.018, with a matching $\langle s_2^2 \rangle + \langle s_3^2 \rangle = 0.014$ in the presence of ADH-1. Deformability results from simulations are plotted on the right y-axis of figure 5.3 (C), for control (grey) and ADH-1 (red) samples. In figure 5.3 (B), the contribution $\langle s_m^2 \rangle$ of mode 2 and mode 3 deformation to the overall shape is shown for simulations as solid symbols for control samples (grey) and ADH-1 samples (red). Due to normalisation by, units for experiments and simulations are directly transferable. The increase of ratio Γ_2/Γ_3 obtained from power spectrum analysis of experiments in the presence of ADH-1 by factor of 1.4 could be simulated by increasing the line tension ratio κ_3/κ_2 of mode 2 and 3 deformation from 1.8 (control) to 2.2 (ADH-1) by factor of 1.2.

Discussion

Control experiments showed similar deformation power compared to previous works,[22,87] considering the normalisation by Monzel *et al.*[87] Both the predominant mode of deformation and the reduction in the presence of ADH-1 could be reproduced in the theoretical model by adjustment of parameters g_c, κ_2, and κ_3. In the presence of ADH-1, the parameter ratio g_c/κ_2 was reduced. From the perspective of simulations, this reduction indicates a reduction of intrinsic forces g_c, or enhancement of relaxation rate κ equivalent to a stiffening of the cell.

With this distinction of deformation during migration using power spectral analysis and numerical simulations, an additional perspective is given on cell migration, which is only probed by start-to-end point observation in commonly applied screen-

ing studies. Since in the presence of ADH-1 deformation activity is significantly reduced, further details about the influence of ADH-1 on intrinsic force generation and deformation parameters such as stiffness and membrane tension would be of great interest.

5.1.3. Migration Analysis and Simulations

For migration analysis, cell positions were extracted from binarised images of the time lapse experiments by calculating the center of mass in each frame, and the corresponding trajectories were analysed using the MSD calculation introduced in chapter 2.6.

Experiment Trajectories from migration experiments are shown in the top row (grey panels) of figure 5.4 (A), in the absence (grey, left) and presence (red, right) of 0.5 µg/ml ADH-1. For control samples, cells could reach a total migrating distance of $\sim 20\,\mu m$, while in the presence of ADH-1, the total migrating distance was reduced to $\sim 10\,\mu m$.

Analysis of the MSD of each trajectory resulted in the fitting of the diffusion constant D according to equation 2.57. Results are plotted in figure 5.4 (B) for experiments (left, solid boxes) and simulations (right, open boxes). Control experiments showed an average diffusion constant of $0.97 \pm 0.64\,\mu m^2/min$, while in the presence of 0.5 µg/ml ADH-1, D was reduced to $0.40 \pm 0.33\,\mu m^2/min$ by factor of 2.4 ($N > 36, p < 0.001$, two-sided Mann-Whitney test).

Figure 5.4 (C) shows the results from ACF analysis of migration direction as described in section 2.6. Persistence time τ from experiments is plotted in solid boxes (left) for control (grey) and ADH-1 (red) samples. In the absence of ADH-1, trajectories showed an average persistence time of $\tau = 88 \pm 26\,s$, while the presence of ADH-1 reduced τ to 72 ± 19 by factor of 1.2. ($N > 36, p < 0.001$, two-sided Mann-Whitney test)

Simulation Results from simulations are plotted in white panels (bottom row) of figure 5.4 (A), for both control (grey) and ADH-1 (red) samples. Unit settings for the simulations define 1 simulated length unit as 5 µm, therefore the plotted radius of max. 6 units corresponds to the plotted radius of max. 30 µm. The extension and reduction of trajectory length in the absence and presence of ADH-1

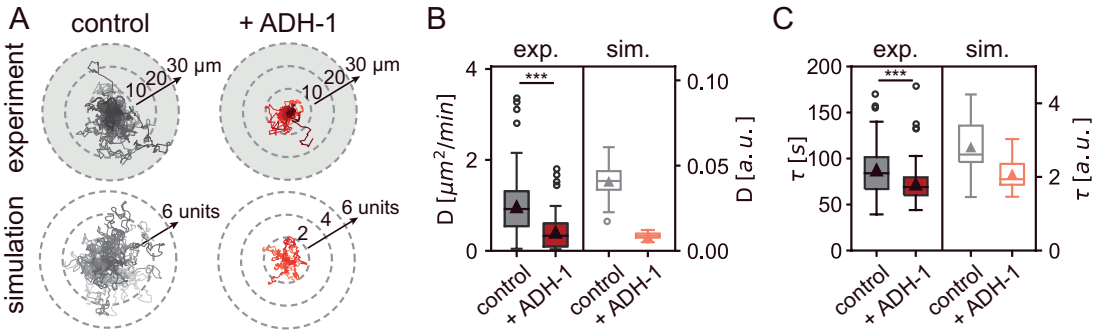

Figure 5.4.: Migration analysis and simulations in the absence and presence of ADH-1. (A) Experimentally determined (top, grey panels) and numerically simulated (bottom, white panels) trajectories of hHSCs migrating in absence (grey) and presence (red) of ADH-1. **(B)** Diffusion constant D and **(C)** persistence time τ of trajectories for experiments (solid boxes, left) and simulations (open boxes, right). Reduction of D by factor of 2.4 and reduction of τ by factor of 1.2 in presence of ADH-1 ($N > 36, p < 0.001$, two-sided Mann-Whitney test). Note: $1\,\mu\text{m} = \frac{1}{5}\,\text{l.u.}$, $1\,\text{min} = 1.5$ t.u., and $1\,\mu\text{m}^2/\text{min} = \frac{0.04^2}{1.5}\,\frac{\text{l.u.}^2}{\text{t.u.}} = 0.0267\,\frac{\text{l.u.}^2}{\text{t.u.}}$ in experiments and simulations, respectively.

is well reproduced in the simulations. While simulated cells reached a total migrating distance of ~ 4 length units (l.u.) under control conditions, corresponding to 20 µm in real units, simulations of ADH-1 samples led to a reduction of total migrating distance to ~ 2 l.u., which corresponds to 10 µm in real units. As indicated from the qualitative observation of trajectory appearance and dimensions, experimental behaviour could be well reproduced by the simulations.

For quantitative analysis, diffusion constant D and persistence time τ were also calculated for simulations, and matched to the experimental results by choice of the linear model and adjustment of mobility parameter $|\gamma|$ in equation 2.70. Diffusion constants D obtained from simulations are plotted in the right panel of 5.4 (B) (open boxes) for both control (grey) and ADH-1 (red) samples. Due to the definition of length and time units of $1\,\mu\text{m} = \frac{1}{5}$ l.u. and $1\,\text{min} = 1.5$ t.u., a diffusion constant of $1\,\mu\text{m}^2/\text{min}$ in the experiments corresponds to a value of $\frac{0.04^2}{1.5} = 0.0267$ in dimensionless units for the simulations. The reduction of D in the presence of ADH-1 could be reproduced in the simulations by calculating mobility $|\gamma|$ from average velocity $|v|$, Γ_2, and Γ_3, following equation 3.10 as described in section 3.6. For control samples, the setting of $|\gamma| = 8.1 \pm 1.8$ resulted in trajectories of $D = 0.041 \pm 0.013$, corresponding to $1.5 \pm 0.5\,\mu\text{m}^2/\text{min}$ in real units, while for the presence of ADH-1, an increase in mobility $|\gamma|$ by factor of 1.4 to 11.1 ± 3.4

resulted in $D = 0.009 \pm 0.004$, corresponding to $0.3 \pm 0.1\,\mu m^2/min$ in real units.

Results for persistence time τ from simulations are plotted in the right panel of figure 5.4 (C) (open boxes) for control (grey) and ADH-1 (red) samples. Due to the definition of time units, a persistence time of 40 s in the experiments corresponds to a value of 1 t.u. in dimensionless units for simulations. The reduction of τ in the presence of ADH-1 could be reproduced in the simulations. For control samples, the setting of $|\gamma| = 8.1 \pm 1.8$ resulted in trajectories of $\tau = 2.66$, corresponding to 106 s in real units. For simulations of migration behaviour in the presence of ADH-1, an increase of mobility $|\gamma|$ by factor of 1.4 resulted in $\tau = 2.15$, corresponding to 86 s in real units.

Note that the the scattering of simulation values of D, $\langle v \rangle$, and τ arises from the choice of $|\gamma|$ including standard deviation.

Discussion

Compared to previously reported data of hHSC migrating on surrogate substrates displaying N-cadherin at $\langle d \rangle = 18\,nm$, control experiments in the present study exhibited a similar extension of trajectories.[87] Other migration parameters such as diffusion constant and persistence time have not been analysed in this report, but studies on surrogate substrates displaying CXCL12 at $\langle d \rangle = 18\,nm$ showed comparable order of magnitude for diffusion constant D and persistence time τ.[86]

The effect of the administration of 5 µg/ml ADH-1 on migration showed a reduction of diffusion constant, speed, and persistence time. This is in good agreement with previous data of migration assays performed on a human breast cancer cell line, where cell migration was significantly reduced in the presence of ADH-1 mod-

Table 5.3.: Results from migration analysis of experiments in the absence and presence of ADH-1 on surrogate substrates displaying N-cadherin at intermolecular distance of $\langle d \rangle = 18\,nm$ 2 h after seeding. Average values of 3 independent experiments considering $N > 36$ cells, ± standard deviation.

	$control_{exp}$	$+$ ADH-1_{exp}
D [$\mu m^2/min$]	0.97 ± 0.64	0.40 ± 0.33
$\langle v \rangle$ [$\mu m/min$]	2.03 ± 0.66	1.30 ± 0.76
τ [s]	88 ± 26	72 ± 19

Table 5.4.: Results from migration analysis of simulations in the absence presence of 0.5 µg/ml ADH-1. Average values of 40 independent simulations each, ± standard deviation.

	$\text{control}_{\text{sim}}$	+ $\text{ADH-1}_{\text{sim}}$
D [a.u.]	0.041 ± 0.013	0.009 ± 0.004
$\langle v \rangle$ [a.u.]	0.254 ± 0.014	0.109 ± 0.026
τ [a.u.]	2.66 ± 0.86	2.15 ± 0.54
$\lvert\gamma\rvert$	8.1 ± 1.8	11.1 ± 3.4

ified liposomes as well as soluble ADH-1, compared to the control group in the absence of ADH-1.[44]

Both qualitative and quantitative properties of control experiments and experiments in the presence of ADH-1 could be reproduced by application of the linear model for cell crawling presented by Ohta *et al.*[63,86] From the absence of persistent behaviour, the linear case of $b_0 = d_0 = 0$ in equations 2.93 – 2.96 was chosen for numerical simulations. Adjustment of mobility parameter $|\gamma|$ showed that the presence of 5 µg/ml ADH-1 causes an increase in mobility by factor of 1.4. This is in good agreement with the findings of reduced adhesion parameters presented in section 5.1.1, which strengthens the conclusion that ADH-1 blocks the accessible binding sites of N-cadherin displayed on the substrate and thereby reduces the friction between cells and substrate.

5.1.4. Summary

In this section, the effect of an external stimulus to the adhesion axis mediated via N-cadherin was presented and analysed. By the administration of 0.5 µg/ml ADH-1, adhesion as well as deformation and migration parameters of hHSC migrating on surrogate substrates were significantly reduced.

The results of reduced adhesion area and strength are in good agreement with previous publications regarding interruption of cell-cell adhesion by the application of ADH-1,[45,163] as well as reduction of migration behaviour.[44] The results presented in the current work indicate that ADH-1 directly blocks N-cadherin on the surrogate substrates, where the reduction of adhesion parameters can be ex-

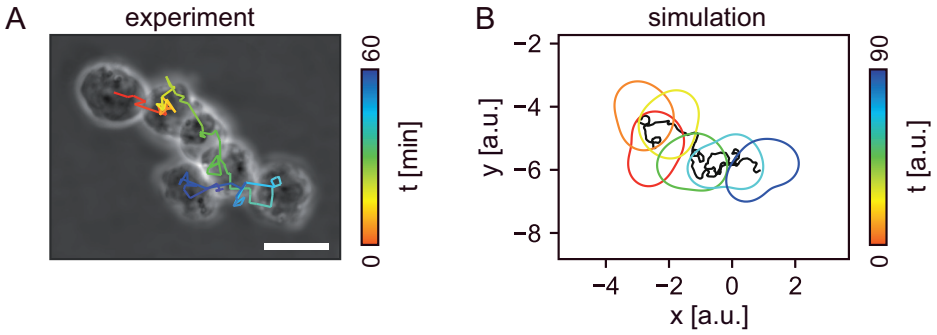

Figure 5.5.: Experiment and Simulation. Time series from **(A)** experimentally tracked and **(B)** numerically simulated cell deforming and migrating in absence of ADH-1. Scale bar of 10 µm equivalent to 2 simulated length units, 1 minute in experiments equiv. to 1.5 simulated time units.

plained by the reduction of accessible binding sites.

Furthermore, reduced migration behaviour was investigated by applying a simple model of cell crawling in 2D.[63,86] Taking the adjustment of deformability parameter g_c/κ_2 together with mobility parameter $|\gamma|$ for migration, numerical simulations led to good agreement between computation and experiments. Figure 5.5 (A) presents the overlay of phase contrast images from time-lapse experiments for different time points during 60 minutes of tracking time, illustrating the propagation of cell shape and position (i.e. deformation and migration) of hHSCs over time. In figure 5.5 (B), the result from simulations of an equivalent time series is presented, outlining the modelled shapes (colour gradient from red to blue) and trajectory (black) over simulated time of 90 units. Due to the normalisation of 1 length unit equiv. 5 µm, length scales in both illustrations are comparable, demonstrating the qualitative agreement between simulations and experimental observations. Moreover, the analysis of migration parameters as well as deformation power showed good quantitative agreement between simulation and experiments.

Combined results of experiments and numerical simulations strongly indicate that reduced deformability in the presence of ADH-1 dominates the outcome of reduced migration behaviour. Therefore, the reduction of migration behaviour is not a result of lacking mobility but indeed caused by deficient deformation activity. Both the results of adhesion parameters from experiments as well as the mobility parameter obtained from simulations show that friction between cells and substrate is reduced by the presence of ADH-1. This detailed and differentiated effect of clinical drug ADH-1 could not be shown by stand-alone experiments before.

5.2. Simulation of Dynamic Behaviour under the Influence of N-cadherin

Following the effect of ADH-1 on blocking accessible adhesion sites on N-cadherin functionalised substrates, the adhesion mediated via N-cadherin is further investigated using numerical simulations of deformation induced cell migration. In the following chapter the influence of ligand spacing on the deformation and migration of hHSC on surrogate substrates displaying N-cadherin will be presented and discussed. In section 5.2.1, the results from deformation analysis of hHSC on different ligand spacing of N-cadherin are reproduced by the theoretical model. Furthermore, the migration behaviour of hHSCs under the same conditions are simulated and discussed in section 5.2.2. All experiments on intermolecular distances of $\langle d \rangle$ = 6, 34, and 47 nm were performed by Dr. Alexandra S. Becker.

5.2.1. Simulation of Cell Deformation

Figure 5.6 displays the results from deformation analysis[†] (solid boxes, black symbols) alongside the results from numerical simulations (grey symbols) of hHSCs deforming on $\langle d \rangle$ = 6, 18, 34, and 47 nm in the absence of further additives. On substrates displaying N-cadherin at lowest intermolecular distance of $\langle d \rangle = 6$ nm, $\Gamma_2 + \Gamma_3$ showed similar values compared to control experiments on $\langle d \rangle = 18$ nm presented in section 5.1.2. Deformation power on $\langle d \rangle = 34$ nm remained unchanged (0.032 ± 0.023), while the $\Gamma_2 + \Gamma_3$ of hHSC migrating on highest ligand spacing $\langle d \rangle = 47$ nm exhibited a strong reduction by factor 1.4 to 0.022 ± 0.012. In summary, $\Gamma_2 + \Gamma_3$ showed elevated values for 18 and 34 nm, but was decreased at the highest (6 nm) and lowest (47 nm) ligand densities.

For numerical simulations, the parameter ratio g_c/κ_2 was adjusted for each sample to reach the deformability $\langle s_2^2 \rangle + \langle s_3^2 \rangle$ equivalent to values of $\Gamma_2 + \Gamma_3 \pm 10\,\%$ obtained from experiments. As a reference, the value of $g_c/\kappa_2 = 0.09$ was used for $\langle d \rangle = 18$ nm, as obtained and presented in section 5.1.2. On substrates displaying $\langle d \rangle = 6$ nm N-cadherin, g_c/κ_2 was reduced to 0.087 to reproduce the minor reduction of $\Gamma_2 + \Gamma_3$ from 0.031 to 0.028 by factor 0.9. Since samples on 34 nm N-cadherin showed similar values of total power as samples on 18 nm N-cadherin,

[†] Dr. Alexandra S. Becker, unpublished data

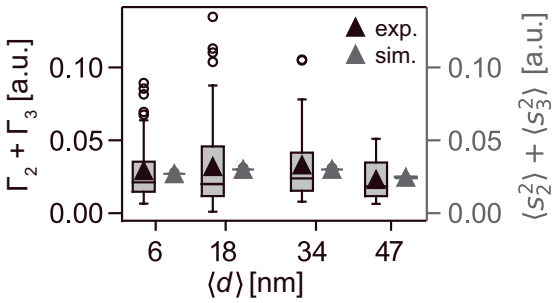

Figure 5.6.: Cell deformation in dependence on intermolecular distance between ligand molecules N-cadherin. Sum of deformation powers of mode 2 and mode 3, calculated from cell shapes in experiments† (solid boxes, black symbols) and determined by deformability $\langle s_2^2 \rangle + \langle s_3^2 \rangle$ in simulations (grey symbols). Simulations in good agreement with experimental results, all experiments were performed by Dr. Alexandra S. Becker.

g_c/κ_2 was held almost constant at 0.089. To reproduce the reduction of deformability to 0.022 on substrates displaying 47 nm N-cadherin, g_c/κ_2 was reduced to 0.078 by factor 0.87 compared to the value obtained for 18 nm N-cadherin.

5.2.2. Simulation of Cell Migration

Results from cell migration experiments† (solid boxes, black symbols) and simulations are presented in figure 5.7, on substrates functionalised with N-cadherin of various $\langle d \rangle$. In figure 5.7 (A), trajectories from experiments† (top, grey panels) and simulations (bottom, white panels) are plotted for ligand spacing $\langle d \rangle = 6$, 34, and 47 nm (left to right), for $N > 40$ cells each. As defined in section 3.6, unit settings for the simulations define 1 simulated length unit as 5 µm, therefore the plotted radius of max. 6 units corresponds to the plotted radius of max. 30 µm. For the lowest ligand spacing of $\langle d \rangle = 6$ nm, trajectories of migrating cells reach a net migrating distance of 20 – 30 µm. For reduced ligand density ($\langle d \rangle = 34$ and 47 nm), the net distance reached by migration is reduced to $\sim 10 - 20$ µm.

The effect of decreasing migrating distance with increasing ligand spacing could be reproduced by numerical simulations. While for simulations of $\langle d \rangle = 6$ nm the simulated trajectories reach a net distance of 4 – 6 l.u. corresponding to 20 – 30 µm in real units, this extension is reduced to 2 – 4 l.u. for simulations on $\langle d \rangle = 34$ nm ligand spacing, and further compacted for simulations on $\langle d \rangle = 47$ nm.

† Dr. Alexandra S. Becker, unpublished data

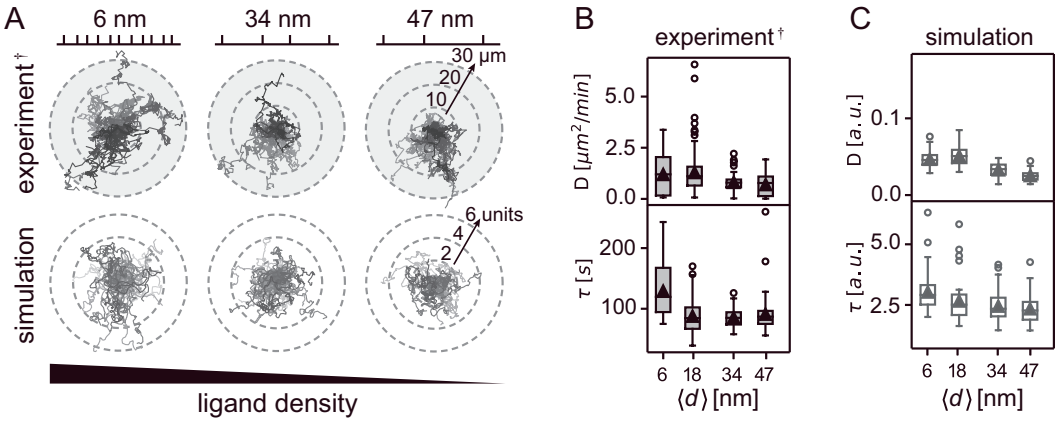

Figure 5.7.: Cell migration in dependence on intermolecular distance between ligand molecules N-cadherin. (A) Experimentally determined† (top) and numerically simulated (bottom) trajectories of hHSCs migrating on substrates functionalised with N-cadherin of ligand spacing $\langle d \rangle$ = 6, 34, and 47 nm, for $N > 40$ trajectories each. **(B)** Diffusion constant D and persistence time τ of trajectories from experiments†. **(C)** Diffusion constant D and persistence time τ from simulations. Simulations in good agreement with experimental results, all experiments were performed by Dr. Alexandra S. Becker.

Figure 5.7 (B) shows the results of MSD- and ACF-analysis of experimental† trajectories according to section 2.6. Diffusion constant D obtained from MSD-analysis (upper panel) exhibits highest values for highest ligand densities ($\langle d \rangle$ = 6, 18 nm), and decreases with increasing ligand spacing. For persistence time τ obtained from ACF-analysis (bottom panel), the maximum value is obtained at the highest ligand density ($\langle d \rangle$ = 6 nm), and decreases rapidly with increasing ligand spacing.

Results from MSD- and ACF-analysis of simulated trajectories are presented in figure 5.7 (C). Mobility $|\gamma|$ was adjusted for each sample to match diffusion constant D and persistence time τ equivalent to the corresponding values ±10% obtained from experiments performed by Dr. Alexandra S. Becker. As a reference, the value of $|\gamma| = 8.1 \pm 1.8$ was used for simulations on $\langle d \rangle$ = 18 nm, as obtained and presented in section 5.1.3. For substrates displaying N-cadherin at $\langle d \rangle$ = 6 nm, simulations matching a reduced D of 0.90 ± 0.72 µm²/min and an elevated τ of 129 ± 42 s were reached by reducing $|\gamma|$ to 7.90 ± 0.60 in combination with a reduced parameter ratio κ_3/κ_2, as observed from the ratio of deformation powers Γ_3/Γ_2 in experiments†. For substrates displaying N-cadherin at $\langle d \rangle$ = 34 nm,

† Dr. Alexandra S. Becker, unpublished data

simulations matching a reduced D of $0.81 \pm 0.52\,\mu m^2/min$ and a similar τ of $86 \pm 16\,s$ were reached by keeping $|\gamma|$ at 8.00 ± 0.80 and adjusting κ_3/κ_2 to Γ_3/Γ_2 from experiments. For substrates displaying N-cadherin at $\langle d \rangle = 47\,nm$, simulations matching a reduced D of $0.70 \pm 0.53\,\mu m^2/min$ and a similar τ of $91 \pm 32\,s$ were reached by increasing the mobility $|\gamma|$ to 10.0 ± 0.7 in combination with the reduced deformability $\langle s_2^2 \rangle + \langle s_3^2 \rangle$.

5.2.3. Discussion

The mechanism of hHSCs adhering and migrating on N-cadherin-functionalised substrates seems to be fundamentally different from the pinning effect of other ligand molecules such as E-cadherin, P-selectin, or CXCL12.[41,86] Previous studies of hHSC migrating on CXCL12-functionalised substrates have shown an increased extension of trajectories as well as migration parameters with increasing ligand spacing.[86] Panorchan *et al.* showed that N-cadherin acts as a dynamic adhesive promoting cell movement, in contrast to E-cadherin, which works as a static adhesive similar to the previously reported effect of CXCL12.[41,86] Furthermore, Panorchan *et al.* uses the analogy of a rolling wheel to describe the mechanism of homophilic N-cadherin adhesion, where the dynamic behaviour of N-cadherin is necessary for exertion of propulsive forces from cells to the environment, similar to the friction of a rolling wheel.[41] This description of a 'dynamic adhesion' is in agreement with the simulations presented in this work. At high densities of N-cadherin displayed on the surrogate substrates, low mobility parameter $|\gamma|$ indicates higher friction to the substrate, which means that cells are able to exert

Table 5.5.: Results from deformation and migration analysis of experiments[†] on surrogate substrates displaying N-cadherin at intermolecular distances of $\langle d \rangle = 6 - 47\,nm$, 2 h after seeding. Average values of 3 independent experiments considering $N > 40$ cells, ± standard deviation.

	6 nm[†]	18 nm	34 nm[†]	47 nm[†]
$\Gamma_2 + \Gamma_3$ [a.u.]	0.028 ± 0.021	0.031 ± 0.025	0.032 ± 0.023	0.022 ± 0.012
D [$\mu m^2/min$]	0.90 ± 0.72	0.97 ± 0.64	0.81 ± 0.52	0.70 ± 0.53
τ [s]	129 ± 42	88 ± 26	86 ± 16	91 ± 32

Table 5.6.: Results from simulations considering surrogate substrates displaying N-cadherin at $\langle d \rangle = 6 - 47\,\mathrm{nm}$. Average values in dimensionless units of $N = 40$ independent simulations each, ± standard deviation.

	6 nm	18 nm	34 nm	47 nm
$\langle s_2^2 \rangle + \langle s_3^2 \rangle$	0.027	0.031	0.030	0.024
g_c/κ_2	0.087	0.090	0.089	0.078
$\lvert\gamma\rvert$	7.9 ± 0.6	8.1 ± 1.8	8.0 ± 0.8	10.0 ± 0.7

propulsion forces to their micro-environment.

In the occurrence of reduced deformation power at lower densities of N-cadherin-functionalised substrates, however, the relative increase of mobility parameter $|\gamma|$ was not as high as the adjustment of $|\gamma|$ in previously reported simulations on substrates displaying CXCL12.[86] For N-cadherin, a mobility of $|\gamma|_{\mathrm{Ncad}} = 8 - 10$ was determined in the present work, while in the work of Ohta *et al.*, for migration on CXCL12-functionalised substrates $|\gamma|_{\mathrm{CXCL12}}$ was set to $5 - 7$ for the same extension of trajectories, as well as parameters D and τ. This observation of reduced friction between cells and substrate when comparing N-cadherin and CXCL12 is consistent with the results of adhesion parameters presented in section 5.1.1.

In general, from the qualitative observation of trajectory appearance as well as quantitative analysis of migration parameters, the experimental[†] behaviour of hHSC could be reproduced. Similar to the behaviour of deformation power and mobility in the presence of clinical drug ADH-1 (cf. sec. 5.1.2), results presented in the current section also exhibited an increase in mobility, combined with a decrease in deformation activity and migration. This strongly indicates that the reduction in migration behaviour is dominated by a lack of deformation activity, while the mobility of cells is indeed increased by the reduction of accessible binding sites of N-cadherin on the substrates. This finding strengthens the conclusion for the influence of ADH-1, where the effect of reduced dynamic behaviour combined with increased mobility was observed in a more pronounced manner.

[†] Dr. Alexandra S. Becker, unpublished data

5.3. Simulation of Dynamic Behaviour under the Influence of NOX-A12

In the following section, simulations of deformation and migration of hHSC under the effect of chemokine CXCL12 as well as Spiegelmer NOX-A12 will be presented and discussed. All experiments in this section were performed and published by Dr. Cornelia Monzel and Dr. Alexandra S. Becker.[87]

As reported in Monzel *et al.*, adhesion area of hHSCs on substrates displaying N-cadherin at intermolecular distances of $\langle d \rangle = 18\,\mathrm{nm}$ was not influenced by the administration of soluble CXCL12 or NOX-A12.[87] The dynamic behaviour, however, was strongly influenced by the presence of NOX-A12, even in the absence of its antagonist CXCL12. Therefore, it is of great interest to investigate the differential effect of NOX-A12 on deformation and migration using numerical simulations of self-propelled cells.

5.3.1. Simulation of Cell Deformation and Migration

Figure 5.8 shows the results of cell deformation and migration experiments[‡] and simulations on substrates functionalised with $\langle d \rangle = 18\,\mathrm{nm}$ N-cadherin, in the presence of soluble CXCL12 and NOX-A12. In figure 5.8 (A), trajectories from experiments[‡] (top, grey panels) and simulations (bottom, white panels) are plotted for the addition of 5 ng/ml sol. CXCL12 (green), 50 ng/ml NOX-A12 (blue), and 500 ng/ml NOX-A12 (purple). As defined in section 3.6, unit settings for the simulations define 1 simulated length unit as 5 µm, therefore the plotted radius of max. 6 units corresponds to the plotted radius of max. 30 µm.

In the presence of sol. CXCL12, trajectories of migrating cells are compacted and reach a net migrating distance of 10 – 20 µm. In the presence of NOX-A12, trajectories are more stretched and the net distance reached by migration is enhanced to $\sim 20 - 30$ µm. Increasing the concentration of NOX-A12 by factor of 10 did not increase the stretching of trajectories or the net distance of migration.

By adjusting the mobility parameter $|\gamma|$, this trend could be reproduced using numerical simulations. While for simulations in the presence of sol. CXCL12 the simulated trajectories reach a net migrating distance of ~ 4 l.u., this extension is

[‡] adapted with permission from Monzel *et al.*[87]

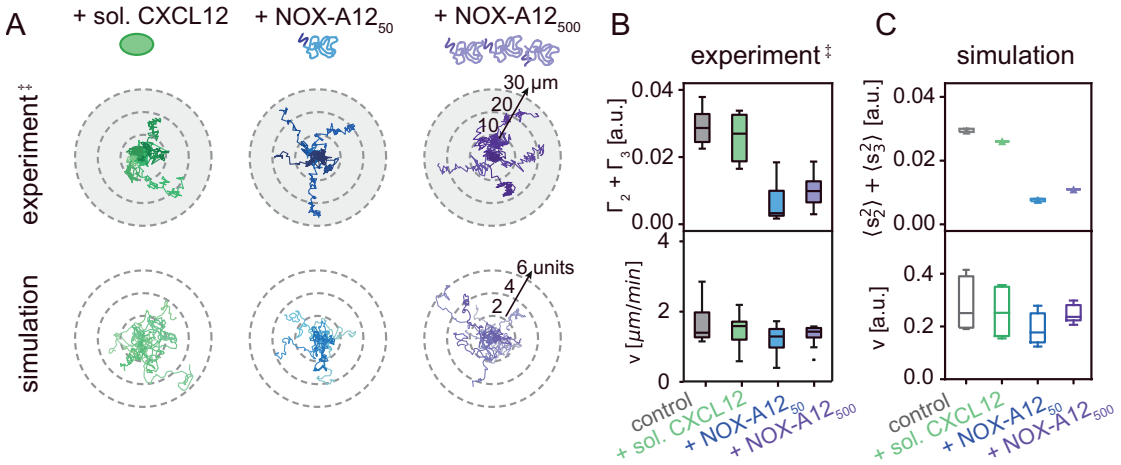

Figure 5.8.: Cell migration in the presence of chemokine and synthetic agent. **(A)** Experimentally determined‡ (top, grey panels) and numerically simulated (bottom, white panels) trajectories of hHSCs migrating on substrates functionalised with $\langle d \rangle = 18\,\text{nm}$ N-cadherin in the presence of sol. CXCL12 (green), NOX-A12$_{50}$ (blue), and NOX-A12$_{500}$ (purple). **(B)** Sum of deformation powers of mode 2 and mode 3 (top) and migration velocity $\langle v \rangle$ (bottom), calculated from experiments‡, considering $N > 30$ cells each. **(C)** Sum of deformability $\langle s_2^2 \rangle + \langle s_3^2 \rangle$ (top) and migration velocity $\langle v \rangle$ in simulations, considering $N > 40$ independent simulations each. Boxplots representing data minimum, maximum, sample median, and the first and third quartiles. Simulations in good agreement with experimental results, all experiments were performed and published by Dr. Cornelia Monzel and Dr. Alexandra S. Becker.‡

enhanced to 4 – 6 l.u. for simulations in the presence of NOX-A12$_{500}$.

Figure 5.8 (B) displays the results from deformation analysis (upper panel, renormalised to currently used units a.u.) and migration analysis (lower panel) of experiments‡ in the presence of soluble CXCL12 and NOX-A12. In the presence of sol. CXCL12, total deformation power remained unchanged at 0.027 – 0.030 compared to the control samples in the absence of additives, but was significantly decreased to values below 0.010 in the presence of NOX-A12. For migration velocity $\langle v \rangle$, no significant difference between samples was observed, values in the range of $\langle v \rangle = 1.3 - 1.6\ \mu\text{m/s}$ remained similar in all samples.[87]

Results obtained from simulations are presented in figure 5.8 (C). Parameter ratio g_c/κ_2 was adjusted for each sample to reach the deformability $\langle s_2^2 \rangle + \langle s_3^2 \rangle$ (upper panel) equivalent to $\Gamma_2 + \Gamma_3 \pm 10\%$ as reported by Monzel *et al.*[87] As a reference, the value of $g_c/\kappa_2 = 0.09$ was used for control samples, as obtained and

‡ adapted with permission from Monzel *et al.*[87]

presented in section 5.1.2. For simulations in the presence of sol. CXCL12, g_c/κ_2 was reduced to 0.085 to reproduce the minor reduction of $\Gamma_2 + \Gamma_3$. To obtain a reduction of deformability in the presence of NOX-A12 by factor of 3 – 4, g_c/κ_2 was reduced to 0.045 by factor of 2 compared to the control sample, and to 0.055 by factor of 1.6, respectively.

To reach a migration speed $\langle v \rangle$ equivalent to the corresponding values ±10% as reported by Monzel *et al.*,[87] mobility parameter $|\gamma|$ was adjusted for simulations. As a reference, the value of $|\gamma| = 8.05 \pm 1.80$ was used for control samples as obtained and presented in section 5.1.3. In the presence of sol. CXCL12, simulations matching a $\langle v \rangle$ of 0.25 a.u. were reached by adjusting $|\gamma|$ to 8.40 ± 3.30 compared to control samples. To reach a migration speed of $\langle v \rangle = 0.18$ a.u. by simulations in the presence of 50 ng/ml NOX-A12, an increase of $|\gamma|$ by factor of 2.7 to 21.8 ± 7.4 was necessary, due to the significant reduction of deformability $\langle s_2^2 \rangle + \langle s_3^2 \rangle$. For simulations in the presence of 500 ng/ml NOX-A12, matching $\langle v \rangle$ of 0.24 a.u. was obtained by increasing $|\gamma|$ by factor of 2.3 to 18.5 ± 2.8 compared to control samples. Since in the presence of 500 ng/ml NOX the experimentally obtained deformation power was higher than in the presence of 50 ng/ml NOX, mobility $|\gamma|$ exhibited lower values for reaching a similar migration speed.

5.3.2. Discussion

From the qualitative observation of trajectory appearance as well as quantitative analysis of dynamic parameters, the effect of sol. CXCL12 and NOX-A12 on the dynamic behaviour of hHSC on surrogate substrates displaying N-cadherin could be reproduced. In the presence of sol. CXCL12, no significant influence was observed in experiments[87] and simulations regarding deformation power, migration speed, parameter ratio g_c/κ_2, or mobility $|\gamma|$. Considering only net migration distance and migration speed $\langle v \rangle$, also the application of NOX-A12 showed no major impact, as compared to control samples. This is in good agreement with transwell migration assays in the absence of CXCL12, where no statistically significant difference was found for the migration of cells with or without the administration of NOX-A12.[164]

Surprisingly, the application of CXCL12 Spiegelmer NOX-A12 altered the dynamic behaviour of hHSCs even in the absence of CXCL12, indicating a possible interaction with cytoskeletal rearrangements during migration. In the presence

Table 5.7.: Results from simulations considering surrogate substrates displaying N-cadherin at $\langle d \rangle = 18\,\text{nm}$ and the presence of sol. CXCL12 and NOX-A12. Average values in dimensionless units, of $N = 40$ independent simulations each, ± standard deviation.

	control	+ CXCL12	+ NOX-A12$_{50}$	+ NOX-A12$_{500}$
$\langle s_2^2 \rangle + \langle s_3^2 \rangle$	0.031	0.029	0.007	0.011
g_c/κ_2	0.090	0.085	0.045	0.055
$\lvert\gamma\rvert$	8.1 ± 1.8	8.4 ± 3.3	21.8 ± 7.4	18.5 ± 2.8

of NOX-A12, deformation activity was reduced, while migration trajectories were elongated compared to the control group.[87] From the perspective of simulations performed in this chapter, the reduction of deformability $\langle s_2^2 \rangle + \langle s_3^2 \rangle$ and therefore g_c/κ_2 in the presence of NOX-A12 indicates a reduction of intrinsic forces g_c, or enhancement of relaxation rate κ equivalent to a stiffening of the cell. With this distinction of deformation during migration using numerical simulations on previously reported data, the present work provides additional insight into the impact of NOX-A12 in the absence of CXCL12. From the simulations point of view, cell migration is governed by deformation and mobility on the substrate. Since in the presence of NOX-A12 the deformation is reduced, sustainment of migration can only be achieved by an increase in mobility.

While NOX-A12 has been shown to inhibit the interaction between soluble CXCL12 and its receptor CXCR4,[165–171] the direct effect of NOX-A12 on the deformation activity of hHSC in the absence of sol. CXCL12 should be further investigated. Several studies have shown that in parallel to the mobilisation of hHSC, administration of NOX-A12 is followed by an over-expression of CXCL12 receptor CXCR4 on the surface of hHSC.[165,172] Since none of the studies investigated control samples in the absence of CXCL12, the exact cause and effect of increased CXCR4 expression is still to be discussed. An intriguing question to address for future studies would be, for example, if the effect of over-expression of CXCR4 could be related to a change in cell stiffness or cytoskeletal rearrangements, or if the impact of NOX-A12 is connected to an entirely different pathway.

5.4. Summary

In this chapter, adhesion, deformation, and migration of hHSCs in the absence and presence of extrinsic stimulation were presented and analysed, connecting experimental results and numerical simulations. By the optical-microscopy based techniques of micro-interferometry and laser-induced cell detachment, the influence of a clinical drug antagonistic to the substrate functionalisation was determined. Results showed a reduction of fraction of adherent cells as well as adhesion area and adhesion strength. Power spectral analysis of experiments revealed a reduction in total power of deformation upon administration of the clinical agent, as well as the variation of ligand density displayed on the surrogate substrates.

Adjustment of simulation parameters to the corresponding results demonstrated that in fact the ratio between intrinsic force and line tension g_c/κ_2 was altered by the stimulation. Migration analysis resulted in the determination of diffusion constant D and persistence time τ of cell trajectories, which was matched in numerical simulation by adjustment of mobility $|\gamma|$, representing the inverse of the friction between cells and substrate. Seeming contradiction between increased mobility $|\gamma|$ and decreased migration behaviour could be explained by the drastic reduction of deformation activity causing deficient cell propulsion. In order to reach the extension of experimentally determined parameters D and τ, lack of deformation activity was demonstrated to be counteracted by an increase in mobility. This showed the direct influence of stimulation of N-cadherin mediated adhesion, where increase of mobility equivalent to reduction of friction between cell and substrate was caused by blocking or reduction of accessible binding sites.

Furthermore, experimental results reported by Monzel *et al.*[87] were investigated using numerical simulations. Drastic reduction of ratio between intrinsic force and line tension g_c/κ_2 as well as increased mobility $|\gamma|$ caused by NOX-A12 showed that NOX-A12 not only influences the adhesion mediated via CXCL12/CXCR4, but also has an effect on deformation and mobility in the absence of its antagonist CXCL12.

The results presented in this chapter demonstrate, how the combination of quantitative experiments utilising *in vitro* bone marrow micro-environments and the simple model of cell crawling[63] provides insight into the influence of clinical agents and environmental parameters on the static and dynamic behaviour of human primary cells, that were not analysed elsewhere.

6. Conclusions

In this work, electrostatics, mechanics, and dynamics of biological interfaces were quantitatively determined in the absence and presence of external perturbation by the combination of various physical techniques.

In chapter 4, the mechanism how the combination of charged surfactants and alcohol synergistically destroys the electrostatic barrier protecting the surface of bacteria was investigated on molecular level, utilising a model system representing the outer membrane of Gram-negative bacteria prepared at the air-water interface. The disturbance of the membrane's equilibrium state by surface active molecules BzA and BAC was studied within Å resolution using X-ray techniques under synchrotron radiation. In section 4.1, the results from compressibility analysis were presented. In the absence of Ca^{2+}, the addition of BzA caused the reduction of maximum compressional modulus from 120 mN/m to 70 mN/m, 50 mN/m, and 20 mN/m, as well as a decrease of the collapse pressure from 50 mN/m to 40 mN/m, 30 mN/m, and 20 mN/m, with the effect increasing with increasing concentration of BzA. Under the influence of BAC, the reduction of maximum compressional modulus to 30 mN/m was not dependent on concentration. Only the collapse pressure decreased with increasing concentration, to 40 mN/m and 30 mN/m. For the combined presence of both additives, 10 mM BzA with 15 µM BAC showed no difference to the presence of 15 µM BAC alone. The combination of 100 mM BzA with 5 µM BAC, however, caused further reduction of maximum compressional modulus to 20 mN/m, as well as the collapse pressure to 25 mN/m, comparable to the effect of lethal dose of 200 mM BzA alone. In the presence of Ca^{2+}, the observed effect was less pronounced than on Ca^{2+}-free buffer. The addition of BzA caused the reduction of maximum compressional modulus from 200 mN/m to 140 mN/m, 70 mN/m, and 50 mN/m, while the collapse pressure remained at 50 mN/m for the addition of 10 mM BzA, and was further reduced to 40 mN/m and 25 – 30 mN/m with increasing concentration. Under the influence of BAC,

the maximum compressional modulus was reduced to 120 mN/m and 100 mN/m, while the collapse pressure remained at $\sim$ 50 mN/m for both concentrations. For the combined presence of both additives, 10 mM BzA with 15 µM BAC showed no difference to the presence of 15 µM BAC alone. The combination of 100 mM BzA with 5 µM BAC, however, caused further reduction of maximum compressional modulus to 100 mN/m, as well as a decrease of collapse pressure to 35 mN/m, similar to the effect of 15 µM BAC alone, with reduction of the collapse pressure.

Structural changes in the direction perpendicular to the membrane were investigated with sub-Å resolution using specular X-ray reflectivity in sections 4.2 – 4.4. In the absence of Ca^{2+}, the addition of 100 mM BzA caused roughening of the chain-saccharide interface, and the stratified structures of the model membranes were significantly disturbed by exposure to 5 µM BAC. In the presence of Ca^{2+}, 100 mM BzA did not show any major effect, and the pure addition of 5 µM BAC caused only minor reduction of electron density and minor elevation of roughness at both chain and saccharide regions. Remarkably, the addition of a non-lethal concentration of BzA caused a significant increase of roughness between hydrocarbon chains and saccharide headgroups, leading to a disturbance of structural integrity of the LPS membrane and the incorporation of the cationic surfactant.

Finally, the ion concentration profiles of K^+ and Ca^{2+} near the interface were determined with Å resolution using X-ray fluorescence in section 4.5.

While the addition of 100 mM BzA showed no major effect for both subphases, the presence of 5 µM BAC caused significant changes. On Ca^{2+}-free subphase, cationic surfactants penetrated into the membrane core by disturbing the layer of K^+ coupled to the negatively charged saccharide headgroups at z = 6 Å from the chain-saccharide interface, preventing analysis of fluorescence data due to the disturbance of the layered structure. On Ca^{2+}-loaded buffer, addition of pure BAC caused a shift of concentration maximum in the condensed layer of Ca^{2+}-ions from z = 7 Å to z = 3 Å from the chain-saccharide interface, but the full incorporation of BAC into the membrane core was still prevented by the condensed layer of Ca^{2+} ions cross-linking the charged saccharide groups. Remarkably, the addition of a non-lethal concentration of aromatic alcohol caused a significant increase of roughness between hydrocarbon chains and saccharide headgroups, leading to a disturbance of structural integrity of the membrane.

These results demonstrate details about the synergistic effect of cationic surfac-

tant and aromatic alcohol on bacterial outer membranes, which were not investigated in depth before. Furthermore, the usefulness of simultaneous XRR and GIXF measurement was demonstrated for providing element specific information in the vicinity of interfaces, which provides insight into physical mechanisms at complex, biological interfaces such as the synergistic interplay of sanitiser components to achieve a high antibacterial activity.

In chapter 5, the mechanical properties and non-equilibrium dynamics of living cells were quantitatively investigated on substrates precisely mimicking cellular micro-environments. Human haematopoietic stem cells were analysed in cooperation with Prof. A.D. Ho and Prof. C. Müller-Tidow (Internal Medicine V, University Hospital Heidelberg) under the influence of molecules antagonistic to the micro-environment composition, allowing the analysis of direct perturbation to the system's single components. Area of tight cell contact and adhesion strength in the presence and absence of clinical agents were measured by label-free micro-interferometry and a cell-detachment assay, which is based on shockwaves induced by pico-second laser pulses.

The influence of clinical drug ADH-1, antagonistic to N-cadherin, was analysed in section 5.1. As determined by μ-interferometry analysis, the administration of ADH-1 reduced the area of tight adhesion significantly by a factor of 1.8, from $7.4 \pm 3.4\,\mu m^2$ to $4.1 \pm 2.8\,\mu m^2$. Laser-induced cell detachment showed a highly significant reduction of adherent fraction by a factor of 2, from $73 \pm 10\%$ to $37 \pm 11\%$. The adhesion strength was determined to be reduced from $5.1 \pm 2.0\,MPa$ to $3.4 \pm 2.0\,MPa$ by a factor of 1.5 in the presence of ADH-1.

Deformation and migration of hHSCs in the absence and presence of ADH-1 were presented and analysed in sections 5.1.2 and 5.1.3, connecting experimental results and numerical simulations. Dynamics of cells were characterised by power spectral analysis of membrane deformation from live cell imaging data, yielding the energy dissipation due to active deformation. Power spectral analysis of experiments showed that the addition of ADH-1 reduced the total power of deformation significantly by a factor of 2.2, from 0.031 ± 0.025 to 0.014 ± 0.018. Spatio-temporal dynamics of cells were theoretically modelled by adding periodic deformation forces and friction to the Ohta-Okuma model for self-propelled, deformable particles. Adjustment of simulation parameters to those results demonstrated that in the presence of ADH-1, the ratio between intrinsic force and line

tension g_c/κ_2 was reduced by a factor of 1.5. Line tension of mode 2 and 3 deformation was also altered by the presence of ADH-1. To match the experimentally determined increase in deformation power Γ_2 in respect to Γ_3, the ratio between line tension of mode 2 vs. mode 3 κ_3/κ_2 was increased by factor 1.2. Migration analysis resulted in the determination of diffusion constant D and persistence time τ of cell trajectories. In the presence of ADH-1, D was significantly reduced from $0.97 \pm 0.64\,\mu\text{m}^2/\text{min}$ to $0.40 \pm 0.33\,\mu\text{m}^2/\text{min}$ by factor of 2.4, as well as τ from $88 \pm 26\,\text{s}$ to $72 \pm 19\,\text{s}$ by factor of 1.2. In order to match those experimental results in simulated arbitrary units, mobility $|\gamma|$ on the substrate was increased by factor of 1.4 from 8.1 ± 1.8 to 11.1 ± 3.4. This contradiction between decreased migration behaviour and increased mobility could be explained by the drastic reduction of deformation activity causing deficient cell propulsion. In order to reach the extension of experimentally determined parameters D and τ, lack of deformation activity was demonstrated to be counteracted by an increase in mobility. This showed the direct influence of ADH-1 on N-cadherin mediated adhesion, where increase of mobility equivalent to reduction of friction between cell and substrate was caused by blocking of accessible binding sites via ADH-1.

In section 5.2, the results from unpublished experiments regarding deformation and migration of hHSCs on various surface densities of N-cadherin were reconstructed using numerical simulations. To match the decreased deformation power observed in the highest intermolecular distance of N-cadherin ($\langle d \rangle = 47\,\text{nm}$) displayed on surrogate substrates, the ratio between intrinsic force and line tension g_c/κ_2 was reduced by factor of 1.2 compared to control simulations presented on $\langle d \rangle = 18\,\text{nm}$ in section 5.1.2. Migration parameters of D and τ were adjusted in arbitrary simulated unity by choice of mobility $|\gamma|$. To reach the values observed from experiments at highest intermolecular distance of N-cadherin, $|\gamma|$ was increased to 10.0 ± 0.7 by factor 1.2, compared to control simulations presented in section 5.1.3. These results showed the enhanced mobility of hHSCs caused by a reduced number of binding sites via reduced surface density of N-cadherin on surrogate substrates.

Finally, in section 5.3 the theoretical modelling of hHSC dynamics under the influence of NOX-A12 was presented. Following the experimental results published by Monzel *et al.*,[87] simulation parameters were adjusted to match the results for sum of deformation power $\Gamma_2 + \Gamma_3$ and migration velocity v. The reduction of

$\Gamma_2 + \Gamma_3$ by factor of $\sim 2.8 - 4.4$ in the presence of different concentrations of NOX-A12 was reached by reducing parameter ratio g_c/κ_2 by factor $1.6 - 2$ from 0.090 to $0.045 - 0.055$, respectively. Matching the change of migration velocity in arbitrary simulated units led to the increase in mobility $|\gamma|$ by factor $2.3 - 2.6$, from 8.1 to $18.5 - 21.8$. As for the influence of ADH-1, the drastic reduction of deformation caused by NOX-A12 was counteracted by an increase in mobility, showing that the Spiegelmer not only influences the adhesion mediated via CXCL12/CXCR4, but also influences deformation and mobility in the absence of the ligand-receptor pair.

These results demonstrate how the combination of quantitative experiments utilising *in vitro* bone marrow micro-environments and a simple model of cell crawling[63] provides insight into the influence of clinical agents and environmental parameters on the dynamic phenotype of human primary cells. Although the Ohta-Okuma model for self-propelled, deformable particles is not able to include chemical reactions inside the cells, the simulations could describe the deformation and motion of human stem cells in the absence and presence of drugs as modulation of adhesion and active deformation.

A. Appendix I: Characterisation of LPS Ra Monolayers

A.1. Antibacterial Activity of Sanitiser and its Ingredients

Bacterial killing assays were performed by Simone Gierlich, following a slightly modified version of a previously reported protocol.[14,16] Positive control experiments were performed using a commercial sanitiser (Bathmagiclean, Kao Corporation, Tokyo, Japan) to confirm its antimicrobial activity to *Salmonella enterica* (serovar Minnesota) rough mutant R60. As shown in figure A.1 (A), when a 100- µl portion of suspension containing 7×10^6 bacteria was deposited on lysogeny broth (LB) agar, the surface was fully covered with bacterial colonies after an overnight incubation at 37 °C. On the other hand, only 2 colonies survived when 10 times more bacteria were exposed to a 0.1% (v/v) sanitiser for 5 min before seeding (fig. A.1 (B)). The antimicrobial activity of the commercial sanitiser confirmed that the monolayer of LPS Ra is valid as the model to understand how the sanitiser and its ingredients interact with the outer membrane of Gram-negative bacteria.

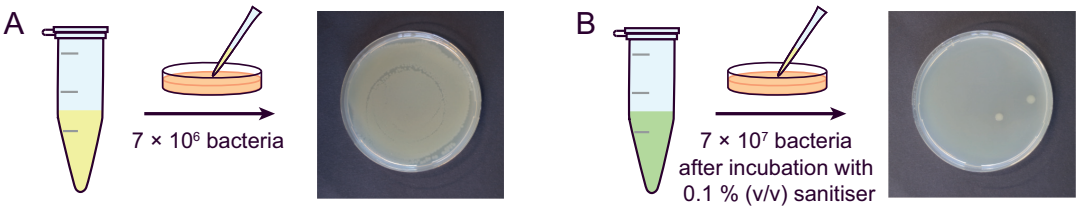

Figure A.1.: Antibacterial activity of a commercial sanitiser against *Salmonella enterica*. **(A)** Control suspension containing 7×10^6 bacteria deposited on LB agar, showing full surface coverage. **(B)** When 10 times more bacteria were exposed to 0.1% (v/v) sanitiser, only 2 colonies survived.

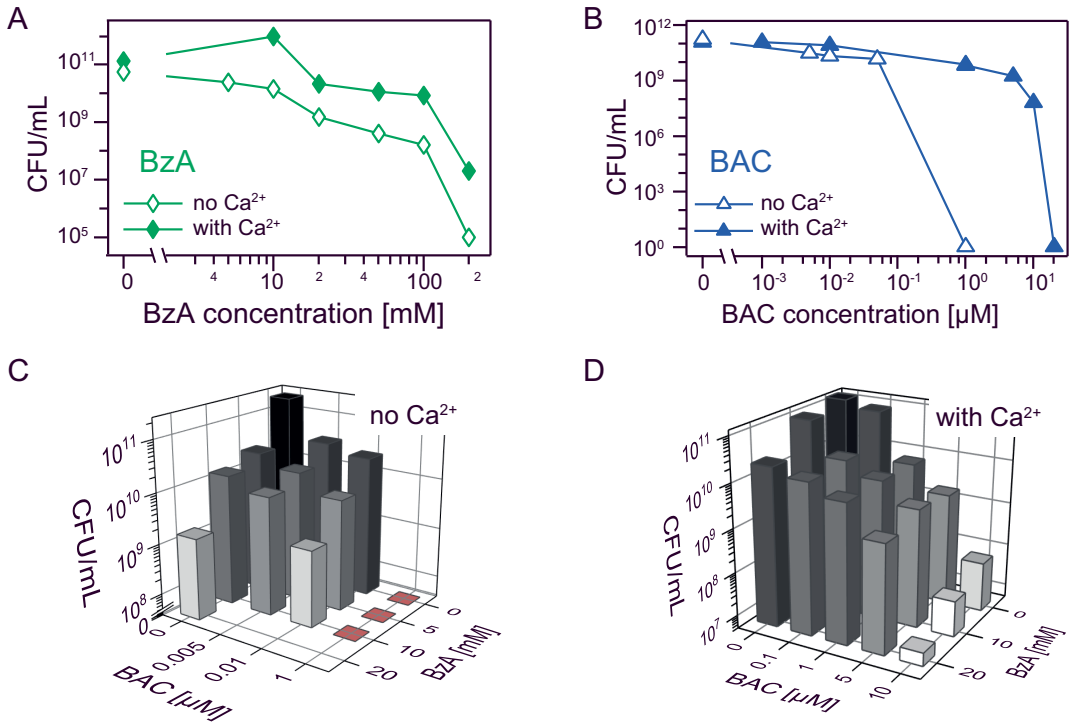

Figure A.2.: Influence of concentrations of additives on the normalised colony forming unit (CFU/ml) of *Salmonella enterica* (serovar Minnesota) rough mutant. Influence of **(A)** benzyl alcohol (BzA) and **(B)** benzalkonium chloride (BAC) on Ca^{2+}-free (open symbols) and Ca^{2+}-loaded (solid symbols) buffers. Note the difference in the scale of the x-axis. Synergistic effect of BAC and BzA in killing *Salmonella enterica* in **(C)** Ca^{2+}-free and **(D)** Ca^{2+}-loaded buffer. Adapted from Thoma *et al.*[16]

In order to understand how each ingredient individually contributes to the killing of bacteria, the same experiment was performed under the exposure to solutions of either aromatic alcohol (BzA) or the cationic surfactant (BAC) at different concentrations, dissolved in Ca^{2+}-free and Ca^{2+}-loaded buffers. Figure A.2 (A) shows CFU/ml of *Salmonella enterica* after 5 min exposure to BzA solutions of various concentrations in the absence and presence of Ca^{2+} ions. Compared to the control experiment at 0 mM BzA, the CFU/ml levels decreased but remained high at $c_{\mathrm{BzA}} = 100\,\mathrm{mM}$. Moreover, experiments in Ca^{2+}-loaded buffer (solid symbols) showed higher CFU/ml levels than under Ca^{2+}-free condition (open symbols) at all BzA concentrations, indicating the protective function of Ca^{2+} ions. All bacteria in Ca^{2+}-free buffer died at $c_{\mathrm{BzA}} = 200\,\mathrm{mM}$, while those in Ca^{2+}-loaded condition still survived with $\sim 10^7$ CFU/ml. Figure A.2 (B) presents CFU/ml of *Salmonella*

enterica after a 5 min exposure to solutions with different BAC concentrations in the absence and presence of Ca^{2+} ions. Compared to BzA, all bacteria were killed at $c_{BAC} = 1\,\mu M$ under Ca^{2+}-free condition (open symbols), while for BzA *Salmonella enterica* could withstand even 10^5 times higher doses (fig. A.2 (A)). Remarkably, in Ca^{2+}-loaded buffer (solid symbols), colony forming units still remained high for this concentration of BAC ($\sim 10^{10}$ CFU/ml). In the presence of Ca^{2+} ions, the BAC concentration necessary for killing all bacteria was more than one order of magnitude higher ($c_{BAC} = 20\,\mu M$). The obtained results suggest the critical role of cationic surfactant (BAC) in bacteria killing and the protective function of Ca^{2+} ions.

The next condition addressed was the combination of both BzA and BAC present in sanitisers. The synergistic effect of both additives was examined in Ca^{2+}-free (A.2 (C)) and Ca^{2+}-loaded (A.2 (D)) condition, which showed that the CFU/ml level exhibited a clear decrease by adding BzA. Even in the presence of Ca^{2+}, the complete killing of *Salmonella enterica* was achieved at additive concentrations of $c_{BAC} = 10\,\mu M$ and $c_{BzA} = 20\,mM$. As these values are distinctly lower than the individual lethal concentrations of BAC or BzA, $c_{BAC} = 20\,\mu M$ and $c_{BzA} = 200\,mM$, respectively, this data confirmed that the combination of cationic surfactant and aromatic alcohol indeed facilitates bacteria killing.

A.2. Pressure-Area Isotherms

Pressure-area isotherms were measured excluding the offset level between blank subphases containing the additive and pure water. Isotherm data including this offset are presented in figure A.3 (A) and (D) for Ca^{2+}-free and Ca^{2+}-loaded conditions, respectively. Control (black), 100 mM BzA (green), 5 µM BAC (blue), and 100 mM BzA + 5 µM BAC (red) measurements are shown including the offset, confirming that the area per molecule near the collapse converges with that of the intact LPS Ra monolayer. Offset levels of blank subphases were observed as surface pressures of $\pi_{BzA} = 15\,mN/m$ for 100 mM BzA, $\pi_{BAC} = 4\,mN/m$ for 5 µM BAC, and $\pi_{BzA\,+\,BAC} = 20\,mN/m$ for 100 mM BzA + 5 µM BAC.

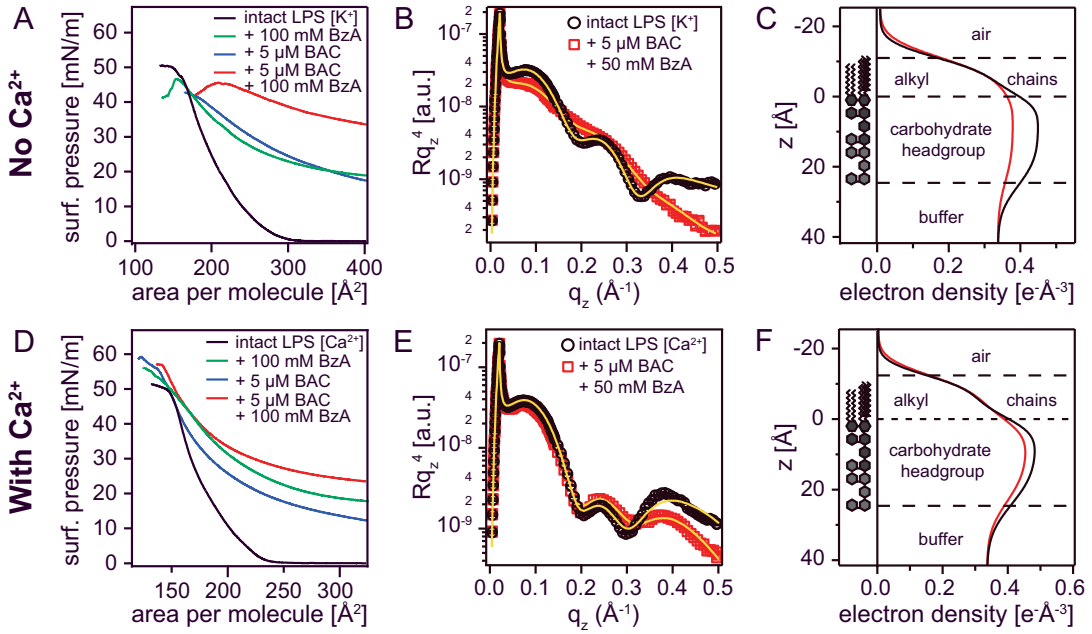

Figure A.3.: Pressure-area isotherms including offset of blank subphases, and synergistic influence of BzA and BAC on LPS Ra monolayers in the absence and presence of Ca^{2+} ions. Isotherm measurement on **(A)** Ca^{2+}-free and **(D)** Ca^{2+}-loaded conditions for control (black) and in the presence of 100 mM BzA (green), 5 µM BAC (blue), and 100 mM BzA + 5 µM BAC (red). XRR data **(B)** and reconstructed electron density profiles **(C)** of LPS Ra monolayers in the absence (black) and presence (red) of 50 mM BzA + 5 µM BAC, measured on Ca^{2+}-free subphase. XRR data **(E)** and reconstructed electron density profiles **(F)** in the absence (black) and presence (red) of 50 mM BzA + 5 µM BAC, measured on Ca^{2+}-loaded subphase.

A.3. Additional Condition in XRR

As a reference, XRR measurement of 50 mM BzA + 5 µM BAC is presented in figure A.3 (B) and (E) on Ca^{2+}-free and Ca^{2+}-loaded condition, with corresponding reconstructed electron density profiles in panels (C) and (F). While in the absence of Ca^{2+} the disturbance of the layered structure can be seen by the loss of periodic oscillations in the XRR data, the integrity of the stratified layers under Ca^{2+}-loaded condition is clearly indicated by the intact profile of the XRR data.

B. Appendix II: Glossary on Mathematical Symbols

B.1. X-Ray Reflectivity and Micro-Interferometry

Table B.1.: Mathematical symbols used for calculations of X-ray reflectivity and μ-interferometry in sections 2.1 and 2.3

α^+, α_0^+	incident angle, relative to the surface
α_{sc}, α_0^-	scattered angle, relative to the surface
α_t	complex transmission angle, relative to the surface
α_c	critical angle for total reflection, relative to the surface
β, β_j	imaginary part of n_j, absorption
δ, δ_j	real part of n_j, dispersion
$\delta_\pm$	phase change between layers
Δ_i, Δ_{const}, Δ_{dest}	optical path difference arising from layer i, for constructive and destructive interference
θ_r, θ_i^-	angle of reflection in μ-interferometry, relative to the surface normal
θ_t, θ_{i+1}^+	angle of transmission in μ-interferometry, relative to the surface normal
Λ	penetration depth
μ	attenuation coefficient
ρ	electron density
σ_j	root-mean-square (rms) roughness of layer j
φ_i	phase shift between incident and reflected wave

d_j	thickness of layer j
$\boldsymbol{E}_0^+$	incident wave
E_0^+	amplitude of incident wave
E^-, $E_{(j)}^-$, $E_{(j,k)}^-$, $E^-(z)$	amplitude of reflected wave propagating in layer j and reflected from interface to layer k, at depth z
E_0^-	amplitude of reflected wave propagating in layer $j = 0$
$\boldsymbol{E}_t^+$	transmitted wave
E_t^+, $E_{(j)}^+$, $E^+(z)$	amplitude of transmitted wave propagating in layer j, at depth z in the sample
I_{tot}	total reflected intensity in µ-interferometry
$\hat{I}$	normalised intensity in µ-interferometry
$\boldsymbol{k}^+$, $\boldsymbol{k}_0^+$	incident wavevector
k_0^+	magnitude of incident wavevector
$\boldsymbol{k}_{sc}$	scattered wavevector
$\boldsymbol{k}^-$	reflected wavevector
k^-, $k_{(j,k)}^-$	magnitude of reflected wavevector
$\boldsymbol{k}_t^+$	transmitted wavevector
k_t^+, $k_{(j)}^+$	magnitude of transmitted wavevector
$\hat{k}$	z-component k_z of wavevector $\boldsymbol{k}$
n, n_j	refractive index of layer j
$\boldsymbol{P}_{(j,j+1)}$	propagation matrix between adjacent layers j and $j+1$
$\boldsymbol{q}$	wavevector transfer
q_c	wavevector transfer for critical angle of total reflection
q_z	z-component of wavevector transfer
r_e	classical electron radius
$r^\perp$	reflection coefficient for s-polarised wave
$r_{(j,j+1)}$	reflection coefficient for interface between layers $(j, j+1)$
$\tilde{r}_{(j,j+1)}$	modified reflection coefficient between layers $(j, j+1)$
R_F	Fresnel reflectivity
$t^\perp$	transmission coefficient for s-polarised wave
$t_{(j,j+1)}$	transmission coefficient for interface between layers $(j, j+1)$
$\tilde{t}_{(j,j+1)}$	modified transmission coefficient between layers $(j, j+1)$
z, z_j	z-position in layer j

B.2. Deformation Analysis and Numerical Simulations

Table B.2.: Mathematical symbols used to describe cell deformation in experiments and simulations in section 2.5 – 2.7

	experiments		simulations
α	polar angle to describe the cell radius	α	polar angle to describe the cell radius
Γ_m	deformation power of mode m	$\langle s_n^2 \rangle$	deformability of mode n, equivalent to Γ_m
c_m	Fourier coefficients	c_n	Fourier coefficients
$r(\alpha, t)$	cell radius	$R(\alpha, t)$	cell radius
r_0	average cell radius	R_0	average cell radius
$\delta r(\alpha, t)$	normalised shape deviations	$\delta R(\alpha, t)$	normalised shape deviations
$\delta r_m(\alpha, t)$	Fourier expansion of shape deviations	$\delta R_n(\alpha, t)$	Fourier expansion of shape deviations
m	mode of deformation	n	simulated mode of deformation

Table B.3.: Mathematical symbols used for simulations in section 2.7

γ, $\lvert\gamma\rvert$	mobility parameter
δ_{ij}	Kronecker delta
ζ	general noise term, $\zeta \in [\xi_n, \eta_n]$
η_n	noise on direction of intrinsic force $F^{(n)}$
θ	direction of migration velocity
θ_n	orientation of deformation of mode n
θ_{23}	angle between θ_2 and θ_3

$\Theta^{(n)}$	phase of intrinsic force $F^{(n)}$
κ, κ_n	relaxation rate of mode n
ξ_n	noise on amplitude of intrinsic force $F^{(n)}$
Φ	phase shift between oscillations of mode 2 and mode 3 deformation force amplitudes
Ψ_v	phase defining migration to follow broader end of particle
b_0	non-linear coupling parameter for mode 2 deformation
d_0	non-linear coupling parameter for mode 3 deformation
D_ζ	amplitude of Gaussian noise ζ, with $\zeta \in [\xi_n, \eta_n]$
$F^{(n)}$	intrinsic force of mode n
$g^{(n)}$	time-dependent amplitude of intrinsic force of mode n
$g_c^{(n)}$	offset of intrinsic force amplitude
$g_0^{(n)}$	amplitude of intrinsic force oscillations
G_i	random uniform distribution for discrete definition of noise
s_n	amplitude of deformation of mode n
S_{ij}	2^{nd} rank deformation tensor
T	time period of oscillatory deformation forces
U_{ijk}	3^{rd} rank deformation tensor
$\boldsymbol{v}$	migration velocity
v_k	migration velocity component k
$\|v\|$	amplitude of migration velocity

C. Appendix III: Abbreviations

ACF	Auto-correlation function
ADH-1	Exherin
AML	Acute myeloid leukaemia
BAC	Benzalkoniumchloride
BM	Bone marrow
BzA	Benzyl alcohol
CAM	Cell adhesion molecule
CDH2	N-cadherin
CLL	Chronic lymphocytic leukaemia
CXCL12	C-X-C motif chemokine 12, also known as SDF-1α
CXCR4	C-X-C chemokine receptor type 4, also known as CD184
EMT	Epithelial-to-mesenchymal transition
FT	Fourier transform
FWHM	Full width at half maximum
GIXF	Grazing incidence X-ray fluorescence
HBS	HEPES, 4-(2-hydroxyethyl)-1-piperazineethanesulfonic acid
HSC, hHSC	Human haematopoietic stem cell
LPS	Lipopolysaccharide
MM	Multiple myeloma
MSA	Mean squared-amplitude
MSD	Mean squared-displacement
NOX-A12	Olaptesed pegol, Noxxon Pharma
PB	Peripheral blood
PDMS	Polydimethylsiloxane
SDF-1α	Stromal cell-derived factor 1α, also known as CXCL12
XRR	X-ray reflectivity

D. Publications

Included in this thesis

1. **J. Thoma**[†], W. Abuillan[†], I. Furikado, T. Habe, A. Yamamoto, S. Gierlich, ... & M. Tanaka. Specific localisation of ions in bacterial membranes unravels physical mechanism of effective bacteria killing by sanitiser. *Scientific reports*, 10(1), 1-12, 2020.

Not included in this thesis

1. L. He, C. Arnold, **J. Thoma**, C. Rohde, M. Kholmatov, S. Garg1, ... & C. Pabst. CDK7/12/13 inhibition targets an oscillatingleukemia stem cell network and synergizes with venetoclax in acute myeloid leukaemia. *EMBO Molecular Medicine*, e14990, 2022.

2. L. Poisa-Beiro[†], **J. Thoma**[†], J. Landry, S. Sauer, A. Yamamoto, V. Eckstein, ... & A. D. Ho. Glycogen accumulation, central carbon metabolism, and aging of hematopoietic stem and progenitor cells. *Scientific reports*, 10(1), 1-11, 2020.

3. M. Lamas-Murua, B. Stolp, S. Kaw, **J. Thoma**, N. Tsopoulidis, B. Trautz, ... & O. T. Fackler. HIV-1 Nef disrupts $CD4^+$ T lymphocyte polarity, extravasation, and homing to lymph nodes via its Nef-associated kinase complex interface. *The Journal of Immunology*, 201(9), 2731-2743, 2018.

[†] authors contributed equally

Bibliography

[1] PA Monnard and DW. Deamer. Membrane self-assembly processes: Steps toward the first cellular life. *The Anatomical Record*, 268(3):196–207, 2002.

[2] E Sackmann. Chapter 1 Biological Membranes Architecture and Function. In *Handbook of Biological Physics*, volume 1, pages 1–62. Elsevier Science, 1995.

[3] Anonymous Authors. *http://2012books.lardbucket.org/books/introduction-to-chemistry-general-organic-and-biological/s20-03-membranes-and-membrane-lipids.html.* Free since 2013 by Creative Commons by-nc-sa 3.0 license.

[4] Franck Duong, Jerry Eichler, Albert Price, Marilyn Rice Leonard, and William Wickner. Biogenesis of the gram-negative bacterial envelope. *Cell*, 91(5):567–573, 1997.

[5] Rafael G Oliveira, Emanuel Schneck, Bonnie E Quinn, Oleg V Konovalov, Klaus Brandenburg, Ulrich Seydel, Tom Gill, Charles B Hanna, David A Pink, and Motomu Tanaka. Physical mechanisms of bacterial survival revealed by combined grazing-incidence x-ray scattering and monte carlo simulation. *Comptes Rendus Chimie*, 12(1-2):209–217, 2009.

[6] Rafael G Oliveira, Emanuel Schneck, Bonnie E Quinn, Oleg V Konovalov, Klaus Brandenburg, Thomas Gutsmann, Tom Gill, Charles B Hanna, David A Pink, and Motomu Tanaka. Crucial roles of charged saccharide moieties in survival of gram negative bacteria against protamine revealed by combination of grazing incidence x-ray structural characterizations and monte carlo simulations. *Physical Review E*, 81(4):041901, 2010.

[7] Emanuel Schneck, Thomas Schubert, Oleg V Konovalov, Bonnie E Quinn, Thomas Gutsmann, Klaus Brandenburg, Rafael G Oliveira, David A Pink,

and Motomu Tanaka. Quantitative determination of ion distributions in bacterial lipopolysaccharide membranes by grazing-incidence x-ray fluorescence. *Proceedings of the National Academy of Sciences*, 107(20):9147–9151, 2010.

[8] Wasim Abuillan, Emanuel Schneck, Alexander Körner, Klaus Brandenburg, Thomas Gutsmann, Tom Gill, Alexei Vorobiev, Oleg Konovalov, and Motomu Tanaka. Physical interactions of fish protamine and antisepsis peptide drugs with bacterial membranes revealed by combination of specular x-ray reflectivity and grazing-incidence x-ray fluorescence. *Physical Review E - Statistical, Nonlinear, and Soft Matter Physics*, 88(1):12705, 2013.

[9] DA Pink, L Truelstrup Hansen, Tom A Gill, Bonnie E Quinn, MH Jericho, and TJ Beveridge. Divalent calcium ions inhibit the penetration of protamine through the polysaccharide brush of the outer membrane of gram-negative bacteria. *Langmuir*, 19(21):8852–8858, 2003.

[10] Moritz Herrmann, Emanuel Schneck, Thomas Gutsmann, Klaus Brandenburg, and Motomu Tanaka. Bacterial lipopolysaccharides form physically cross-linked, two-dimensional gels in the presence of divalent cations. *Soft Matter*, 11(30):6037–6044, jul 2015.

[11] Peter Gilbert and LE Moore. Cationic antiseptics: diversity of action under a common epithet. *Journal of applied microbiology*, 99(4):703–715, 2005.

[12] Daniel K Brannan. *Cosmetic microbiology: a practical handbook*. CRC Press, 1997.

[13] Christopher J Ioannou, Geoff W Hanlon, and Stephen P Denyer. Action of disinfectant quaternary ammonium compounds against staphylococcus aureus. *Antimicrobial agents and chemotherapy*, 51(1):296–306, 2007.

[14] Takehisa Yano, Yoshiko Miyahara, Noriyuki Morii, Tetsuya Okano, and Hiromi Kubota. Pentanol and benzyl alcohol attack bacterial surface structures differently. *Applied and environmental microbiology*, 82(1):402–408, 2016.

[15] Takehisa Yano, Hiromi Kubota, Junya Hanai, Jun Hitomi, and Hajime Tokuda. Stress tolerance of methylobacterium biofilms in bathrooms. *Microbes and Environments*, page ME12146, 2012.

[16] Judith Thoma, Wasim Abuillan, Ippei Furikado, Taichi Habe, Akihisa Yamamoto, Simone Gierlich, Stefan Kaufmann, Klaus Brandenburg, Thomas Gutsmann, Oleg Konovalov, Shigeto Inoue, and Motomu Tanaka. Specific localisation of ions in bacterial membranes unravels physical mechanism of effective bacteria killing by sanitiser. *Scientific Reports*, 10(1), dec 2020.

[17] Ivo Konopásek, Kazimierz Strzalka, and Jaroslava Svobodová. Cold shock in bacillus subtilis: different effects of benzyl alcohol and ethanol on the membrane organisation and cell adaptation. *Biochimica Et Biophysica Acta (BBA)-Biomembranes*, 1464(1):18–26, 2000.

[18] Pavel Jungwirth and Paul S Cremer. Beyond hofmeister. *Nature chemistry*, 6(4):261–263, 2014.

[19] Bruce C Gibb. Hofmeister's curse. *Nature chemistry*, 11:963–965, 2019.

[20] Denise J. Montell. Morphogenetic cell movements: Diversity from modular mechanical properties. *Science*, 322(5907):1502–1505, 2008.

[21] S. F. Gilbert. *Developmental Biology, Morphogenesis and Cell Adhesion.* Sinauer Associates, Sunderland (MA), 6th edition, 2000. Available from: https://www.ncbi.nlm.nih.gov/books/NBK10021/.

[22] Alexandra S. Burk, Cornelia Monzel, Hiroshi Y. Yoshikawa, Patrick Wuchter, Rainer Saffrich, Volker Eckstein, Motomu Tanaka, and Anthony D. Ho. Quantifying Adhesion Mechanisms and Dynamics of Human Hematopoietic Stem and Progenitor Cells. *Scientific Reports*, 5:1–11, 2015.

[23] James HC Wang and Jeen-Shang Lin. Cell traction force and measurement methods. *Biomechanics and modeling in mechanobiology*, 6(6):361–371, 2007.

[24] Xavier Trepat, Michael R Wasserman, Thomas E Angelini, Emil Millet, David A Weitz, James P Butler, and Jeffrey J Fredberg. Physical forces during collective cell migration. *Nature physics*, 5(6):426–430, 2009.

[25] Jens Als-Nielsen and Des McMorrow. *Elements of Modern X-ray Physics.* John Wiley & Sons, Ltd, second edition, 2011.

[26] C. Lo Celso, H. E. Fleming, J. W. Wu, C. X. Zhao, S. Miake-Lye, J. Fujisaki, D. Côté, D. W. Rowe, C. P. Lin, and D. T. Scadden. Live-animal tracking of individual haematopoietic stem/progenitor cells in their niche. *Nature*, 457(7225):92–96, 2009.

[27] A. Wilson and A. Trumpp. Bone-marrow haematopoietic-stem-cell niches. *Nature Reviews Immunology*, 6(2):93–106, 2006.

[28] B. D. MacArthur, A. Ma'ayan, and I. R. Lemischka. Systems biology of stem cell fate and cellular reprogramming. *Nature reviews Molecular cell biology*, 10(10):672–681, 2009.

[29] K. A. Moore and I. R. Lemischka. Stem cells and their niches. *Science*, 311(5769):1880–1885, 2006.

[30] Bob Lowenberg, James R Downing, and Alan Burnett. Acute myeloid leukemia. *New England Journal of Medicine*, 341(14):1051–1062, 1999.

[31] Fumihiko Ishikawa, Shuro Yoshida, Yoriko Saito, Atsushi Hijikata, Hiroshi Kitamura, Satoshi Tanaka, Ryu Nakamura, Toru Tanaka, Hiroko Tomiyama, Noriyuki Saito, et al. Chemotherapy-resistant human aml stem cells home to and engraft within the bone-marrow endosteal region. *Nature biotechnology*, 25(11):1315–1321, 2007.

[32] Steven W Lane, David T Scadden, and D Gary Gilliland. The leukemic stem cell niche: current concepts and therapeutic opportunities. *Blood, The Journal of the American Society of Hematology*, 114(6):1150–1157, 2009.

[33] T. M. Dexter and M. A.S. Moore. In vitro duplication and 'cure' of haemopoietic defects in genetically anaemic mice. *Nature*, 269(5627):412–414, 1977.

[34] Olga Schmal, Jan Seifert, Tilman E. Schäffer, Christina B. Walter, Wilhelm K. Aicher, and Gerd Klein. Hematopoietic stem and progenitor cell expansion in contact with mesenchymal stromal cells in a hanging drop model uncovers disadvantages of 3D culture. *Stem Cells International*, 2016, 2016.

[35] M Tanaka and E Sackmann. Polymer-supported membranes as models of the cell surface. *Nature*, 437(7059):656–663, 2005.

[36] Jennifer M Halbleib and W James Nelson. Cadherins in development: Cell adhesion, sorting, and tissue morphogenesis, 2006.

[37] S. Puch, S. Armeanu, C. Kibler, K. R. Johnson, C. A. Muller, M. J. Wheelock, and G. Klein. N-cadherin is developmentally regulated and functionally involved in early hematopoietic cell differentiation. *Journal of cell science*, 114(8):1567–1577, 2001.

[38] L. M. Calvi, G. B. Adams, K. W. Weibrecht, J. M. Weber, D. P. Olson, M. C. Knight, R. P. Martin, E. Schipani, P. Divieti, F. R. Bringhurst, et al. Osteoblastic cells regulate the haematopoietic stem cell niche. *Nature*, 425(6960):841–846, 2003.

[39] F. Wein, L. Pietsch, R. Saffrich, P. Wuchter, T. Walenda, S. Bork, P. Horn, A. Diehlmann, V. Eckstein, A. D. Ho, et al. N-cadherin is expressed on human hematopoietic progenitor cells and mediates interaction with human mesenchymal stromal cells. *Stem cell research*, 4(2):129–139, 2010.

[40] J. Zhang, C. Niu, L. Ye, H. Huang, X. He, W.-G. Tong, J. Ross, J. Haug, T. Johnson, J. Q. Feng, et al. Identification of the haematopoietic stem cell niche and control of the niche size. *Nature*, 425(6960):836–841, 2003.

[41] Porntula Panorchan, Melissa S. Thompson, Kelly J. Davis, Yiider Tseng, Konstantinos Konstantopoulos, and Denis Wirtz. Single-molecule analysis of cadherin-mediated cell-cell adhesion. *Journal of Cell Science*, 119(1):66–74, jan 2006.

[42] Jean Paul Thiery, Hervé Acloque, Ruby Y.J. Huang, and M. Angela Nieto. Epithelial-Mesenchymal Transitions in Development and Disease, nov 2009.

[43] Zhaoming Guo, Kun Zheng, Zhenquan Tan, Ye Liu, Ziyin Zhao, Guang Zhu, Kun Ma, Changhao Cui, Li Wang, and Tianyu Kang. Overcoming drug resistance with functional mesoporous titanium dioxide nanoparticles combining targeting, drug delivery and photodynamic therapy. *Journal of Materials Chemistry B*, 6(46):7750–7759, 2018.

[44] Zhaoming Guo, Wenqing Li, Yue Yuan, Kun Zheng, Yu Tang, Kun Ma, Changhao Cui, Li Wang, Bing He, and Qiang Zhang. Improvement of

chemosensitivity and inhibition of migration via targeting tumor epithelial-to-mesenchymal transition cells by ADH-1-modified liposomes. *Drug Delivery*, 25(1):112–121, 2018.

[45] Noam Erez, Eli Zamir, Barbara J. Gour, Orest W. Blaschuk, and Benjamin Geiger. Induction of apoptosis in cultured endothelial cells by a cadherin antagonist peptide: Involvement of fibroblast growth factor receptor-mediated signalling. *Experimental Cell Research*, 294(2):366–378, 2004.

[46] Cornelia Monzel, Susanne F Fenz, Rudolf Merkel, and Kheya Sengupta. Probing biomembrane dynamics by dual-wavelength reflection interference contrast microscopy. *ChemPhysChem*, 10(16):2828–2838, 2009.

[47] E Evans, K Ritchie, and R Merkel. Sensitive force technique to probe molecular adhesion and structural linkages at biological interfaces. *Biophysical journal*, 68(6):2580–2587, 1995.

[48] Scott E Chesla, Periasamy Selvaraj, and Cheng Zhu. Measuring two-dimensional receptor-ligand binding kinetics by micropipette. *Biophysical journal*, 75(3):1553–1572, 1998.

[49] Amelia Ahmad Khalili and Mohd Ridzuan Ahmad. A review of cell adhesion studies for biomedical and biological applications. *International journal of molecular sciences*, 16(8):18149–18184, 2015.

[50] Jin-Yu Shao and Robert M Hochmuth. Micropipette suction for measuring piconewton forces of adhesion and tether formation from neutrophil membranes. *Biophysical journal*, 71(5):2892–2901, 1996.

[51] Robert M Hochmuth. Micropipette aspiration of living cells. *Journal of biomechanics*, 33(1):15–22, 2000.

[52] JP Mills, M Diez-Silva, DJ Quinn, M Dao, MJ Lang, KSW Tan, CT Lim, G Milon, PH David, O Mercereau-Puijalon, et al. Effect of plasmodial resa protein on deformability of human red blood cells harboring plasmodium falciparum. *Proceedings of the National Academy of Sciences*, 104(22):9213–9217, 2007.

[53] Ming Dao, Chwee Teck Lim, and Subra Suresh. Mechanics of the human red blood cell deformed by optical tweezers. *Journal of the Mechanics and Physics of Solids*, 51(11-12):2259–2280, 2003.

[54] Nadine Walter, Christine Selhuber, Horst Kessler, and Joachim P Spatz. Cellular unbinding forces of initial adhesion processes on nanopatterned surfaces probed with magnetic tweezers. *Nano letters*, 6(3):398–402, 2006.

[55] Keir C Neuman and Attila Nagy. Single-molecule force spectroscopy: optical tweezers, magnetic tweezers and atomic force microscopy. *Nature methods*, 5(6):491–505, 2008.

[56] G Sagvolden, I Giaever, EO Pettersen, and J Feder. Cell adhesion force microscopy. *Proceedings of the National Academy of Sciences*, 96(2):471–476, 1999.

[57] Gerd Binnig, Calvin F Quate, and Ch Gerber. Atomic force microscope. *Physical review letters*, 56(9):930, 1986.

[58] Martin Benoit, Daniela Gabriel, Günther Gerisch, and Hermann E Gaub. Discrete interactions in cell adhesion measured by single-molecule force spectroscopy. *Nature cell biology*, 2(6):313–317, 2000.

[59] Pierre-Henri Puech, Kate Poole, Detlef Knebel, and Daniel J Muller. A new technical approach to quantify cell–cell adhesion forces by afm. *Ultramicroscopy*, 106(8-9):637–644, 2006.

[60] Hiroshi Y. Yoshikawa, Fernanda F. Rossetti, Stefan Kaufmann, Thomas Kaindl, Jeppe Madsen, Ulrike Engel, Andrew L. Lewis, Steven P. Armes, and Motomu Tanaka. Quantitative evaluation of mechanosensing of cells on dynamically tunable hydrogels. *Journal of the American Chemical Society*, 133(5):1367–1374, 2011.

[61] Frank Entschladen, Theodore L Drell IV, Kerstin Lang, Kai Masur, Daniel Palm, Philipp Bastian, Bernd Niggemann, and Kurt S Zaenker. Analysis methods of human cell migration. *Experimental cell research*, 307(2):418–426, 2005.

[62] Takao Ohta and Takahiro Ohkuma. Deformable self-propelled particles. *Physical Review Letters*, 102(15):1–4, 2009.

[63] T. Ohta, M. Tarama, and M. Sano. Simple model of cell crawling. *Physica D: Nonlinear Phenomena*, 318-319:3–11, 2016.

[64] T. Ohta. Dynamics of deformable active particles. *Journal of the Physical Society of Japan*, 86(7):1–20, 2017.

[65] Falko Ziebert, Sumanth Swaminathan, and Igor S. Aranson. Model for self-polarization and motility of keratocyte fragments. *Journal of The Royal Society Interface*, 9(70):1084–1092, may 2012.

[66] M.-F. Carlier and D. Pantaloni. Control of actin assembly dynamics in cell motility. *Journal of Biological Chemistry*, 282(32):23005–23009, 2007.

[67] T. D. Pollard, L. Blanchoin, and R. D. Mullins. Molecular mechanisms controlling actin filament dynamics in nonmuscle cells. *Annu Rev Biophys Biomol Struct*, 29:545–576, 2000.

[68] R. Zaidel-Bar, M. Cohen, L. Addadi, and B. Geiger. Hierarchical assembly of cell–matrix adhesion complexes. *Biochemical Society Transactions*, 32(3):416–420, 2004.

[69] M. A. Stolarska, Y. Kim, and H. G. Othmer. Multi-scale models of cell and tissue dynamics. *Philosophical Transactions of the Royal Society A: Mathematical, Physical and Engineering Sciences*, 367(1902):3525–3553, 2009.

[70] K. Kruse, J. F. Joanny, F. Jülicher, and J. Prost. Contractility and retrograde flow in lamellipodium motion. *Physical biology*, 3(2):130, 2006.

[71] K. Doubrovinski and K. Kruse. Self-organization of treadmilling filaments. *Physical review letters*, 99(22):228104, 2007.

[72] J. M. Oliver, J. R. King, K. J. McKinlay, P. D. Brown, D. M. Grant, C. A. Scotchford, and J. V. Wood. Thin-film theories for two-phase reactive flow models of active cell motion. *Mathematical medicine and biology: a journal of the IMA*, 22(1):53–98, 2005.

[73] P. A. DiMilla, K. Barbee, and D. A. Lauffenburger. Mathematical model for the effects of adhesion and mechanics on cell migration speed. *Biophysical Journal*, 60(1):15–37, 1991.

[74] P. A. DiMilla. Adhesion and traction forces in migration: insights from mathematical models and experiments. In *Biomechanics of Active Movement and Division of Cells*, pages 329–368. Springer, 1994.

[75] K. Kruse, J. F. Joanny, F. Jülicher, and J. Prost. Contractility and retrograde flow in lamellipodium motion. *Physical Biology*, 3(2):130–137, 2006.

[76] D. Shao, W. J. Rappel, and H. Levine. Computational model for cell morphodynamics. *Physical Review Letters*, 105(10):2–5, 2010.

[77] Julien Kockelkoren, Herbert Levine, and Wouter-Jan Rappel. Computational approach for modeling intra-and extracellular dynamics. *Physical Review E*, 68(3):037702, 2003.

[78] Joseph B Collins and Herbert Levine. Diffuse interface model of diffusion-limited crystal growth. *Physical Review B*, 31(9):6119, 1985.

[79] Kinneret Keren, Zachary Pincus, Greg M. Allen, Erin L. Barnhart, Gerard Marriott, Alex Mogilner, and Julie A. Theriot. Mechanism of shape determination in motile cells. *Nature*, 453(7194):475–480, 2008.

[80] Alexander B Verkhovsky, Tatyana M Svitkina, and Gary G Borisy. Self-polarization and directional motility of cytoplasm. *Current Biology*, 9(1):11–S1, 1999.

[81] Maxime F Fournier, Roger Sauser, Davide Ambrosi, Jean-Jacques Meister, and Alexander B Verkhovsky. Force transmission in migrating cells. *Journal of Cell Biology*, 188(2):287–297, 2010.

[82] Pascal Vallotton, Gaudenz Danuser, Sophie Bohnet, Jean-Jacques Meister, and Alexander B Verkhovsky. Tracking retrograde flow in keratocytes: news from the front. *Molecular biology of the cell*, 16(3):1223–1231, 2005.

[83] Falko Ziebert and Igor S. Aranson. Effects of Adhesion Dynamics and Substrate Compliance on the Shape and Motility of Crawling Cells. *PLoS ONE*, 8(5):1–13, 2013.

[84] Tetsuya Hiraiwa. Two types of exclusion interactions for self-propelled objects and collective motion induced by their combination. *Physical Review E*, 99(1):012614, jan 2019.

[85] Tetsuya Hiraiwa. Dynamic Self-Organization of Idealized Migrating Cells by Contact Communication. *Physical Review Letters*, 125(26):268104, 2020.

[86] Takao Ohta, Cornelia Monzel, Alexandra S. Becker, Anthony D. Ho, and Motomu Tanaka. Simple Physical Model Unravels Influences of Chemokine on Shape Deformation and Migration of Human Hematopoietic Stem Cells. *Scientific Reports*, 8(1):1–9, 2018.

[87] Cornelia Monzel, Alexandra S Becker, Rainer Saffrich, Patrick Wuchter, Anthony D Ho, and Motomu Tanaka. Dynamic cellular phynotyping defines specific mobilization mechanisms of human hematopoietic stem and progenitor cells induced by SDF1 α versus synthetic agents. *Scientific Reports*, 8(1841):1–10, 2018.

[88] Metin Tolan. *X-Ray Scattering from Soft-Matter Thin Films*, volume 148 of *Springer Tracts in Modern Physics*. Springer Berlin Heidelberg, Berlin, Heidelberg, 1999.

[89] H. H. de Sénarmont, E. Verdet, and L. F. Fresnel. *Oeuvres Complètes D'Augustin Fresnel*. Imprimerie impériale, 1866.

[90] J. Daillant and A. Gibaud, editors. *X-ray and Neutron Reflectivity. Principles and Applications*. Springer, Berlin Heidelberg, lect. note edition, 2009.

[91] Ullrich Pietsch, Vaclav Holy, and Tilo Baumbach. *High-resolution X-ray scattering: from thin films to lateral nanostructures*. Springer Science & Business Media, 2004.

[92] L G Parratt. Surface studies of solids by total reflection of x-rays. *Physical Review*, 95(2):359–369, 1954.

[93] F. Abelès. La théorie générale des couches minces. *Journal de Physique et le Radium*, 11(7):307–309, 1950.

[94] F. Abelès. La détermination de l'indice et de l'épaisseur des couches minces transparentes. *J. phys. radium*, 11(7):310–314, 1950.

[95] Koji Ohta and Hatsuo Ishida. Matrix formalism for calculation of electric field intensity of light in stratified multilayered films. *Applied Optics*, 29(13):1952–1959, 1990.

[96] P. T. Boggs, J. R. Donaldson, R. H. Byrd, and R. B. Schnabel. Algorithm 676: Odrpack: software for weighted orthogonal distance regression. *ACM Transactions on Mathematical Software (TOMS)*, 15(4):348–364, 1989.

[97] Joachim Rädler and Erich Sackmann. Imaging optical thicknesses and separation distances of phospholipid vesicles at solid surfaces. *Journal de Physique II*, 3(5):727–748, 1993.

[98] Gerald Wiegand, Klaus R Neumaier, and Erich Sackmann. Microinterferometry: three-dimensional reconstruction of surface microtopography for thin-film and wetting studies by reflection interference contrast microscopy (ricm). *Applied optics*, 37(29):6892–6905, 1998.

[99] Laurent Limozin and Kheya Sengupta. Quantitative reflection interference contrast microscopy (ricm) in soft matter and cell adhesion. *ChemPhysChem*, 10(16):2752–2768, 2009.

[100] A. Vogel, S. Busch, and U. Parlitz. Shock wave emission and cavitation bubble generation by picosecond and nanosecond optical breakdown in water. *The Journal of the Acoustical Society of America*, 100(1):148–165, 1996.

[101] Vogel, A. and Lauterborn, W. and Timm R. Optical and acoustic investigations of the dynamics of laser produced cavitation bubbles near a solid boundary, 1989.

[102] Emil Alexandru Brujan, Kester Nahen, Peter Schmidt, and Alfred Vogel. Dynamics of laser-induced cavitation bubbles near an elastic boundary. *Journal of Fluid Mechanics*, 433:251–281, 2001.

[103] Melvin H Rice and John M Walsh. Equation of state of water to 250 kilobars. *The Journal of Chemical Physics*, 26(4):824–830, 1957.

[104] Lord Rayleigh. Viii. on the pressure developed in a liquid during the collapse of a spherical cavity. *The London, Edinburgh, and Dublin Philosophical Magazine and Journal of Science*, 34(200):94–98, 1917.

[105] Nykolai Bilaniuk and George SK Wong. Speed of sound in pure water as a function of temperature. *The Journal of the Acoustical Society of America*, 93(3):1609–1612, 1993.

[106] Milton S Plesset and Richard B Chapman. Collapse of an initially spherical vapour cavity in the neighbourhood of a solid boundary. *Journal of Fluid Mechanics*, 47(2):283–290, 1971.

[107] NS Gov and SA Safran. Red blood cell membrane fluctuations and shape controlled by atp-induced cytoskeletal defects. *Biophysical journal*, 88(3):1859–1874, 2005.

[108] Timo Betz, Martin Lenz, Jean-François Joanny, and Cécile Sykes. Atp-dependent mechanics of red blood cells. *Proceedings of the National Academy of Sciences*, 106(36):15320–15325, 2009.

[109] Miguel Lamas-Murua, Bettina Stolp, Sheetal Kaw, Judith Thoma, Nikolaos Tsopoulidis, Birthe Trautz, Ina Ambiel, Tatjana Reif, Sakshi Arora, Andrea Imle, Nadine Tibroni, Jingxia Wu, Guoliang Cui, Jens V. Stein, Motomu Tanaka, Ruth Lyck, and Oliver T. Fackler. HIV-1 Nef Disrupts CD4 + T Lymphocyte Polarity, Extravasation, and Homing to Lymph Nodes via Its Nef-Associated Kinase Complex Interface . *The Journal of Immunology*, 201(9):2731–2743, 2018.

[110] GA Dunn and AF Brown. A unified approach to analysing cell motility. *Journal of Cell Science*, 1987(Supplement_8):81–102, 1987.

[111] Guenter Albrecht-Buehler. The phagokinetic tracks of 3t3 cells. *Cell*, 11(2):395–404, 1977.

[112] Peter B Noble, Martin D Levine, et al. *Computer-assisted analyses of cell locomotion and chemotaxis*. CRC Press, 1986.

[113] A. W. Partin, J. S. Schoeniger, J. L. Mohler, and D. S. Coffey. Fourier analysis of cell motility: Correlation of motility with metastatic potential. *Proceedings of the National Academy of Sciences of the United States of America*, 86(4):1254–1258, 1989.

[114] Tolstov P Georgi. Fourier series, 1976.

[115] Michael Peter Norton and Denis G Karczub. *Fundamentals of noise and vibration analysis for engineers*. Cambridge university press, 2003.

[116] C. M. Svensson, A. Medyukhina, I. Belyaev, N. Al-Zaben, and M. T. Figge. Untangling cell tracks: Quantifying cell migration by time lapse image data analysis. *Cytometry Part A*, 93(3):357–370, 2018.

[117] MJ Saxton. Chapter 6 Single-Particle Tracking. In *Handbook of Modern Biophysics*, volume 1, pages 147–180. Humana Press, 2009.

[118] MJ Saxton. Single-particle tracking: the distribution of diffusion coefficients. *Biophysical journal*, 72(4):1744, 1997.

[119] PFF Almeida and WLC Vaz. Chapter 6 Lateral Diffusion in Membranes. In *Handbook of Biological Physics*, volume 1, pages 305–357. Elsevier Science, 1995.

[120] H. C. Berg. Random walks in biology. In *Random Walks in Biology*. Princeton University Press, 2018.

[121] S. Wong, W.-H. Guo, and Y.-L. Wang. Fibroblasts probe substrate rigidity with filopodia extensions before occupying an area. *Proceedings of the National Academy of Sciences*, 111(48):17176–17181, 2014.

[122] J. Ballester-Beltran, M. J. P. Biggs, M. J. Dalby, M. Salmeron-Sanchez, and A. Leal-Egana. Sensing the difference: the influence of anisotropic cues on cell behavior. *Frontiers in Materials*, 2:39, 2015.

[123] H. R. Bourne and O. Weiner. Cell polarity: a chemical compass. *Nature*, 419(6902):21–21, 2002.

[124] T. Ishii, J. Kikuta, A. Kubo, and M. Ishii. Control of osteoclast precursor migration: a novel point of control for osteoclastogenesis and bone homeostasis. *IBMS BoneKEy*, 7:279, 2010.

[125] H van Beijeren and R Kutner. Mean square displacement of a tracer particle in a hard-core lattice gas. *Physical review letters*, 55(2):238, 1985.

[126] MJ Saxton and K Jacobson. Single-particle tracking: applications to membrane dynamics. *Annual review of biophysics and biomolecular structure*, 26(1):373–399, 1997.

[127] MJ Saxton. Lateral diffusion in an archipelago. The effect of mobile obstacles. *Biophysical journal*, 52(6):989, 1987.

[128] MJ Saxton. Lateral diffusion in an archipelago. distance dependence of the diffusion coefficient. *Biophysical journal*, 56(3):615, 1989.

[129] A. Greiner, W. Strittmatter, and J. Honerkamp. Numerical integration of stochastic differential equations. *Journal of Statistical Physics*, 51(1-2):95–108, 1988.

[130] Peter E Kloeden and Eckhard Platen. Stochastic differential equations. In *Numerical solution of stochastic differential equations*, pages 103–160. Springer, 1992.

[131] F Kauffmann, O Lüderitz, H Stierlin, O West-phal, et al. The immunochemistry of enterobacteriaeeae. i, analysis of the sugar components of the salmonella-o-antigen. *Zentralblatt fur Bakteriologie, Parasitenkunde, Infektionskrankheiten und Hygiene*, 178(4):442–58, 1960.

[132] Klaus Brandenburg, Jörg Andrä, Mareike Müller, Michel H.J. Koch, and Patrick Garidel. Physicochemical properties of bacterial glycopolymers in relation to bioactivity. *Carbohydrate Research*, 338(23):2477–2489, 2003.

[133] Klaus Brandenburg and Ulrich Seydel. Physical aspects of structure and function of membranes made from lipopolysaccharides and free lipid A. *BBA - Biomembranes*, 775(2):225–238, 1984.

[134] Ulrich Seydel, Michel H.J. Koch, and Klaus Brandenburg. Structural polymorphisms of rough mutant lipopolysaccharides Rd to Ra from Salmonella minnesota, 1993.

[135] Sigma-Aldrich. *https://www.sigmaaldrich.com/*.

[136] Rute I.S. Romão and Amélia M. Gonçalves Da Silva. Phase behaviour and morphology of binary mixtures of DPPC with stearonitrile, stearic acid, and

octadecanol at the air-water interface. *Chemistry and Physics of Lipids*, 131(1):27–39, 2004.

[137] Yingying Chen, Runguang Sun, and Bo Wang. Monolayer behavior of binary systems of betulinic acid and cardiolipin: Thermodynamic analyses of Langmuir monolayers and AFM study of Langmuir-Blodgett monolayers. *Journal of Colloid and Interface Science*, 353(1):294–300, 2011.

[138] N Watanabe, A Watanabe, and Y Tamai. Hyomen oyobi kaimen (surface and interface). *Kyouritsu Shuppan, Tokyo*, pages 58–60, 1973.

[139] E.K. Rideal J.T. Davies. Interfacial phenomena. *Academic Press, New York*, 1963.

[140] Andrew Nelson. Co-refinement of multiple-contrast neutron/X-ray reflectivity data using MOTOFIT. *Journal of Applied Crystallography*, 39(2):273–276, mar 2006.

[141] W Abuillan. *Fine-Structures, Lateral Correlation and Diffusion of Membrane-Associated Proteins on Biological Membrane Surfaces*. PhD thesis, Ruperto-Carola University of Heidelberg, Germany, 2013.

[142] Avanti Polar Lipids Inc. *https://avantilipids.com/*.

[143] AbMole BioScience. *http://www.abmole.com/*.

[144] O. W. Blaschuk, R. Sullivan, S. David, and Y. Pouliot. Identification of a cadherin cell adhesion recognition sequence. *Developmental biology*, 139(1):227–229, 1990.

[145] E. Williams, G. Williams, B. J. Gour, O. W. Blaschuk, and P. Doherty. A novel family of cyclic peptide antagonists suggests that n-cadherin specificity is determined by amino acids that flank the hav motif. *Journal of Biological Chemistry*, 275(6):4007–4012, 2000.

[146] W. Kern and D. A. Puotinen. Cleaning solutions based on hydrogen peroxide for use in silicon semiconductor technology. *RCA Rev.*, 31(2):187–206, 1970.

[147] David Needham and Rashmi S. Nunn. Elastic deformation and failure of lipid bilayer membranes. *Biophysical Journal*, 58(October):997–1009, 1990.

[148] T. H. Bayburt and S. G. Sligar. Self-assembly of single integral membrane proteins into soluble nanoscale phospholipid bilayers. *Protein science*, 12(11):2476–2481, 2003.

[149] JS Ploem. Reflection-contrast microscopy as a tool for investigation of the attachment of living cells to a glass surface. *Mononuclear phagocytes in immunity, infection and pathology*, pages 405–421, 1975.

[150] Michael Bass. *Handbook of Optics: Volume I-Geometrical and Physical Optics, Polarized Light, Components and Instruments*. McGraw-Hill Education, 2010.

[151] Lord Rayleigh. Xxxi. investigations in optics, with special reference to the spectroscope. *The London, Edinburgh, and Dublin Philosophical Magazine and Journal of Science*, 8(49):261–274, 1879.

[152] Benjamin Fröhlich. *Haemoglobinopathies and the Protection Against Severe Malaria: Probing Cytoadhesion and Mechanics of Plasmodium falciparum Infected Erythrocytes*. PhD thesis, Ruperto-Carola University of Heidelberg, Germany, 2019.

[153] Johannes Schindelin, Ignacio Arganda-Carreras, Erwin Frise, Verena Kaynig, Mark Longair, Tobias Pietzsch, Stephan Preibisch, Curtis Rueden, Stephan Saalfeld, Benjamin Schmid, Jean Yves Tinevez, Daniel James White, Volker Hartenstein, Kevin Eliceiri, Pavel Tomancak, and Albert Cardona. Fiji: An open-source platform for biological-image analysis, jul 2012.

[154] Chakravart, Laha, and Roy. *Handbook of Methods of Applied Statistics*. John Wiley and Sons, volume i edition, 1967.

[155] Internet Archive Wayback Machine. *https://web.arChive.org/web/20160818104718/http://www.mathematik.uni-kl.de/~schwaar/Exercises/Tabellen/table_kolmogorov.pdf*.

[156] Yusuke T. Maeda, Junya Inose, Miki Y. Matsuo, Suguru Iwaya, and Masaki Sano. Ordered patterns of cell shape and orientational correlation during spontaneous cell migration. *PLoS ONE*, 3(11), 2008.

[157] Yan Levin, Alexandre P Dos Santos, and Alexandre Diehl. Ions at the air-water interface: an end to a hundred-year-old mystery? *Physical review letters*, 103(25):257802, 2009.

[158] Alexandre P dos Santos, Alexandre Diehl, and Yan Levin. Surface tensions, surface potentials, and the hofmeister series of electrolyte solutions. *Langmuir*, 26(13):10778–10783, 2010.

[159] Alexandre P dos Santos, Amin Bakhshandeh, and Yan Levin. Effects of the dielectric discontinuity on the counterion distribution in a colloidal suspension. *The Journal of chemical physics*, 135(4):044124, 2011.

[160] R. M. E. Richards and R. J. McBride. Enhancement of benzalkonium chloride and chlorhexidine acetate activity against Pseudomonas aeruginosa by aromatic alcohols. *Journal of pharmaceutical sciences*, 62(12):2035–2037, 1973.

[161] J. A. Barry and K. Gawrisch. Direct nmr evidence for ethanol binding to the lipid-water interface of phospholipid bilayers. *Biochemistry*, 33(26):8082–8088, 1994.

[162] O. Purrucker, H. Hillebrandt, K. Adlkofer, and M. Tanaka. Deposition of highly resistive lipid bilayer on silicon–silicon dioxide electrode and incorporation of gramicidin studied by ac impedance spectroscopy. *Electrochimica Acta*, 47(5):791–798, 2001.

[163] Orest W. Blaschuk. Discovery and development of N-cadherin antagonists. *Cell and Tissue Research*, 348(2):309–313, May 2012.

[164] Ellen L. Weisberg, Martin Sattler, Abdel Kareem Azab, Dirk Eulberg, Anna Kruschinski, Paul W. Manley, Richard Stone, and James D. Griffin. Inhibition of SDF-1-induced migration of oncogene-driven myeloid leukemia by the L-RNA aptamer (Spiegelmer), NOX-A12, and potentiation of tyrosine kinase inhibition. *Oncotarget*, 8(66):109973–109984, 2017.

[165] Aldo M. Roccaro, Antonio Sacco, Werner G. Purschke, Michele Moschetta, Klaus Buchner, Christian Maasch, Dirk Zboralski, Stefan Zöllner, Stefan Vonhoff, Yuji Mishima, Patricia Maiso, Michaela R. Reagan, Silvia Lonardi,

Marco Ungari, Fabio Facchetti, Dirk Eulberg, Anna Kruschinski, Axel Vater, Giuseppe Rossi, Sven Klussmann, and Irene M. Ghobrial. SDF-1 inhibition targets the bone marrow niche for cancer therapy. *Cell Reports*, 9(1):118–128, 2014.

[166] A. Vater, J. Sahlmann, N. Kröger, S. Zöllner, M. Lioznov, C. Maasch, K. Buchner, D. Vossmeyer, F. Schwoebel, W. G. Purschke, S. Vonhoff, A. Kruschinski, K. Hübel, M. Humphrey, S. Klussmann, and F. Fliegert. Hematopoietic stem and progenitor cell mobilization in mice and humans by a first-in-class mirror-image oligonucleotide inhibitor of CXCL12. *Clinical Pharmacology and Therapeutics*, 94(1):150–157, 2013.

[167] Julia Hoellenriegel, Dirk Zboralski, Christian Maasch, Nathalie Y. Rosin, William G. Wierda, Michael J. Keating, Anna Kruschinski, and Jan A. Burger. The Spiegelmer NOX-A12, a novel CXCL12 inhibitor, interferes with chronic lymphocytic leukemia cell motility and causes chemosensitization. *Blood*, 123(7):1032–1039, 2014.

[168] H. Ludwig, K. Weisel, M. T. Petrucci, X. Leleu, A. M. Cafro, L. Garderet, C. Leitgeb, R. Foa, R. Greil, I. Yakoub-Agha, D. Zboralski, S. Vauléon, T. Dümmler, D. Beyer, A. Kruschinski, K. Riecke, M. Baumann, and M. Engelhardt. Olaptesed pegol, an anti-CXCL12/SDF-1 Spiegelmer, alone and with bortezomib-dexamethasone in relapsed/refractory multiple myeloma: A Phase IIa Study. *Leukemia*, 31(4):997–1000, 2017.

[169] S. G. Sayyed, H. Hägele, O. P. Kulkarni, K. Endlich, S. Segerer, D. Eulberg, S. Klussmann, and H. J. Anders. Podocytes produce homeostatic chemokine stromal cell-derived factor-1/CXCL12, which contributes to glomerulosclerosis, podocyte loss and albuminuria in a mouse model of type 2 diabetes. *Diabetologia*, 52(11):2445–2454, 2009.

[170] Byung Sik Cho, Hee Je Kim, and Marina Konopleva. Targeting the CXCL12/CXCR4 axis in acute myeloid leukemia: From bench to bedside. *Korean Journal of Internal Medicine*, 32(2):248–257, 2017.

[171] Rita De Cássia Carvalho Melo, Ana Leda Longhini, Carolina Louzão Bigarella, Mariana Ozello Baratti, Fabiola Traina, Patrícia Favaro, Paula

De Melo Campos, and Sara Teresinha Olalla Saad. CXCR7 is highly expressed in acute lymphoblastic leukemia and potentiates CXCR4 response to CXCL12. *PLoS ONE*, 9(1):1–12, 2014.

[172] Michael Steurer, Marco Montillo, Lydia Scarfò, Francesca R. Mauro, Johannes Andel, Sophie Wildner, Livio Trentin, Ann Janssens, Sonja Burgstaller, Anna Frömming, Thomas Dümmler, Kai Riecke, Matthias Baumann, Diana Beyer, Stéphanie Vauléon, Paolo Ghia, Robin Foà, Federico Caligaris-Cappio, and Marco Gobbi. Olaptesed pegol (NOX-A12) with bendamustine and rituximab: A phase IIa study in patients with relapsed/refractory chronic lymphocytic leukemia. *Haematologica*, 104(10):2053–2060, 2019.